

MECHANICAL CHARACTERIZATION OF ADDITIVELY MANUFACTURED
Ti-6Al-4V AIRCRAFT STRUCTURAL COMPONENTS PRODUCED BY
ELECTRON BEAM MELTING

A THESIS SUBMITTED TO
THE GRADUATE SCHOOL OF NATURAL AND APPLIED SCIENCES
OF
MIDDLE EAST TECHNICAL UNIVERSITY

BY

FATİH YILMAZ

IN PARTIAL FULFILLMENT OF THE REQUIREMENTS
FOR
THE DEGREE OF DOCTOR OF PHILOSOPHY
IN
AEROSPACE ENGINEERING

AUGUST 2022

Approval of the thesis:

**MECHANICAL CHARACTERIZATION OF ADDITIVELY
MANUFACTURED Ti-6Al-4V AIRCRAFT STRUCTURAL COMPONENTS
PRODUCED BY ELECTRON BEAM MELTING**

submitted by **FATİH YILMAZ** in partial fulfillment of the requirements for the degree of **Doctor of Philosophy in Aerospace Engineering, Middle East Technical University** by,

Prof. Dr. Halil Kalıpçılar
Dean, Graduate School of **Natural and Applied Sciences**

Prof. Dr. Serkan Özgen
Head of the Department, **Aerospace Engineering**

Assoc. Prof. Dr. Melin Şahin
Supervisor, **Aerospace Engineering, METU**

Assoc. Prof. Dr. Ercan Gürses
Co-Supervisor, **Aerospace Engineering, METU**

Examining Committee Members:

Prof. Dr. Demirkan Çöker
Aerospace Engineering, METU

Assoc. Prof. Dr. Melin Şahin
Aerospace Engineering, METU

Assoc. Prof. Dr. Mehmet Bülent Özer
Mechanical Engineering, METU

Prof. Dr. Erdem Acar
Mechanical Engineering, TOBB ETÜ

Assist. Prof. Dr. Recep Muhammet Görgülüarslan
Mechanical Engineering, TOBB ETÜ

Date: 25.08.2022

I hereby declare that all information in this document has been obtained and presented in accordance with academic rules and ethical conduct. I also declare that, as required by these rules and conduct, I have fully cited and referenced all material and results that are not original to this work.

Name Last name : Fatih Yılmaz

Signature :

ABSTRACT

MECHANICAL CHARACTERIZATION OF ADDITIVELY MANUFACTURED Ti-6Al-4V AIRCRAFT STRUCTURAL COMPONENTS PRODUCED BY ELECTRON BEAM MELTING

Yılmaz, Fatih

Doctor of Philosophy, Aerospace Engineering

Supervisor : Assoc. Prof. Dr. Melin Şahin

Co-Supervisor: Assoc. Prof. Dr. Ercan Gürses

August 2022, 178 pages

Weight reduction of structural parts is one of the most important efforts of design and analysis studies to improve fuel efficiency and flight performance of aerospace vehicles through topology optimization creating complex geometric designs that are lighter but cannot be produced via conventional manufacturing methods. Instead, the manufacturing of the resulting designs is possible with additive manufacturing methods where the final product is obtained by adding layer upon layer to obtain close to the near-net-shape. However, the material properties produced by additive manufacturing are not standardized and fully known. Therefore, this thesis aims to obtain the tensile, fatigue, and pin-bearing material properties of Ti-6Al-4V alloy produced by electron beam melting (EBM) with test campaigns carried out according to ASTM standards. Test specimens are manufactured in three build directions, and the effect of build direction on material properties is investigated. Additionally, the effect of hot isostatic pressing (HIP) as a post-treatment revealed that the unwanted pores in the material are almost thoroughly closed. Having obtained the material properties, the pylon fitting of an unmanned aerial vehicle is lightened by topology optimization.

Finally, as novel scientific contributions, this study includes comprehensive test campaigns and investigates the effects of three orthogonal build directions on elastoplastic properties, while many studies focus on only two-build directions. Evaluation of Poisson's ratio is the other originality of this study. Furthermore, another finding through micro CT imaging is that temporary support structures result in intense defects closer to applied surfaces; hence high-stress regions of structures should be avoided to use support structures.

Keywords: Additive Manufacturing, Electron Beam Melting, Titanium, Topology Optimization, Unmanned Aerial Vehicle Structural Component

ÖZ

ELEKTRON DEMETİ İLE ERGİTME EKLEMELİ İMALAT YÖNTEMİYLE ÜRETİLEN Ti-6Al-4V UÇAK YAPISAL PARÇALARININ MEKANİK KARAKTERİZASYONU

Yılmaz, Fatih
Doktora, Havacılık ve Uzay Mühendisliği
Tez Yöneticisi: Doç. Dr. Melin Şahin
Yardımcı Tez Yöneticisi: Doç. Dr. Ercan Gürses

Ağustos 2022, 178 sayfa

Hava ve uzay araçlarının yakıt verimi ve uçuş performansını iyileştirmek için yapısal parçaların topoloji optimizasyonu ile hafifletilmesi, tasarım ve analiz çalışmalarının en önemli amaçlarından biridir. Bu noktada; karmaşık geometriye sahip daha hafif tasarımlar ortaya çıkmakta ancak konvansiyonel imalat yöntemleriyle üretilmemektedir. Ortaya çıkan tasarım ise katman üzerine katman ekleyerek gerçekleştiren eklemeli imalat yöntemleriyle net şekle yakın olarak üretilmektedir. Ancak, eklemeli imalat ile üretilen malzemelerin özellikleri standardize edilmemiştir ve tam olarak da bilinmemektedir. Bu nedenle bu tez çalışmasında, bir toz yatağında metalik eklemeli imalat yöntemi olan elektron demeti ile ergitme (EBM) ile üretilen Ti-6Al-4V alaşımının çekme, yorulma ve pim-ezme malzeme özelliklerinin ASTM standartlarına göre gerçekleştirilen test kampanyaları ile elde edilmesi amaçlanmıştır. Test numuneleri üç üretim yönünde üretilmiştir ve üretim yönlerinin malzeme özelliklerine etkisi araştırılmıştır. Bunun yanında, bir ardıl işlem olan sıcak izostatik preslemenin (HIP) malzemedeki istenmeyen gözenekleri neredeyse tamamen giderdiği de gözlemlenmiştir. Test kampanyaları ile

malzeme özellikleri elde edildikten sonra, bir insansız hava aracının pilon bağlantı parçasının ağırlığı topoloji optimizasyonu ile azaltılmıştır.

Son olarak bilimsel katkıları özetlemek gerekirse; bu çalışma kapsamlı bir test kampanyasını içermektedir ve birçok çalışma sadece iki üretim yönüne odaklanırken bu çalışmada esas olarak birbirine dik üç üretim yönünün elastoplastik özellikler üzerindeki etkisi araştırılmıştır. Bu çalışmanın bir diğer özgünlüğü de Poisson oranının değerlendirilmesidir. Bunlara ek olarak elde edilen bir diğer bulgu ise, mikro CT görüntüleme ile destek yapılarının uygulandığı yüzeylerde daha yoğun kusurlara yol açtığına gözlemlenmesidir; bu nedenle yapısal parçaların yüksek gerilimli bölgelerinde destek yapıları kullanmaktan kaçınılmalıdır.

Anahtar Kelimeler: Eklemeli İmalat, Elektron Demeti ile Ergitme, Titanyum, Topoloji Optimizasyonu, İnsansız Hava Aracı Yapısal Parçası

I would like to dedicate my thesis to my daughter Defne, my son Atlas,
and my wife, Canan

ACKNOWLEDGMENTS

First of all, I would like to thank my thesis advisor Assoc. Prof. Dr. Melin Şahin for his outstanding academic and project management contribution to my studies, his inspiring motivation throughout my thesis, and guidance from beginning to end of the overall work. At the same time, I would also like to thank my co-supervisor, Assoc. Prof. Dr. Ercan Gürses, for his outstanding academic contributions, guidance, encouragement, and criticism of my thesis work.

I gratefully acknowledge the support and funding of the Presidency of Defence Industries (SSB), Turkish Aerospace Industries, and Middle East Technical University, Aerospace Department with project code and number DDEKL1 and 2019-03-13-32-00-03, respectively.

I also would like to thank Assoc. Prof. Dr. M. Bülent Özer, and Prof. Dr. Demirkan Çöker for their wise advice and critics provided during thesis progress committee meetings.

I would like to thank METU RUZGEM academic staff for their excellent testing experience reflected in my thesis and for their patience.

I would like to thank Aslan Makina, PMC companies, and Mustafa Boybey, who contributed to processing test specimens and producing the static test setup with an excellent industry experience and dedication.

I would also like to thank to my industry thesis advisor Dr. İlhan Şen for his significant contribution to manufacturing and observing the parts inside the Turkish Aerospace facilities and for his pragmatic and analytic contribution to my project works, to Mine Alemdaroğlu Temel and Cahit Mavili, who have supported the thesis studies and project management with great dedication and finally to my friends Okan Yıldırım, Burak Sarı, Dr. Fahri Buğra Çamlıca, Mustafa Özgür Aydoğan, who both supported and motivated me throughout my thesis work.

TABLE OF CONTENTS

| | |
|--|-------|
| ABSTRACT..... | v |
| ÖZ | vii |
| ACKNOWLEDGMENTS | x |
| TABLE OF CONTENTS..... | xi |
| LIST OF TABLES | xiv |
| LIST OF FIGURES | xv |
| LIST OF ABBREVIATIONS | xxii |
| LIST OF SYMBOLS | xxiii |
| CHAPTERS | |
| 1 INTRODUCTION | 1 |
| 1.1 Context | 1 |
| 1.2 Motivation | 2 |
| 1.3 Objectives..... | 3 |
| 1.4 Limitations | 5 |
| 1.5 Outline..... | 5 |
| 2 LITERATURE SURVEY | 7 |
| 2.1 Introduction | 7 |
| 2.2 History of additive manufacturing | 7 |
| 2.3 The additive manufacturing process | 8 |
| 2.3.1 Processes and materials..... | 10 |
| 2.3.2 Powder bed fusion method and electron beam melting | 11 |
| 2.4 Effects of defects in additive manufacturing..... | 13 |
| 2.5 Applications of additive manufacturing | 21 |

| | | |
|-------|---|-----|
| 2.6 | Conclusion | 26 |
| 3 | EXPERIMENTAL INVESTIGATION ON MECHANICAL PERFORMANCE OF ELECTRON BEAM MELTED Ti-6Al-4V | 27 |
| 3.1 | Additive manufacturing of test specimens with electron beam melting and hot isostatic pressing..... | 27 |
| 3.2 | Tensile test campaign..... | 32 |
| 3.2.1 | Methods and means of tensile test campaign | 34 |
| 3.2.2 | Statistical analyses and results of tensile test campaign..... | 42 |
| 3.3 | Fatigue test campaign | 57 |
| 3.3.1 | Fatigue test methods and means | 58 |
| 3.3.2 | Results of fatigue test campaign and modeling of fatigue life by Airbus IQF method using test data | 63 |
| 3.4 | Pin-bearing testing campaign..... | 75 |
| 3.4.1 | Pin-bearing test means and methods | 77 |
| 3.4.1 | Results of pin-bearing test campaign | 81 |
| 4 | A CASE STUDY TO LIGHTEN AN UNMANNED AERIAL VEHICLE PYLON FITTING BY TOPOLOGY OPTIMIZATION AND ELECTRON BEAM MELTING | 87 |
| 4.1 | Introduction..... | 87 |
| 4.2 | Topology optimization of the unmanned aerial vehicle pylon fitting | 88 |
| 4.2.1 | Finite element modeling of the fitting | 90 |
| 4.2.2 | Topology optimization of the fitting | 94 |
| 4.2.3 | Optimized solid geometry creation | 101 |
| 4.2.4 | Result of the topology optimization and finite element re-analysis | 102 |
| 4.3 | Validation of the optimized fitting..... | 106 |

| | | |
|-------|--|-----|
| 4.3.1 | Comparison of static finite element analysis results of original and optimized fitting | 106 |
| 4.3.2 | Comparison of modal and transient load analysis results | 107 |
| 4.3.3 | Double shear lug static analysis | 113 |
| 4.3.4 | Estimation of fatigue life of the optimized fitting | 116 |
| 4.3.5 | Additive manufacturing and testing of the optimized fitting | 119 |
| 5 | CONCLUSION | 131 |
| 5.1 | General conclusions | 131 |
| 5.2 | Recommendation for future work | 136 |
| | REFERENCES | 139 |
| | APPENDICES | 149 |
| A. | Fractured tensile test specimens and test results | 149 |
| B. | Fractured fatigue test specimens and test results | 151 |
| C. | Derivation of IQF method and related factors | 153 |
| D. | Fractured pin-bearing test specimens and test results | 161 |
| E. | Finite element model element size dependency check..... | 165 |
| F. | Optimization convergence check and element size dependency | 167 |
| G. | Static failure loads of metallic double shear lug | 171 |
| | CURRICULUM VITAE | 177 |

LIST OF TABLES

| | |
|--|-----|
| Table 2.1 Static tensile and fracture toughness values for SLM and EBM Ti-6Al-4V [7]. | 21 |
| Table 3.1 Manufactured ASTM E8 tensile test specimen quantities. | 35 |
| Table 3.2 Parameters of F-test and t-test | 43 |
| Table 3.3 F-test and t-test results of two groups. | 53 |
| Table 3.4 Comparison of elastoplastic properties with build direction independent studies and conventional AMS4911 Ti-6Al-4V alloy | 54 |
| Table 3.5 Comparison of elastoplastic properties with regard to build directions. | 55 |
| Table 3.6 Material constants and standard deviations | 66 |
| Table 3.7 Comparison of p-index values | 67 |
| Table 3.8 Averaged summary pin bearing results according to build direction and edge distance and comparison of AMS4911. | 82 |
| Table 4.1 CBUSH element stiffness values | 94 |
| Table 4.2 Optimization constraints. | 100 |
| Table 4.3 Comparison of FEA maximum values. | 105 |
| Table 4.4 Static FEA result comparison | 107 |
| Table 4.5 Material properties for dynamic analysis. | 108 |
| Table 4.6 Free mode frequencies excluding rigid body modes | 108 |
| Table 4.7 System natural frequencies | 111 |
| Table 4.8 Calculation summary for double lug shear analysis | 116 |
| Table A.1 Tensile test results | 150 |
| Table B.1 R=0.1 Constant amplitude fatigue test results. | 152 |
| Table C.1 Effect of the type of structural configuration | 157 |
| Table D.1 Pin-bearing test results | 164 |
| Table E.1 Element quantities and lug tip displacement values. | 165 |
| Table G.1 Parameters for lug static analysis | 171 |

LIST OF FIGURES

| | |
|--|----|
| Figure 2.1. Percentage shares of additive manufacturing in industries [14]. | 8 |
| Figure 2.2. Effect of layer thickness on the final part [16]. | 9 |
| Figure 2.3. The generic process of CAD to part shows all eight stages. | 10 |
| Figure 2.4. Schematic diagrams of four main methods of additive manufacturing: (a) fused deposition modeling; (b) inkjet printing; (c) stereolithography; (d) powder bed fusion [17]. | 11 |
| Figure 2.5. Electron Beam Melting (EBM) machine's main components [20] | 12 |
| Figure 2.6. Global energy density versus porosity [10]. | 14 |
| Figure 2.7. (a) lack of fusion pores due to low energy, (b) minimized porosity obtained for optimized energy density, (c) high energy vaporization pores with different sphericity [10]. | 14 |
| Figure 2.8. Pyramid structure [23] | 15 |
| Figure 2.9. Effect of pore size [8]. | 17 |
| Figure 2.10. Experimental and calculated fatigue life comparison [26] | 18 |
| Figure 2.11. Tensile and fatigue test results [30]. | 20 |
| Figure 2.12. Additively manufactured hydraulic reservoir rack consolidates 126 parts into one, courtesy of Airbus [14] | 22 |
| Figure 2.13. Aircraft part before and after topology optimization [33]. | 23 |
| Figure 2.14. Airbus A320 nacelle fitting before and after topology optimization [34]. | 24 |
| Figure 2.15. The integrated design approach for the infill patterning of an airfoil based on internal stress [13]. | 24 |
| Figure 2.16. A bracket installed on a spacecraft developed by Oerlikon and Ruag Space (a) Conventional machining (b) Additive manufacturing after topology optimization [12]. | 25 |
| Figure 2.17. Aerospace fitting before and after topology optimization [35] | 25 |
| Figure 3.1. Build directions of a test specimen. | 28 |

| | |
|---|----|
| Figure 3.2. Arcam Q20 Plus machine and manufactured test specimens. (a) Interior view of the machine (b) Manufactured tensile test specimens and build platform. | 29 |
| Figure 3.3. HIP facility..... | 30 |
| Figure 3.4. HIP chamber and laid test specimens at the last stage, respectively..... | 31 |
| Figure 3.5. Applied HIP process. | 31 |
| Figure 3.6. Tensile test specimen dimensions and build directions. (a) Specimen dimensions according to ASTM E8 and build directions (b) Specimen manufacturing layout in same build tank. | 36 |
| Figure 3.7. (a) Schematic for the cause of surface roughness (b) Pre- and post-machined specimens with build directions..... | 37 |
| Figure 3.8. MicroCT imaging component schematic..... | 38 |
| Figure 3.9. Sample painted tensile test specimens | 39 |
| Figure 3.10. (a) Tensile test and DIC capture configuration (b) A view from the test campaign..... | 40 |
| Figure 3.11. DIC extensometers to calculate strains by image processing. (a) 50 mm extensometer according to ASTM E8 (b) Longitudinal and transverse extensometers to calculate Poisson's Ratio | 41 |
| Figure 3.12. Local strain distribution before rupture. | 41 |
| Figure 3.13. Extraction of 0.2% yield strength and ultimate strength sample | 45 |
| Figure 3.14. Averaging Poisson's ratio at elastic region..... | 46 |
| Figure 3.15. Representative lateral cross-sections of as-built and HIP post-treated specimens from microCT images..... | 47 |
| Figure 3.16. Internal defects and pores close to the support structure surface: Schematic cross-section locations and microCT images..... | 48 |
| Figure 3.17. Effect of Hot Isostatic Pressing (HIP) on elastoplastic properties of Ti-6Al-4V alloy manufactured by EBM. | 49 |
| Figure 3.18. Build direction comparison, (a) As-built specimens (b) HIP specimens. | 50 |
| Figure 3.19. Averaged plastic properties and standard deviations; (a) Yield strength (b) Ultimate strength (c) Elongation (d) Reduction of area (RA) | 51 |

| | |
|--|----|
| Figure 3.20. Averaged elastic properties and standard deviations, (a) Modulus of elasticity, (b) Poisson's ratio | 52 |
| Figure 3.21. Airframe structural failure distribution [52]. | 58 |
| Figure 3.22. S-N Curve (Wöhler Curve) creation by coupon testing [53] | 59 |
| Figure 3.23. Goodman-Haigh diagram [54]..... | 60 |
| Figure 3.24. Specimens with tangentially blending fillets between the uniform test section and the ends. | 60 |
| Figure 3.25. (a) Fatigue test specimen samples representing three build directions and support structures before removal, (b) sample machined specimens..... | 61 |
| Figure 3.26. Constant amplitude fatigue test machine and test specimen. | 62 |
| Figure 3.27. R=0.1 fatigue test overall scatter on S-N (Wöhler) curve | 64 |
| Figure 3.28. Description of IQF | 65 |
| Figure 3.29. Change standard deviation of parameter M with respect to p value. . | 67 |
| Figure 3.30. Comparison of material constant M for different build directions and Airbus Ti-6Al-4V material constant. | 68 |
| Figure 3.31. L-NH build direction fatigue life calculation using the first four data and the IQF method. | 69 |
| Figure 3.32. T-NH build direction fatigue life calculation using the first four data and the IQF method. | 69 |
| Figure 3.33. ST-NH build direction fatigue life calculation using the first four data and the IQF method. | 70 |
| Figure 3.34. L-H build direction fatigue life calculation using the first four data and the IQF method. | 70 |
| Figure 3.35. T-H build direction fatigue life calculation using the first four data and the IQF method. | 71 |
| Figure 3.36. ST-H build direction fatigue life calculation using the first four data and the IQF method. | 71 |
| Figure 3.37. As-built specimens - Goodman-Haigh diagram. | 72 |
| Figure 3.38. HIP post-treated specimens - Goodman-Haigh diagram. | 73 |
| Figure 3.39. As-built-specimens pre and post-test comparison. | 74 |

| | |
|---|----|
| Figure 3.40. Typical failure modes of joints [56]. | 76 |
| Figure 3.41. Dimensions for pin-bearing properties. | 76 |
| Figure 3.42. Pin bearing specimen. | 77 |
| Figure 3.43. Pin bearing test schematic with tensile test machine. | 78 |
| Figure 3.44. Pin bearing test configuration. | 78 |
| Figure 3.45. Pin bearing test displacement calibration by DIC. | 79 |
| Figure 3.46. Calibration data | 79 |
| Figure 3.47. Extraction of yield and ultimate bearing strengths from a sample test data. | 80 |
| Figure 3.48. First pin-bearing specimen and deformed bolt after failure. | 81 |
| Figure 3.49. $e/D=1.5$ Ultimate and yield pin-bearing strength comparison. | 83 |
| Figure 3.50. $e/D=2.0$ Ultimate and yield pin-bearing strength comparison. | 83 |
| Figure 4.1. Schematic view of UAV and pylons which hold the payloads (not scaled). | 88 |
| Figure 4.2. Front and isometric view of pylon fitting to be optimized. | 89 |
| Figure 4.3. Generic process flow of weight reduction campaign. | 89 |
| Figure 4.4. Process flowchart for FEM creation. | 90 |
| Figure 4.5. Generic presentation of the simulation. | 91 |
| Figure 4.6. FEM of the fitting. | 91 |
| Figure 4.7. Clevis pin modeling as steel beam element. | 92 |
| Figure 4.8 Fastener modeling as CBUSH. | 92 |
| Figure 4.9. CBUSH element spring constants representation for a fastener. | 93 |
| Figure 4.10. Structural optimization categories. a) sizing optimization of a truss structure b) shape optimization c) topology optimization [59]. | 95 |
| Figure 4.11. The topology optimization computation flow [59]. | 96 |
| Figure 4.12. An example of an additive-manufactured part with build direction indicated with the black arrow, showing self-supporting build angles in green, and areas overhanging greater than 45° requiring support structure in red [61]. | 97 |
| Figure 4.13. Definition of the build direction vector and OHA definition [61]. | 98 |

| | |
|---|-----|
| Figure 4.14. Example of the results obtained by varying the allowable OHA parameter [61]. | 98 |
| Figure 4.15. Process flowchart for topology optimization. | 99 |
| Figure 4.16. Optimization model including build direction. | 99 |
| Figure 4.17. Additive manufacturing properties defined at the topology variable. | 100 |
| Figure 4.18. Process flowchart for optimized geometry creation. | 102 |
| Figure 4.19. Displacement magnitude values distribution. | 103 |
| Figure 4.20. Von Mises, Max, and Min principal stresses, respectively. | 103 |
| Figure 4.21. Smoothed and exported STL mesh data. | 104 |
| Figure 4.22. Optimized final solid geometry, front and isometric view. | 104 |
| Figure 4.23. Displacement magnitude values distribution of optimized fitting.... | 105 |
| Figure 4.24. Comparison of the first three modes of pre- and post-optimization for an unconstrained case. | 109 |
| Figure 4.25. FEM for calculation of system modes and transient load response. | 110 |
| Figure 4.26. Retention and recoil force in parallel to the ground direction. | 110 |
| Figure 4.27. Acceleration data acquisition point for each model. | 111 |
| Figure 4.28. Explanation of shock response spectrum [64]. | 112 |
| Figure 4.29. Calculated shock response spectrum for $Q=10$. | 113 |
| Figure 4.30. Bearing yield strength data obtained from pin-bearing tests. | 114 |
| Figure 4.31. Geometric dimensions for calculation. | 115 |
| Figure 4.32. Representation of equivalent force direction. | 116 |
| Figure 4.33. (a) load-time history, (b) rain-flow cycle counting [68]. | 117 |
| Figure 4.34. Conversion to monotonic loading. | 118 |
| Figure 4.35. Build direction optimization. | 120 |
| Figure 4.36. Sample build direction on the 2D drawing. | 121 |
| Figure 4.37. Sample support structure definition on drawing as “Zones” by hatching. | 122 |
| Figure 4.38. Functional zone examples shown by hatching. | 122 |
| Figure 4.39. Material offset example. | 122 |

| | |
|--|-----|
| Figure 4.40. Optimized fitting manufactured by EBM after two attempts. | 123 |
| Figure 4.41. Original fitting and final optimized fitting comparison. | 124 |
| Figure 4.42. Static test setup schematic for qualification of the optimized fitting. | 125 |
| Figure 4.43. Test case FEA and loadings. | 126 |
| Figure 4.44. Resultant max von Mises stresses for 600 kgf and 700 kgf. | 126 |
| Figure 4.45. Strain gauge bonding location selection. | 127 |
| Figure 4.46. Test setup installation. | 127 |
| Figure 4.47. Image processing and data acquisition. | 128 |
| Figure 4.48. Comparison of static FEA results and the test data. | 129 |
| Figure A.1. As-built tensile test specimens after fracture. | 149 |
| Figure A.2. HIP post-treated tensile test specimens after fracture. | 149 |
| Figure B.1. HIP post-treated fatigue test specimens after fatigue fracture. | 151 |
| Figure B.2. As-built fatigue test specimens after fatigue fracture. | 151 |
| Figure C.1. Cyclic tension [71] | 153 |
| Figure C.2. Hysteresis loops with different mean stress [71]. | 154 |
| Figure C.3. Neuber's rule [71] | 155 |
| Figure C.4. Effect of C value on IQF. | 157 |
| Figure C.5. Radius for scale factor calculation. | 158 |
| Figure C.6. Variation of scale factor according to notch radius. | 158 |
| Figure C.7. Stress concentration factors Kt for opposite deep hyperbolic notches in an infinitely wide thin element in tension [75]. | 159 |
| Figure D.1. As built ST build direction pin-bearing test specimens after fracture. | 161 |
| Figure D.2. As built T build direction pin-bearing test specimens after fracture.. | 161 |
| Figure D.3. As built L build direction pin-bearing test specimens after fracture.. | 162 |
| Figure D.4. HIP post-treated ST build direction pin-bearing test specimens after fracture. | 162 |
| Figure D.5 HIP post-treated T build direction pin-bearing test specimens after fracture. | 163 |

| | |
|--|-----|
| Figure D.6. HIP post-treated L build direction pin-bearing test specimens after fracture. | 163 |
| Figure E.1. Lug tip point for the displacement comparison..... | 165 |
| Figure F.1. Element densities contour, element quantities, and vfrac convergence results. | 167 |
| Figure F.2. Geometries regarding converged vfrac values after each optimization. | 168 |
| Figure F.3. Change of volumetric fraction objective according to iterations. | 169 |
| Figure F.4. Change of lug tip displacement according to load cases and iterations. | 169 |
| Figure F.5. Change of max principal stress according to iterations..... | 170 |
| Figure G.1. Lug definition and dimension parameters. | 173 |

LIST OF ABBREVIATIONS

| | |
|-------|--|
| 3DP | Three-Dimensional Printing |
| AM | Additive Manufacturing |
| ASTM | American Society for Testing and Materials |
| CAD | Computer-Aided Design |
| CAM | Computer-Aided Manufacturing |
| CCD | Charge-Coupled Device |
| CoG | Center of Gravity |
| CT | Computerized Tomography |
| DED | Direct Energy Deposition |
| DIC | Digital Image Correlation |
| EBM | Electron Beam Melting |
| FDM | Fused Deposition Modeling |
| FE | Finite Element |
| FEM | Finite Element Model |
| GPa | Gigapascals |
| H | HIPed |
| HIP | Hot Isostatic Pressing |
| IQF | Fatigue Quality Index |
| L | Longitudinal |
| LOM | Laminated Object Manufacturing |
| METU | Middle East Technical University |
| MMPDS | Metallic Material Properties Development and Standardization |
| MPa | Megapascals |
| NA | Not Applicable |
| NASA | National Aeronautics and Space Administration |
| NH | Non-HIPed |
| RA | Reduction of Area |
| RAMP | Rational Approximation of Material Properties |
| RF | Reserve Factor |
| SDOF | Single Degree of Freedom |
| SIMP | Solid Isotropic Material with Penalization |
| SLM | Selective Laser Melting |
| SLS | Selective Laser Sintering |
| SRS | Shock Response Spectrum |
| ST | Short Transverse |
| STL | Standard Triangle Language |
| T | Transverse |
| UAV | Unmanned Aerial Vehicle |
| UTS | Ultimate Strength |
| YS | Yield Strength |

LIST OF SYMBOLS

| | |
|--------------------------|---|
| D | Damage |
| E | Modulus of elasticity |
| e/D | Edge distance/hole diameter |
| IQF | Fatigue quality index |
| K | Stiffness matrix |
| K_q | Fracture toughness |
| K_{IC} | Plane-strain fracture toughness |
| K_t | Stress concentration factor |
| $k_{fast,shear}^{FEM}$ | Shear spring coefficient |
| $k_{fast,axial}^{FEM}$ | Axial spring coefficient |
| $k_{fast,bending}^{FEM}$ | Bending spring coefficient |
| M | Material constant |
| m | Penalization factor |
| N | Number of cycles |
| n_A | Sample quantity of Group A |
| n_B | Sample quantity of Group B |
| R | Fatigue test stress ratio (S_{max}/S_{min}) |
| $R_{p0.2}$ | 0.2% Yield strength |
| R_m, R_{pu} | Ultimate strength |
| R_{bry} | Bearing yield strength |
| R_{bru} | Bearing ultimate strength |
| S_{max} | Fatigue test maximum stress |
| S_{min} | Fatigue test minimum stress |
| S_{eq} | Equivalent stress |
| S_{FLC} | Flight life cycle stress |
| s_A | Standard deviation of Group A |
| s_B | Standard deviation of Group B |
| \bar{X}_A | Mean of Group A |
| \bar{X}_B | Mean of Group B |
| Greek Letters | |
| α | Significance level |
| ρ | Relative density |
| σ | Stress |
| ν | Poisson's ratio |

CHAPTER 1

INTRODUCTION

The ability to design and manufacture lightweight parts is a primary effort for fuel economy and improved flight performance of an aircraft or a satellite. Weight reduction of an aerospace structural part by free-form design is an achievable task; however, this can result in complex geometries that may not be manufactured rapidly and efficiently with traditional fabrication methods. At this point, additive manufacturing methods, also called 3D printing, can enable complex geometries to be manufactured easily and fast. However, until now, the main scope of additive manufacturing is rapid prototyping. Although additive manufacturing is a rapid prototyping method, it also attracts companies to utilize it in serial manufacturing. In addition to the rapid manufacturing advantage, additive manufacturing brings other advantages such as producing assemblies consisting of multiple parts into one piece, minimizing delivery times, eliminating the need for tooling for production, and not storing spare parts. Furthermore, aerospace companies conduct research activities and invest significant capital in this perspective to incorporate additive manufacturing into their design and production processes.

1.1 Context

According to ISO/ASTM 52900:2015 definition, additive manufacturing (AM) makes parts by joining materials layer upon layer instead of machining, which subtracts layers [1]. Transferring directly from the CAD environment to production offers a unique opportunity for prototyping. In addition to prototyping, the industrial use of this production method has been gaining momentum recently. It also includes opportunities for the automotive and medical implant industry, especially aerospace.

Additive manufacturing consists of various technologies to process versatile materials, and for many years its dominant application has been the manufacturing of prototypes or rapid prototyping. However, the recent growth in applications for direct near-net-shape part manufacturing or rapid manufacturing has resulted in more research efforts focusing on developing new processes and materials [2]. Additive manufacturing does not need tooling or computer-aided manufacturing (CAM) tools. Computer-aided design (CAD) data can be manufactured directly from the additive manufacturing machine.

1.2 Motivation

In the aerospace industry, there is a continuous drive to decrease the weight of a compound while aiming for high performance. Throughout the years, many new materials and manufacturing technologies have been investigated, developed, and integrated to the aerospace industry. Significantly composite technologies have radically changed the industry as composites are highly customizable and could be optimized to the specific needs to improve performance while reducing the structural weight. Initially, it was labor-intensive, then new technologies were adopted to automate the manufacturing process to reduce cost.

Metals have been the proven material for the industry with various manufacturing technologies, such as sheet forming, milling, extrusion, and casting. Manufacturing constraints have bound the structural design with conventional technologies, allowing limited weight reduction and performance improvement. However, the emergence of additive manufacturing literally removes the manufacturing constraints and allows designers more freedom to optimize the structural parts further.

Additive manufacturing makes up a part by additively printing layer by layer to extend the part that arises from the powder. This technology is promising, but with all other new materials or manufacturing methods, the materials and process should

be investigated, and the actual mechanical behavior has to be determined to ensure the capabilities and limitations of this technology. In particular, aviation airworthiness authorities push aerospace structural part manufacturers to prove their processes and materials. In order to adapt additive manufacturing for the aerospace industry to produce airframe flying structural parts, it is necessary to investigate the mechanical performance of the final material and reveal its properties with a scientific approach. In this study, the material properties resulting from the electron beam melting (EBM) method, which is likely to be widely used in the production of airframe parts, will be investigated. The resulting material properties will be used in weight reduction campaigns with topology optimization of aerospace structures. Since topology optimization obtains complex geometries, the part will be realized with the additive manufacturing method, whose final product mechanical properties are known.

1.3 Objectives

The opportunity that metal additive manufacturing can be used in the production of aerospace structural parts, especially in the fabrication of lightweight but complex geometries obtained by topology optimization, led to the conduct of this research. Although there are several metallic additive manufacturing methods, this study investigates the mechanical performance of Ti-6Al-4V alloy obtained from Arcam Q20 Plus electron beam melting (EBM) machine, which utilizes powder bed fusion technology. EBM machine manufacturer states that Arcam Q20 Plus is developed especially for airframe part manufacturing [3].

Plenty of studies characterize and understand the mechanical behavior of materials produced by EBM additive manufacturing. In the literature, many studies have been presented to describe the tensile [4], [5], [6], [7], and fatigue [5], [8] behavior. However, there is no study on the investigation of pin-bearing properties. Additionally, studies have also been performed on the porosity/inner structure [9], [10], surface quality [11], [7], and post-treatment such as HIP [4], [5].

In most studies, insight was gained into the individual properties, but a cohesive bond between material properties and design was not considered. The focus is predominantly on characterizing and understanding the EBM method because many aspects of this new technology resulting material are unknown.

On the other hand, many topology optimization studies were performed for additive manufacturing [12], [13]. In the studies, the design optimization is performed with assumed material properties, and the obtained design was purely theoretical rather than the actual manufactured part that met all requirements.

The lack of linking the design method with material properties is due to more understanding of the material being needed before proceeding to the design for the application. In this study, a case study is carried out in which the pylon fitting of an unmanned aerial vehicle is lightened. Thus, it aims to determine the material's tensile properties in the elastic and plastic region to validate the part obtained from this case study with analysis methods. Furthermore, it aims to create a fatigue model by obtaining high cycle fatigue data to calculate the fitting fatigue life. In addition to the tensile and fatigue properties, a pin-bearing test campaign is also conducted to obtain pin-bearing strength. All these mechanical properties are aimed to be investigated for as-built and HIP (hot isostatic pressing) post-treated test specimens. The HIP process is a post-treatment method applied at high temperatures and pressure to remove unsolicited pores and defects in metal structures produced with powder technology.

In addition to obtaining the mechanical performance of the final product, it is essential to determine the design criteria for metallic additive manufacturing by powder bed fusion. This study collects the experience gained during research and test sample production as design criteria. Furthermore, a topology optimization process combined with the design criteria is aimed to be developed for weight reduction of an unmanned aerial vehicle pylon fitting.

1.4 Limitations

The research is limited to Electron Beam Melting powder bed technology for specimens and parts manufactured with Arcam Q20 Plus machine with Ti-6Al-4V grade 5 powder. The surfaces of the test samples are milled since the surface roughness is high due to the EBM method, and therefore the effect of surface roughness is excluded from the scope.

The research scope is limited to mechanical performance derived from the design criteria that drive the design of an aerospace fitting, namely maximum tensile loading, pin bearing loading, and fatigue criteria. Hence, the developed design methodology is limited to fitting designs printed with additive manufacturing technology. Still, it applies to other manufacturing technology or designs of other components with an alteration. Furthermore, mechanical properties are obtained under room conditions; elevated or cryogenic temperatures are out of the scope of the research.

1.5 Outline

The thesis describes the investigation of the development of an aerospace part with additive manufacturing in six chapters.

Chapter 1 explains this thesis's motivation, objective, limitations and it also provides the outline.

Chapter 2 gives an overview of the prominent properties of materials printed by electron beam melting powder bed technology. The material properties are investigated, and the current design methodology for additively manufactured parts is determined. Furthermore, the design criteria required for aerospace fittings are discussed.

Chapter 3 presents the tensile, fatigue, and pin-bearing testing campaign required to develop an additively manufactured part. The investigation is performed for as-built and Hot Isostatic Pressing (HIP) post-treated specimens.

Chapter 4 demonstrates a design case in which an unmanned aerial vehicle fitting is optimized and designed with additive manufacturing constraints. A detailed analysis is performed, and verification by static, dynamic, and fatigue analyses is shown. Optimized and additively manufactured fitting is tested by a custom-made test rig. The design rules for additive manufacturing are determined, and a complete additive manufacturing procedure, including topology optimization, is also included in this chapter.

Chapter 5 restates the objective of this thesis and discusses and presents outcomes of the research study. In this chapter, the essential conclusions from the entire work are briefly noted in a concise summary and the recommendations for further study are also given.

CHAPTER 2

LITERATURE SURVEY

2.1 Introduction

A literature survey is conducted to relate this research on additive manufacturing with other studies and benefit from other studies. First of all, a survey is focused on the definition of the additive manufacturing method, its types, and the materials used. After obtaining information about additive manufacturing, academic research on electron beam melting, a powder bed fusion method, is carried out. The literature review results in the most critical drawback encountered in additive manufacturing: porosity. It has also been investigated how the porous structures can affect the material properties used in aerospace structure strength calculations. Finally, the application of additive manufacturing on aerospace structural parts is also researched.

2.2 History of additive manufacturing

History from the Wohlers' Report states that "Additive manufacturing first emerged in 1987 with stereolithography from 3D Systems, a process that solidifies thin layers of ultraviolet light-sensitive liquid polymer using a laser." [14]. Afterward, the commercialization of additive manufacturing started. The contribution of advanced electronics and computer technology makes additive manufacturing more popular. Additive manufacturing is not an alternative to subtractive manufacturing, but rapid prototyping or progress to custom-based manufacturing is inevitable. From 1987 to now, additive manufacturing technologies are available broadly for commercial or scientific purposes. The subject of this thesis is a powder bed fusion method, and the first commercialized additive manufacturing method is the selective laser sintering

(SLS) method, which is a powder bed fusion method developed by the University of Texas [15].

The Wohler's Report [14] presents the survey result of 52 additive manufacturer companies and 98 service providers for the share of additive manufacturing industries up to the year 2016. The research results are shown in Figure 2.1, where these companies serve. This figure shows that additive manufacturing comprises many industries where aerospace has a considerable share.

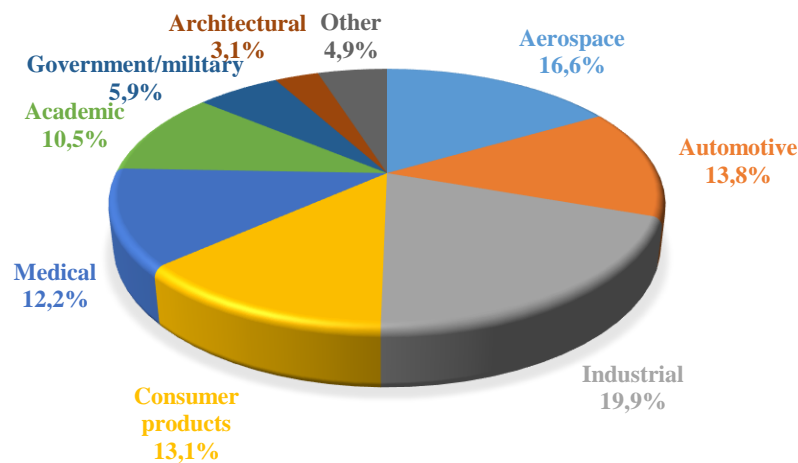


Figure 2.1. Percentage shares of additive manufacturing in industries [14].

2.3 The additive manufacturing process

The key to additive manufacturing is that parts are made by adding material in layers; each layer is a thin cross-section of the part derived from the original CAD data. Obviously, each layer must have a finite thickness in the physical world. So the resulting part will be an approximation of the original data, as shown in Figure 2.2. The thinner each layer is, the closer the final part will be to the original [15].



Figure 2.2. Effect of layer thickness on the final part [16].

Additive manufacturing involves several steps that move from the virtual CAD description to the resultant physical part. Different products will involve additive manufacturing in different ways and to different degrees. Small, relatively simple products may only use additive manufacturing for visualization models. In contrast, more oversized, more complex products with greater engineering content may involve additive manufacturing during numerous stages and iterations throughout the development process. Furthermore, the early stages of the product development process may only require rough parts, and then additive manufacturing can be used for fabrication due to the fast manufacturing. At later stages of the process, parts may require careful cleaning and post-processing (including sanding, surface preparation, and painting) before they are used, with additive manufacturing being practical here because of the complexity of form that can be created without having to consider tooling. Additive manufacturing generic process flow is shown in Figure 2.3.

Most production methods produce parts in a layer fashion. The final product is obtained by removing a layer from stock is achieved by production with machining. In additive manufacturing, the fabrication is done by adding layers upon layer. This manufacturing method was preliminary used for prototyping since it is a rapid manufacturing method; however, it started to be used for mass production.

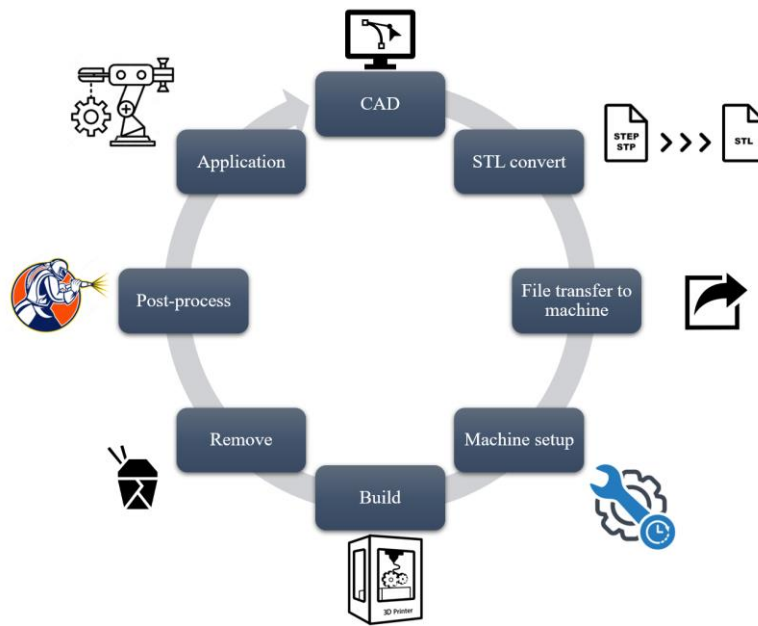


Figure 2.3. The generic process of CAD to part shows all eight stages.

2.3.1 Processes and materials

Fabrication with additive manufacturing has a variety of different production methods and materials. The most common additive manufacturing method mainly uses polymer filaments is fused deposition modeling (FDM). Furthermore, additive manufacturing of powders by selective laser sintering (SLS), selective laser melting (SLM), or liquid binding in three-dimensional printing (3DP), as well as inkjet printing, contour crafting, stereolithography, direct energy deposition (DED), and laminated object manufacturing (LOM) are the main methods of additive manufacturing [17]. Four generic additive manufacturing methods are presented in Figure 2.4.

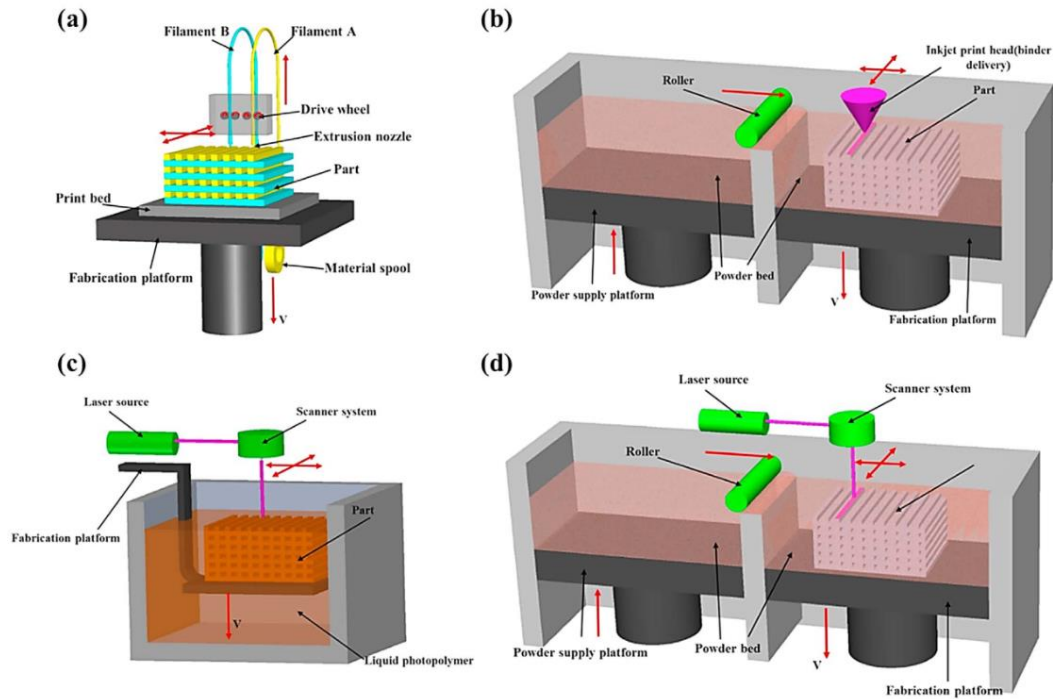


Figure 2.4. Schematic diagrams of four main methods of additive manufacturing: (a) fused deposition modeling; (b) inkjet printing; (c) stereolithography; (d) powder bed fusion [17].

For any manufacturing process, including additive manufacturing technologies, the feedstock must be formed into a state compatible with the process in question (e.g., powder, sheet, wire, liquid) [18]. According to the material list of Bourell et al. [18], metallic, polymer, and ceramic materials can be used in powder bed fusion methods. The metallic material used in EBM, a powder bed fusion method, is Ti-6Al-4V alloy. This metallic material is a titanium alloy used in aerospace structures commonly.

2.3.2 Powder bed fusion method and electron beam melting

Electron Beam Melting (EBM) is a powder bed fusion method, and all powder bed fusion methods have basic common features. These basic features are one or more heat sources to provide fusion between powder grains, and a method to keep the fusion of powder layers in a certain region are these basic features [15]. The EBM additive manufacturing is a method that is achieved by melting and fusion of alloy

powder with an electron beam close to light speed. If gas atoms are in the melting environment, electrons will collide with gas atoms and change their direction; therefore, the environment must be vacuumed to avoid collision [15]. Manufacturing with the EBM method was developed at Chalmers University-Sweden, and it was commercialized in 2001 by establishing ARCAM AB company [19]. Figure 2.5 shows the main components of an Arcam EBM machine. Melting of powder is performed at high pre-heating conditions by the electron beam. The electron beam also controls the temperature of the pre-heated environment at around 700°C. The electron beam is generated at Electron Beam Column with Cathode and then passes through the coils, which act as electromagnetic lenses controlling the beam [20]. Since electromagnetic control is used, layer melting speed is independent of inertia constraints of lenses, and better speed control is achieved compared to the laser beam melting method, which uses galvanometric mirrors for selective laser melting. The inertia of mirrors in the selective laser melting (SLM) method constrains the control.

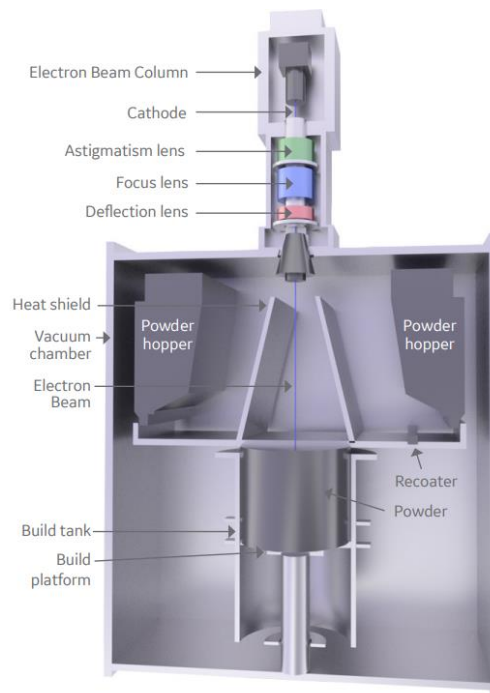


Figure 2.5. Electron Beam Melting (EBM) machine's main components [20]

In addition to the melting source, powder feed and layer formation infrastructure is another feature of the electron beam melting method. Powder hoppers are used to store and deliver metal powder layers. Recoater behaves like a rake and evenly distributes the powder layer before melting. The build platform is lowered towards the build tank after each selected layer melting. Finally, upon melting all selected layers, unmelted but sintered powders and support structures must be removed from the manufactured part by special mechanical post-processes.

Murr et al. [19] compare materials manufactured by EBM and SLM. The study also gives results for Ti-6Al-4V alloys manufactured by additive manufacturing. Martensitic structures are observed at the SLM method; however, they are not observed at the EBM method. Hardness tests also show that SLM manufactured materials are harder than EBM manufactured materials. On the other hand, grain structures are not dependent on scanning directions at both SLM and EBM is another finding from this study.

2.4 Effects of defects in additive manufacturing

Although additive manufacturing has indisputable advantages, it also brings some drawbacks besides. While literature search, it is realized that one of the most critical drawbacks is the formation of unsolicited porous structures in additive manufacturing by powder bed fusion. This section will summarize the effects of unwanted pores and other defects for powder bed fusion methods.

Kabir et al. [10] modeled an SLM manufactured Ti-6Al-4V alloy pores by Voronoi tessellations. The study also gives a clue about the energy level of melting versus porosity types. Figure 2.6 summarizes the outcome of this study that shows pore creation according to the melting energy density. In this figure, E_{opt} denotes optimum global energy density.

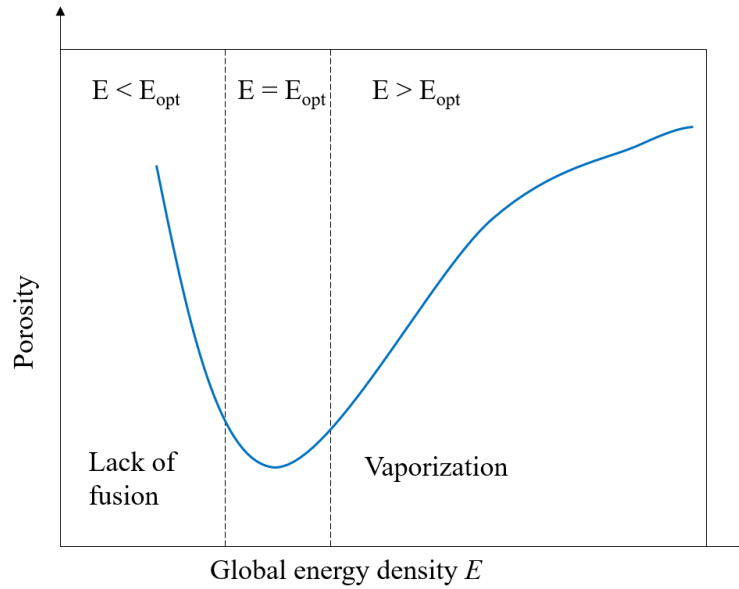


Figure 2.6. Global energy density versus porosity [10].

Different energy levels lead to different pore shapes as depicted in Figure 2.7, which may be sourced from balling effect, incomplete melting, unprocessed powder, tiny pores, and vaporization. While $E = E_{opt}$, an almost non-porous structure can be obtained. However, in the case of $E < E_{opt}$, the increase in porosity results from incomplete melting. Such pores are sharp, elongated crack-like structures as in Figure 2.7a. In the opposite case, $E > E_{opt}$, vaporization occurs, and the bubbles formed as a result of vaporization cause spherical pores, as shown in Figure 2.7c.

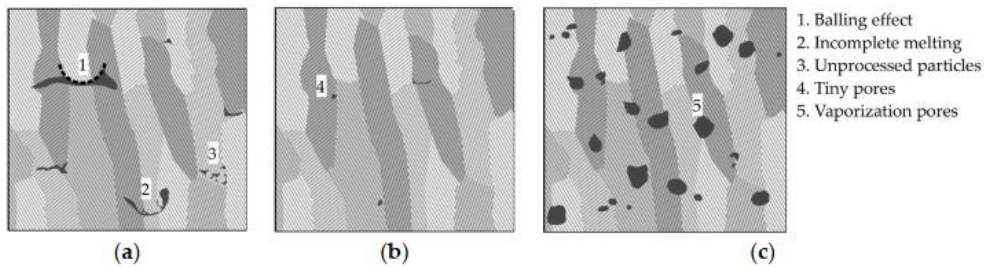


Figure 2.7. (a) lack of fusion pores due to low energy, (b) minimized porosity obtained for optimized energy density, (c) high energy vaporization pores with different sphericity [10].

Karlsson et al. [21] performed a study to see a strain gradient between layers by Digital Image Correlation (DIC). As a result, they could not observe strain gradients between layers due to lack of resolution; however, they could randomly observe some local strain gradients. These strain gradients are interpreted as the cause of pores resulting from incomplete melting. Global strain properties are almost the same between test specimens. It is suspected that pores resulting from additive manufacturing machine parameters are not optimized for 25-45 μm diameter powder.

Kok et al. [22] researched the effect of specimen thickness on microstructure and mechanical performance of EBM manufactured materials. Different thickness test specimens and 100 mm diameter and 43 mm height propellers are manufactured under this study. Some anomalies are observed during the manufacturing process by EBM. The major problems are metallization, warpage, and smoke. Moreover, the most important result from the study is that material tensile and ultimate strengths of complicated geometries can be obtained from the relations between hardness tests. The research also states that current studies are insufficient to determine mechanical properties, and statistical studies are needed.

Everhart et al. [23] studied the effect of beam length on the material properties. As parameters of the EBM device cannot be changed, they used a pyramid structure to see beam power proportional to beam length depicted in Figure 2.8. A 1.3 mm offset is used for the external contour of the beam scanning.

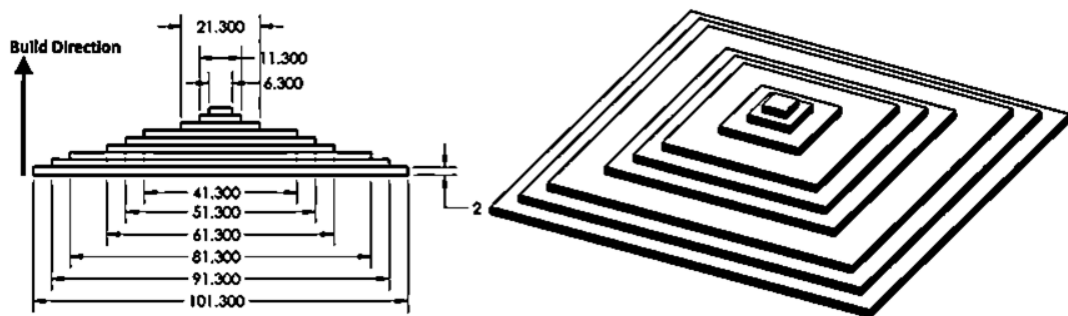


Figure 2.8. Pyramid structure [23]

Monolithic pyramid structure showed that beam length over 90 mm results in a porous structure. The pyramid structure also showed that density values depend on the beam length. After manufacturing the pyramid structure, 20 mm, 30 mm, 40 mm, 50 mm, and 70 mm square cross-section matrices are manufactured. As a result, mechanical performance is independent of density. When scanning length increases, density decreases, and strength also increases. It is assessed that this result is that when scan length increases, grains tend to be more refined. Material properties are not affected by build direction, but beam length is the most important outcome of this study.

Mohammadhosseini et al. [4] studied tension, hardness, and fatigue characteristics of Ti-6Al-4V material manufactured by EBM and applied HIP (Hot Isostatic Pressing) post-treatment to remove unsolicited defects. Moreover, grain structures are analyzed by scanning electron microscope. At the end of the study, they observed that HIP is increasing grain dimension. An increase in grain dimensions results in a ductile material. Hardness and yield strength decrease; however, the fatigue cycle and surface quality increase. On the other hand, pores resulting from improper melting are observed. However, results showed that materials comply with medical requirements. Grain structures are observed as more refined compared to the additive manufacturing machine provider data.

Tang et al. [24] studied the density, mechanical properties, and fatigue characteristics of Ti-6Al-4V alloys manufactured by EBM and HIP post-treated at different temperatures. The Archimedes method measures density and pores are analyzed by a computerized tomography scanner. Density values are improved slightly by HIP post-treatment. Pores resulting from incomplete melting can be observed on post-treated materials more and can be minimized by the HIP. After 870°C HIP post-treatment, martensitic grains are still observed; after 920°C HIP post-treatment, martensitic grains are not observed; but material properties became under requirements. From this point, it is stated that 900°C is the optimum temperature for HIP post-treatment.

Shunyu et al. [25] compared three types of Ti-6Al-4V additive manufacturing which are direct energy deposition (DED), selective laser melting (SLM), and electron beam melting (EBM). In this review, the two most common powder bed fusion additive manufacturing methods, SLM and EBM, are the focus of this study. The research paper gives information about manufacturing methods, microstructures, and defects. Microstructure properties, such as grain content, mainly affect the tensile properties of the additively manufactured material. However, surface roughness and internal porosity primarily result in fatigue properties degradation and crack initiation and propagation.

Tammas-Williams et al. [8] studied the effect of porosity on the fatigue life of additively manufactured Ti-6Al-4V samples. The study includes a prediction of stress concentration factors by four different ranking methods. Cylindrical test specimens with 4.5 mm diameter and 12 mm length are used in this study. Stress concentration factors are calculated according to aspect ratio and pore proximity to surface by the finite element method (FEM).

Figure 2.9 shows that cycle count decreases with a larger pore with less stress level, contrary to higher stress level with smaller pores. The circle size represents the pore dimension. However, despite insufficient data, subsurface pores may be more detrimental than internal pores, independent of pore size. Time-lapse X-ray computerized tomography is used during the fatigue test by interim imaging during the test campaign. It is observed that crack initiation occurs at 75–88%, 87–97%, 90–98%, and >93% of final failure cycles.

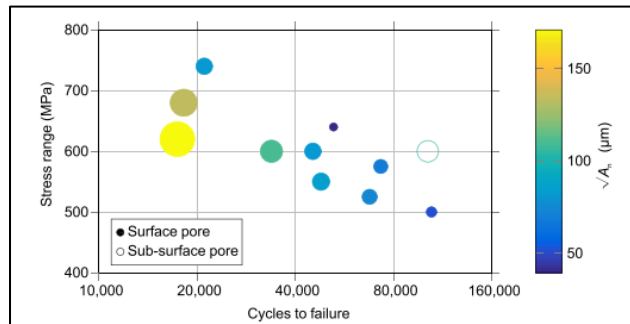
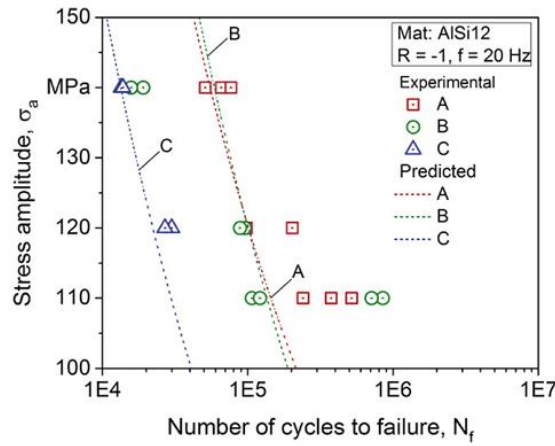


Figure 2.9. Effect of pore size [8].

Siddique et al. [26] investigate the effect of defects on the fatigue life of additively manufactured AlSi12 alloy by selective laser melting (SLM) method. Fatigue life tests are performed with ASTM E466 specimens. Porosity data of specimens are obtained by computerized micro-tomography. An experimental and calculated fatigue life comparison is presented in Figure 2.10. Batch A and Batch B surfaces are machined, but the Batch A base plate is not heated. Batch C is the same as batch B, but the surface is not machined. These conditions affect the pore distribution inside the specimens. Moreover, pore distribution and sizes affect the fatigue life of the specimens. Batch A has the highest fatigue life among the three batches. Surface quality decreases the fatigue strength when Batch C is observed.



specimens have the same or better fatigue behavior than the traditionally manufactured specimens is another outcome of the review.

Romano et al. [29] focus on Sentinel 1 satellite's reflector fitting optimized and manufactured by selective laser melting additive manufacturing. A statistical approach is asserted to overcome NASA's new standard that enforces witness samples during additive manufacturing of parts. These witness samples may not contain the same porosity size and distribution inside the target complex shape products. Then, computerized tomography may analyze witnesses, and a statistical method, "extrema value analyses," can be applied to the product. Obtained statistical data is used to estimate fatigue life with experimental results using the Kitagawa diagram and Murakami's equivalent defect size. Microstructural analysis and fatigue tests showed that failure is mainly sourced from the defects close to or on the surface in parallel with other studies.

Edwards and Ramulu [30] claim the benefits of additive manufacturing for aerospace structures in the manner of carbon footprint decrease. The main scope of the research is to determine the effect of surface quality of additively manufactured Ti-6Al-4V alloys by selective laser melting. A set of test specimens is also manufactured to see the effect of build direction. Residual stress and surface roughness are measured after manufacturing. Half of the specimen surfaces are machined. Some tensile test specimens are also manufactured and tested by ASTM E8 standard. This was not the main scope, but it helps to understand the fatigue behavior of fatigue life. Research cannot find any correlation between surface quality and fatigue life. However, building in longitudinal direction results in poor fatigue life. Tensile and fatigue life tests are shown in Figure 2.11. One of the most important outcomes of the study is that additively manufactured specimens have approximately 77% lower fatigue life than wrought alloy. More experiments without pores and residual stress should be performed to understand the surface quality effect on fatigue life is the final recommendation of the study.

| | Average | STDEV |
|-------------------------|---------|-------|
| Yield strength (MPa) | 910 | 9.9 |
| Ultimate strength (MPa) | 1035 | 29.0 |
| Elongation (%) | 3.3 | 0.76 |

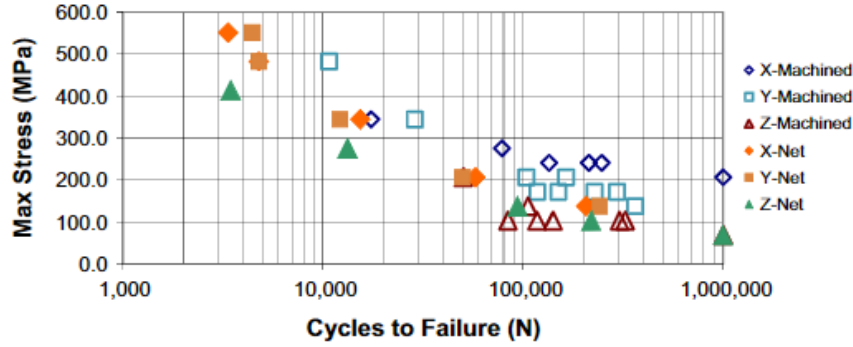


Figure 2.11. Tensile and fatigue test results [30].

Greitemeier et al. [7] have performed experimental research to understand and compare mechanical properties such as tensile, fracture toughness, fatigue crack growth rate, and high cycle fatigue behavior. Different test specimens are manufactured with a selective laser melting method (SLM) and electron beam melting. Surface roughness is kept as built for test specimens and machined specimens for another group. On the other hand, two different heat treatments, such as annealing and hot isostatic pressing (HIP) applied to see the difference. Table 2.1 summarizes tensile test results and fracture toughness results. The selective laser melting (SLM) method has higher tensile strength than EBM manufactured test specimens. This results from martensitic grains in SLM manufactured specimens due to rapid cooling. Surface roughness has a slight effect on tensile stress. It may be due to thickness measurement where surface porosity blocks thickness measurement accurately. However, surface roughness decreases elongation independent of heat treatment. Fracture toughness is varied by factor compared to heat treatments, while the EBM method has no difference among heat-treated specimens. Crack growth properties are also tested, and it is observed that all cases obey Paris region rules.

Table 2.1 Static tensile and fracture toughness values for SLM and EBM Ti-6Al-4V [7].

| Process | Heat treatment | Surface quality | YS, R _{p0.2} [MPa] | UTS, R _m [MPa] | A [%] | K _q /K _{IC} [MPa√m] |
|---------|----------------|-----------------|--------------------------------|------------------------------|--------|--|
| SLM | Annealed | Milled | 1086±1.5 | 1165±5.4 | 15±0.5 | 49.5±1.5 ^a |
| | | As-built | 1017±6.7 | 1096±7.4 | 12±0.5 | |
| | HIP | Milled | 894±3.4 | 997±4.0 | 18±0.5 | 93.5±0.5 ^b |
| | | As-built | 837±0.7 | 949±2.7 | 13±1.4 | |
| EBM | Annealed | Milled | 868±18.6 | 972±111.7 | 15±0.0 | 106.5±3.5 ^b |
| | | As-built | 869±6.5 | 965±4.5 | 6±0.0 | |
| | HIP | Milled | 774±15.6 | 896±11.6 | 18±0.5 | 119 ^b |
| | | As-Built | 718±12.7 | 833±8.7 | 14±0.5 | |

Invalidity criteria= $2.5(K_q/R_{p0.2})^2 < (W-a)$

^a valid

^b invalid

2.5 Applications of additive manufacturing

The evolution of rapid prototyping to additive manufacturing also attracted the aerospace industry's attention. Aerospace manufacturers' investment in state of the art manufacturing technology is progressing drastically. Many studies are being performed to use it as a serial manufacturing process more than prototyping. Wohlers report [14] states that Airbus has done considerable work designing and producing polymer and metal additively manufactured parts for its aircraft. It has manufactured and is flying thousands of plastic brackets, clips, and other devices for holding cables, wires, and hoses in place. Many are produced by ULTEM 9085 material on Fused Deposition Modeling (FDM) equipment. Figure 2.12 shows a hydraulic reservoir rack built by additive manufacturing for Airbus, consolidated from 126 pieces into one.

Additive manufacturing methods have also been developed to meet the demand for printing complex structures at fine resolutions. Rapid manufacturing capability, the

ability to print complex structures, reducing printing defects, and enhancing mechanical properties are key factors driving the development of additive manufacturing technologies.



Figure 2.12. Additively manufactured hydraulic reservoir rack consolidates 126 parts into one, courtesy of Airbus [14]

Products can be designed as complex shapes, customized geometry, and integrated assembly. However, mechanical designers need to know manufacturing limitations, and the trade-off, performance vs. serial production cost, should be considered. In aerospace structures, additive manufacturing is intended to be used mainly to produce complex geometries obtained after topology optimization because these two methods ensure the optimum weight of the structural part without losing its strength. Topology optimization is a branch of structural optimization. This method iteratively distributes materials available in a design domain to give an optimized structure for an objective function. A typical topology optimization algorithm combines two distinct modules, one for analysis and optimization [31]. Although there are several design approaches, such as shape optimization and size optimization, only the topology optimization of an aerospace structure is the aim of this study in the manner of design for additive manufacturing. Additive manufacturing will allow the build of optimized, lightweight, complex geometry that cannot be manufactured by machining.

Goh et al. [32] state according to the Breguet method, aerodynamic parameters must be maximized, and weight must be minimized for longer endurance of fixed-wing unmanned aerial vehicles (UAVs). However, complex inner structures cannot be manufactured by conventional methods. Additive manufacturing brings a new challenge for unmanned air vehicles in the manner of shape and inner structure. The introduction of additive manufacturing has revolutionized the field of UAVs but has influenced the entire manufacturing arena by simplifying the design and easing the fabrication process [32]. UAVs and aerospace components routinely exploit additive techniques like fused deposition modeling (FDM), selective laser sintering (SLS), stereolithography (SLA), selective laser melting (SLM), and electron beam melting (EBM). FDM, SLA, polyjet, and SLS have been used to fully print the UAV structures or fabricate certain parts of UAV structures. For instance, Seabra [33] used the SLM method and topology optimization to lighten an aircraft part by 28%, shown in Figure 2.13.

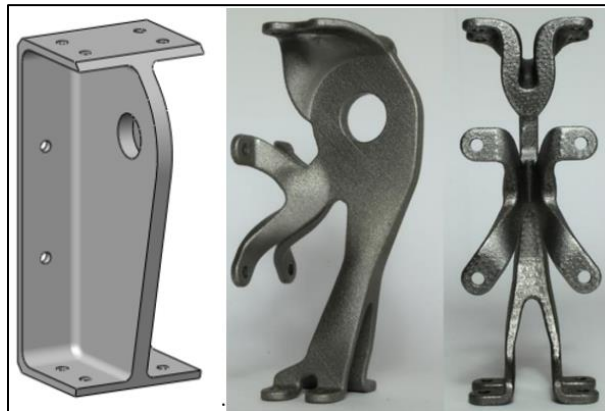


Figure 2.13. Aircraft part before and after topology optimization [33].

Tomlin and Meyer [34] reduced the weight of the hinge fitting of the nacelle of Airbus A320 aircraft by 64% with topology optimization. Photograph of original and optimized parts is shown in Figure 2.14.



Figure 2.14. Airbus A320 nacelle fitting before and after topology optimization [34].

Kim et al. [13] focused on the porous infill of a wing structure more than the overall shape and infill structure. Stages are introduced in Figure 2.15. The designed infill is manufactured by Fused Deposition Modeling and tested. Results showed that stiffness is better than the conventional designed constant infill.

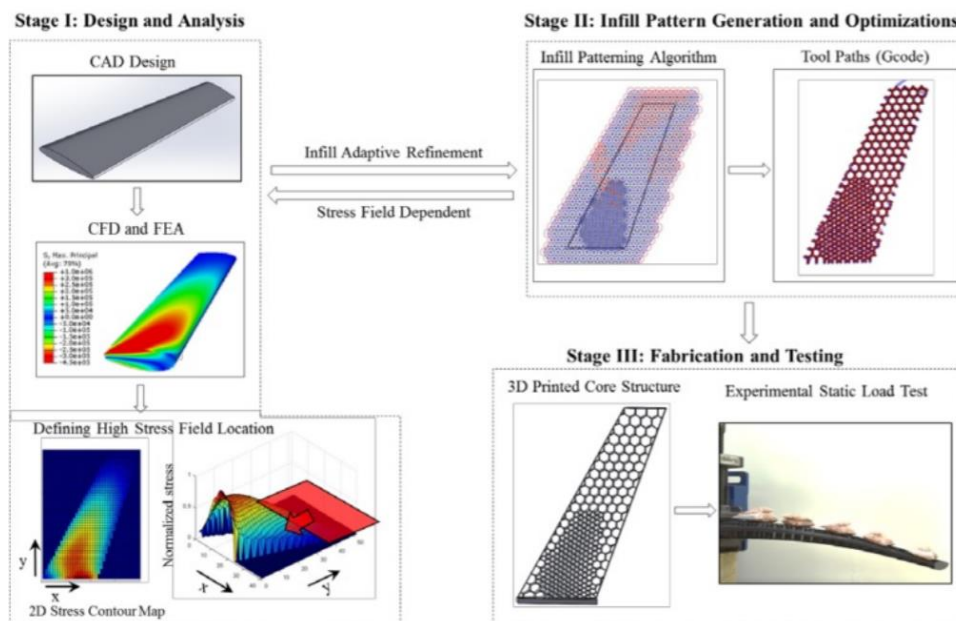


Figure 2.15. The integrated design approach for the infill patterning of an airfoil based on internal stress [13].

Oerlikon and RUAG Space cooperate in qualifying an optimized spacecraft bracket installed on a fairing presented in Figure 2.16. Topology optimization and manufacturing with additive manufacturing reduce cost by 25% and weight by 50%

[12]. This presents the strong capability of coupling topology optimization and additive manufacturing skills of companies.

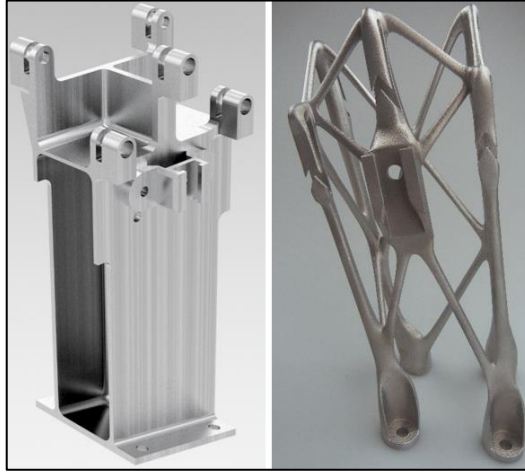


Figure 2.16. A bracket installed on a spacecraft developed by Oerlikon and Ruag Space (a) Conventional machining (b) Additive manufacturing after topology optimization [12]

Yiğitbaşı [35], after measuring the tensile properties of cylindrical Ti-6Al-4V tensile test specimens additively manufactured by EBM, the topology optimization is carried out for an aerospace structural fitting shown in Figure 2.17, which depicts before and after optimization. As a result of the optimization, 40% weight reduction is achieved without losing the fitting mechanical performance.

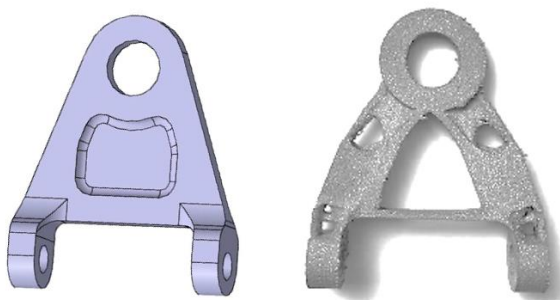


Figure 2.17. Aerospace fitting before and after topology optimization [35]

2.6 Conclusion

With this literature review, firstly, brief information about the historical development of additive manufacturing is given. Then, the definition of additive manufacturing is made, and different methods and materials used in additive manufacturing are discussed. Since this research will be focusing on the EBM method and the Ti-6Al-4V alloy, informative studies are conducted on both. When scientific studies on the EBM method are examined, it is observed that the biggest drawback in additive manufacturing methods is unsolicited pores. Various studies are examined, and their effects on the final product are also investigated. As a result of this literature review, it is evaluated that due to its rapid production method and its ability to produce complex geometries quickly, the additive manufacturing can be used for production purposes after the aerospace structural parts are lightened by optimization. In addition to the weight reduction works, it is evaluated that assemblies consisting of many parts can also be produced in one piece. Finally, it is also observed that additive manufacturing can be used to produce aerospace structural parts after determining the material properties and the effect of the pores formed during production.

CHAPTER 3

EXPERIMENTAL INVESTIGATION ON MECHANICAL PERFORMANCE OF ELECTRON BEAM MELTED Ti-6Al-4V

In this chapter, tensile, high cycle fatigue and pin bearing test specimens manufactured by electron beam melting and the mechanical performance results obtained from the test campaigns will be explained. Prior to the details of the test campaigns, some introductory explanations will be given about the Arcam Q20 Plus EBM (Electron Beam Melting) machine used during manufacturing of all specimens and the HIP (Hot Isostatic Pressing) process used for post-treatment.

3.1 Additive manufacturing of test specimens with electron beam melting and hot isostatic pressing

Arcam [3] states that the Arcam Q20 Plus machine is developed especially for aerospace frame parts. The machine properties used in this research are retrieved from the manufacturer's website. The machine has 3000 W electron beam power and it generates a minimum electron beam diameter of 180 μm . While the beam is scanning, positioning time has a very small-time interval like 10 ms. The manufacturing volume is a cylindrical shape with 350 mm x 380 mm (diameter x height) dimensions. The base vacuum required for the beam to advance without hitting the gas atoms drops down to 10^{-4} mbar pressure. Due to the partial pressure of He, the manufacturing environment has a pressure of 4×10^{-3} mbar. Moreover, build directions considered in this study are depicted in Figure 3.1.

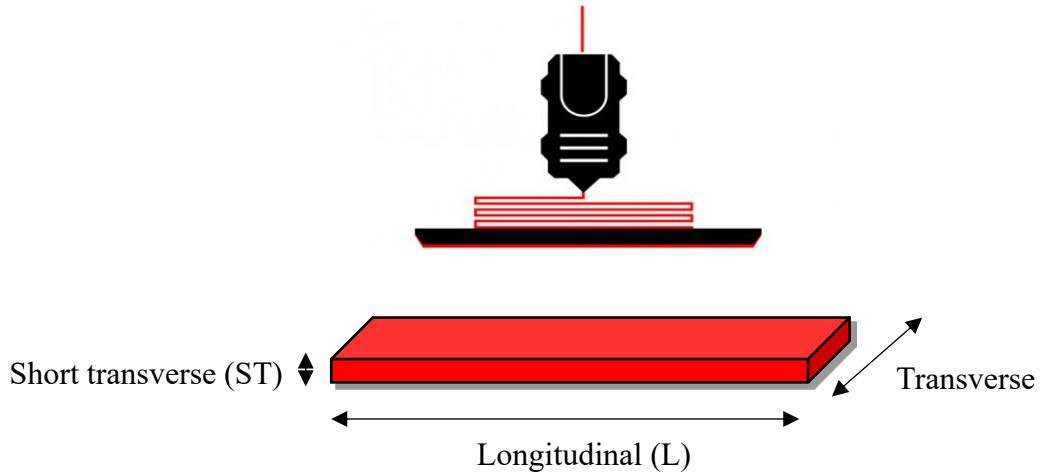


Figure 3.1. Build directions of a test specimen.

Figure 3.2, on the other hand, shows the actual machine and manufactured tensile test specimens in the same build tank used in this study. The specimens are built on a disc-shaped steel build plate. The temporary support structures are also used to underpin the surfaces facing down the build plate. Some residues of support structures can be seen in Figure 3.2 (b) after coarse post-processing.

In this research, ASTM E8 [36] tensile, ASTM E466 [37] fatigue, and ASTM E238 [38] pin bearing test standards are used as a reference and 30 test specimens for each campaign are manufactured in the same build tank in total three manufacturing attempts. Test specimens are built by melting Ti-6Al-4V grade 5 powder [3], which has spherical geometry with 45-106 μm diameter. Half of the test specimens are grouped “as-built” condition, and the remaining specimens are post-treated by Hot Isostatic Pressing (HIP) after surface machining.

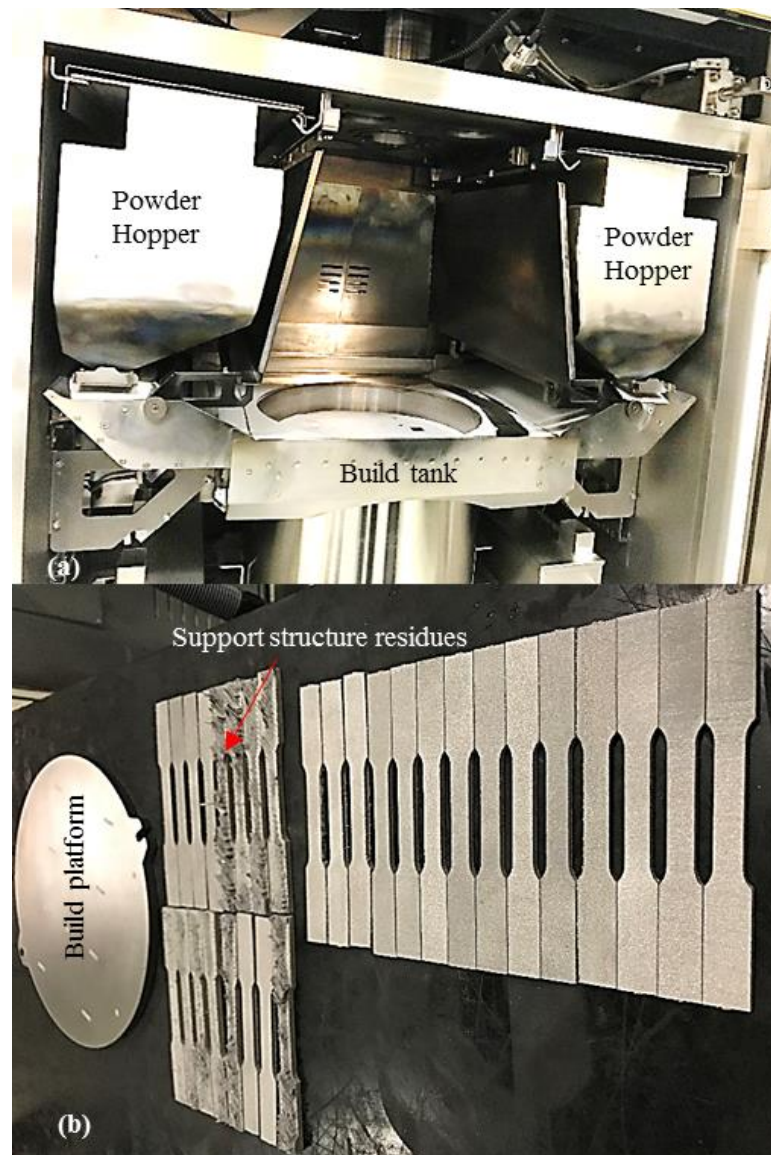


Figure 3.2. Arcam Q20 Plus machine and manufactured test specimens. (a) Interior view of the machine (b) Manufactured tensile test specimens and build platform.

Electron Beam melting method results in poor surface quality since melting pool temperature is very high. The powders in the neighborhood of the desired contour are sintered to the surface due to the high melting pool temperature, then; a porous surface is obtained. This porous surface may affect the test results. Surface machining is decided to be performed on test specimens to decrease the effect of

surface quality. Effect of manufacturing direction and HIP will be more distinguished by this strategy.

In addition to the porous surface, temporary support structures cause material discontinuity at the surface region. Only longitudinal specimen surfaces are not affected by support structures since there is a support structure at only one non-functional end of the specimen. Machining is performed at the gauge length region carefully. After machining all test specimens, the thickness, width, and hole diameter of each specimen are measured by a caliper for later calculations. Following the surface machining, half of the specimens of each test type (15 for each test type, 45 total) are fetched to the HIP facility located at TÜBİTAK MAM premises. The HIP process is required for closing the pores which are emerged during additive manufacturing.

Generic HIP facility is shown in Figure 3.3. HIP volume has a 23 cm diameter and 70 cm height chamber and the chamber of it consists of three separated stages. 45 test specimens are laid down in two stages of the HIP chamber. HIP chamber and laid test specimens are shown in Figure 3.4.

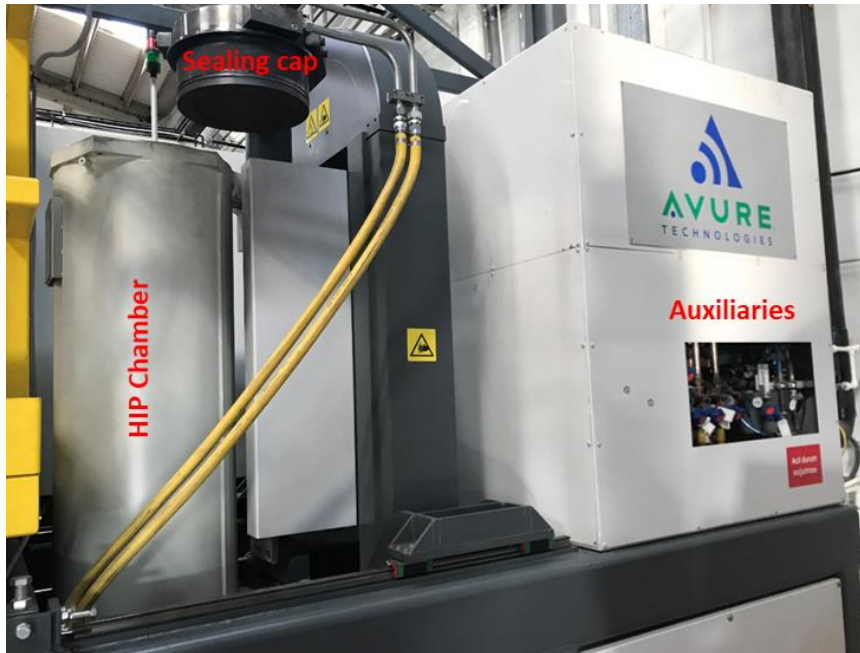


Figure 3.3. HIP facility.

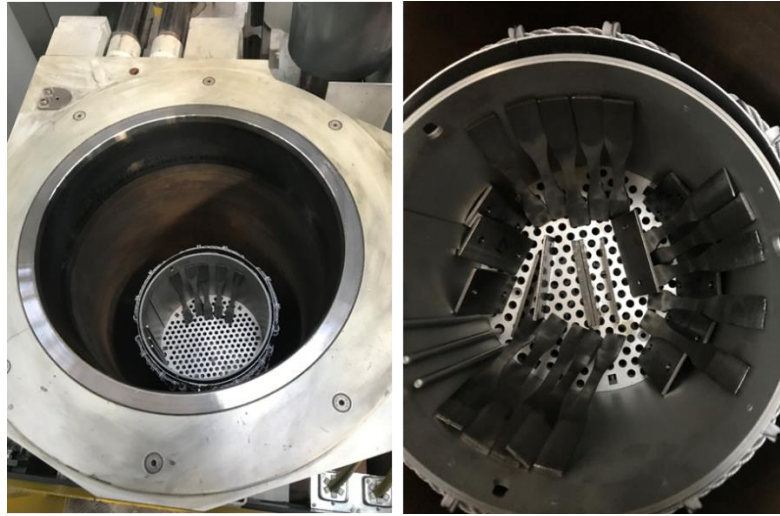


Figure 3.4. HIP chamber and laid test specimens at the last stage, respectively.

Following the specimen allocation, the sealing cap is closed and tightened. Humid air inside the chamber is drained several times and pressurization is realized by inert Argon gas. The HIP process is realized at 100 MPa pressure and 920°C temperature for two hours. Process consists of three phases depicted in Figure 3.5. Dimensions of test specimens are measured before and after the HIP process. However, no significant deviance can be detected before and after HIP.

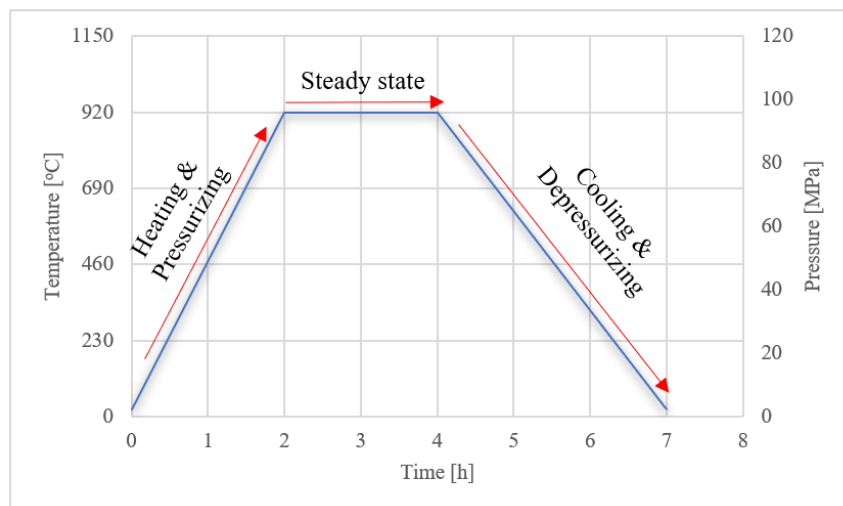


Figure 3.5. Applied HIP process.

3.2 Tensile test campaign

This section focuses on the elastic and plastic properties of Ti-6Al-4V alloy materials manufactured by EBM and imaging the internal structure with microCT. As a novel contribution, revealing the effect of build direction and HIP post-treatment are aimed. Ti-6Al-4V material can be used for airframe fittings instead of aluminum or steel material and has the advantage that it can be used together with carbon fiber composite parts without corrosion incompatibility. Although additive manufacturing and Ti-6Al-4V material provide some benefits such as rapid manufacturing without specific tools and manufacturing of corrosion-compatible material with carbon fiber composites, lightweight complex parts, mechanical properties of the end product are not sufficiently precise for aerospace applications. Consequently, aviation authorities also emphasize rules for certification of the aerospace structures manufactured by additive manufacturing. European Union Aviation Safety Agency (EASA) states that additive manufacturing methods can produce complex parts with engineering properties, which are highly material, process, and configuration dependent. This may generate significant variability if production is not governed by a strict process control documentation [39]. On the other hand, the determination of mechanical properties is also crucial for modeling and simulation purposes. Determination of elastoplastic properties of this type of material needs a long-term effort to simulate the propensity of damage for additively manufactured parts [40].

Mechanical properties of additively manufactured Ti-6Al-4V parts are affected by their microstructure, phases, grain content, grain sizes and shapes, and the presence of defects [25]. Grains have a dominant effect on the tensile properties; on the other hand, surface quality and imperfections such as internal porosity primarily affect the fatigue behavior of the additively manufactured parts.

Ti-6Al-4V is classified as a two-phase α - β alloy. The manufacturing process with its cooldown mechanism and additional heat treatment affects the α - β microstructure and the mechanical properties of the alloy. Draper et al. [5] have performed thorough research on Ti-6Al-4V alloy manufactured by Arcam A2X machine by a wide range

of tests such as tensile, high cycle fatigue, low cycle fatigue, fracture toughness, and fatigue crack growth at cryogenic, room, and elevated temperatures to qualify machine and method for aerospace structures. The results show that specimens have superior mechanical properties to conventional alloy. Although this comprehensive research qualifies the material and the Arcam A2X machine, statistical analysis for three build directions and HIP post-treatment dependency on tensile properties are not included in the report. The cooling mechanism of manufactured specimens during the EBM process is different according to build direction; therefore, mechanical properties are affected by the orientation of the manufactured part [41]. The authors have carried out a study by manufacturing test specimens using an Arcam AB EBM S12 machine in three orthogonal and arbitrary build directions to reveal the dependency of microstructure, tensile, microhardness, and fracture toughness properties on the build direction. The results conclude that grain structure has an acicular shape and columnar β -grains follow the build direction. The mechanical properties, including tensile properties, are also affected by build direction; because different cooling and solidification characteristics occur due to the area of cooling surfaces contacting the base plate [41].

However, a statistical evaluation was not performed in this particular research which is crucial for aerospace structures. Moreover, Tammas-Williams et al. [8] have proven that the pore size and location have a dominant effect in evaluating the fatigue life of EBM Ti-6Al-4V samples. Thus, in the present study, HIP post-treatment, a method used in powder metallurgy, is applied to diminish unsolicited pores and defects inside the structures. Tensile and fatigue properties are the two crucial mechanical properties for aerospace structures; therefore, a micro computerized tomography (microCT) imaging is conducted in the scope of this research to discover porosity according to the build direction and the effect of HIP post-treatment to remove undesired pores and defects. To this end, 30 pieces of ASTM E8 rectangular cross-section tensile test specimens are manufactured using the Arcam Q20 Plus EBM machine. All test specimens are manufactured in the same build tank of the machine, and three orthogonal build directions are considered. Since the surface

quality is not the scope of this research, all specimen surfaces are machined to discard the effect of surface roughness on the elastoplastic properties. Finally, half of the specimens are post-treated by the HIP to remove undesired defects and porosity inside the structure. The internal structures of six specimens are observed by microCT imaging, and tensile tests are conducted for the remaining 24 specimens. Following the microCT imaging and tensile test campaign, the elastoplastic properties of the specimens are evaluated with the support of the digital image correlation (DIC) technique to calculate stress-strain and Poisson's ratio data.

Consequently, these tensile properties are statistically analyzed whether elastoplastic properties are dependent on building direction and/or HIP post-treatment. The test data is also needed for a free-form design that uses topology optimization for an existing airframe fitting since commercial topology optimization tools generally use the assumption of isotropic material properties. Ti-6Al-4V alloy manufactured by Arcam Q20 Plus machine is qualified with superior strength and stiffness properties compared to conventional alloy. The isotropic behavior evaluated by statistical analyses is an essential outcome of this research. Moreover, the effect of the support structure on the unsolicited defects and porosity is also discovered by microCT imaging. HIP post-treatment remedies these defects and pores, furthermore resulting in a slightly coarser grain structure. Hence, a more homogeneous grain structure and a non-porous structure are obtained; more coherent and reliable tensile properties are resulted in by HIP post-treatment.

3.2.1 Methods and means of tensile test campaign

In this test campaign, ASTM E8 tensile test standard is used as a reference [36], and 30 test specimens are manufactured in the same build tank in total. Test specimens are built by melting Ti-6Al-4V powder, which has a spherical geometry within the range of 45-106 μm diameter. Half of the test specimens are grouped "as-built" condition, and the remaining specimens are post-treated by HIP after surface machining.

Specimens are manufactured in three different build directions. Dimensions of the specimens and three build directions are presented in Figure 3.6, and the manufacturing matrix for 30 test specimens is summarized in Table 3.1.

Table 3.1 Manufactured ASTM E8 tensile test specimen quantities.

| Build direction | Manufacturing condition | |
|------------------------|--------------------------------|------------|
| | As-built | HIP |
| Longitudinal (L) | 5 | 5 |
| Transverse (T) | 5 | 5 |
| Short transverse (ST) | 5 | 5 |
| Total quantity | 15 | 15 |

EBM method has a high melting pool temperature and volume compared to the SLM method. High-temperature results in rough surfaces due to the sintering of neighboring powder particles to the melted layers [42]. Thus, all test specimen surfaces are machined by milling to discard the effect of surface quality on tensile properties prior to the HIP post-treatment. Figure 3.7 schematically shows the reason for rough surface and manufactured test specimens before and after machining.

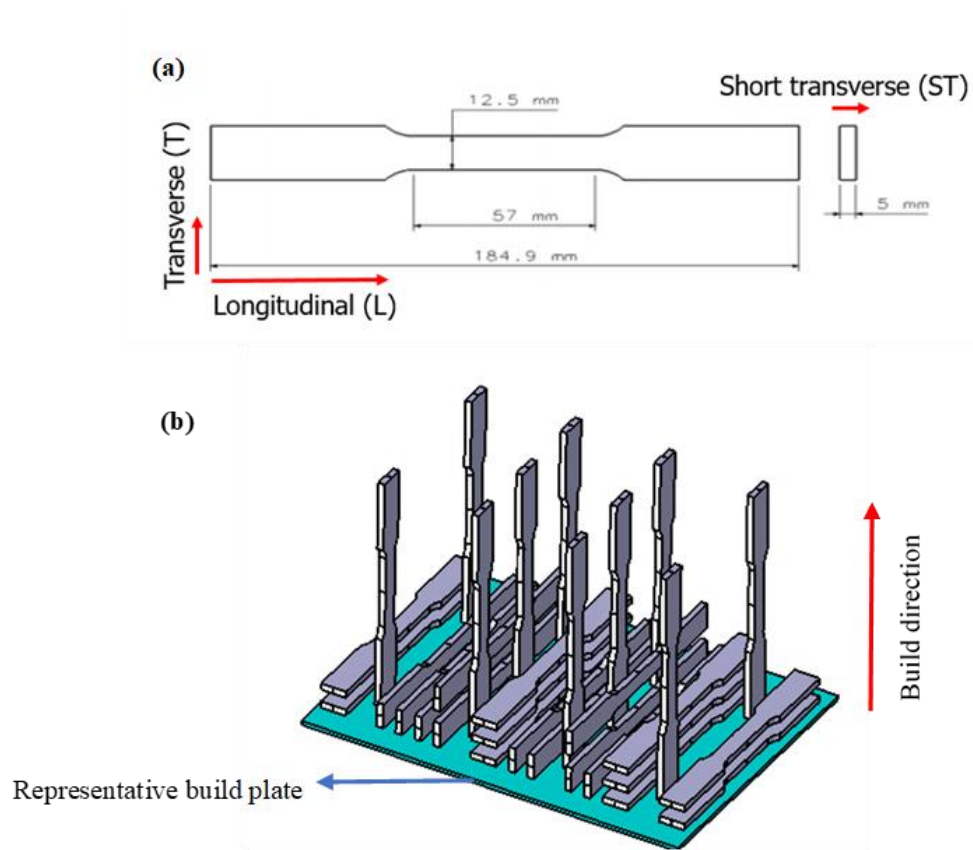


Figure 3.6. Tensile test specimen dimensions and build directions. (a) Specimen dimensions according to ASTM E8 and build directions (b) Specimen manufacturing layout in same build tank.

As stated before, half of the specimens are post-treated by HIP after the improvement of surface quality by machining. This post-treatment is performed in a chamber under 100 MPa pressure and 920°C temperature for 2 hours. The air inside the chamber is extracted and replaced by inert Argon gas before the conditioning of the chamber. The cooldown process after HIP is performed within 3 hours by natural cooling. HIP post-treatment is necessary to remove unsolicited pores and defects inside the structure, which is the main drawback of additive manufacturing. The reasons for defect formation can be categorized into two types; a meager energy input leads to improper melting or lack of fusion porosity, whereas a high-energy input causes keyholing [43]. The parts are exposed to HIP post-treatment just below

the β phase transition temperature. The research by Draper et al. [5] shows that HIP not only closes pores but also slightly coarsens the grain structure.

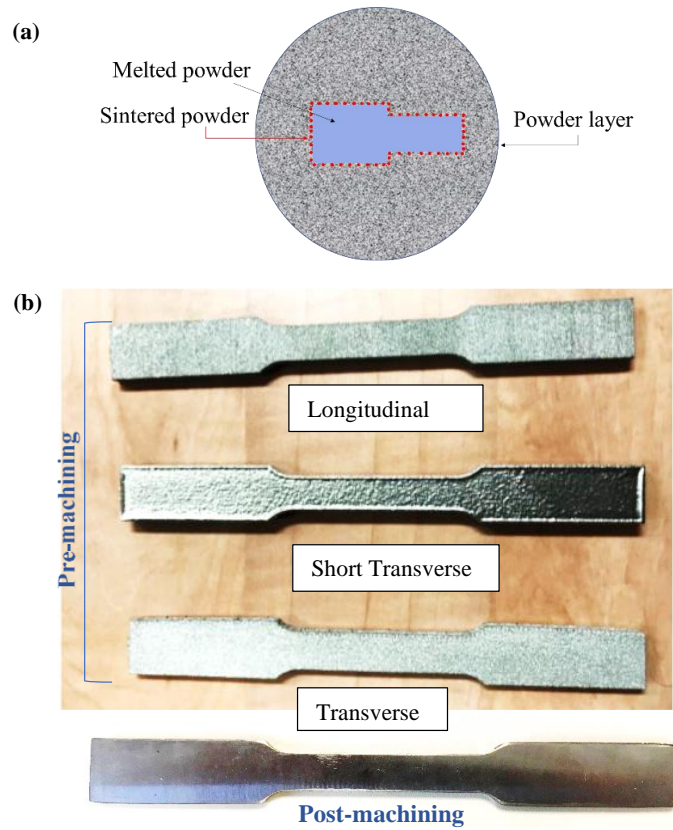


Figure 3.7. (a) Schematic for the cause of surface roughness (b) Pre- and post-machined specimens with build directions

Micro computerized tomography is a method that uses X-ray to obtain images of internal structure. It is a non-destructive observation method and is widely used in the additive manufacturing industry. Defects and their sizes, shapes, and locations, which affect the mechanical properties of the final part, can be determined by the micro computerized tomography (microCT) method [44]. Since the reproducibility of parts by additive manufacturing is not well-known, microCT provides information about each manufactured part's internal structure. The MicroCT imaging system comprises several sub-components: an x-ray tube, a radiation filter and collimator, a

specimen holder, and a screen made from a phosphor-detector/charge-coupled device (CCD) camera shown in Figure 3.8 [45]. Hundreds of images are captured as the specimen rotates around its axis, and then those captured images are converted to 3D images by a computer. The MicroCT imaging method is used to capture 3D internal images of six tensile test specimens. Each specimen is representative of a build direction and final condition. These six test specimens are also kept redundant for the tensile test campaign after microCT imaging.

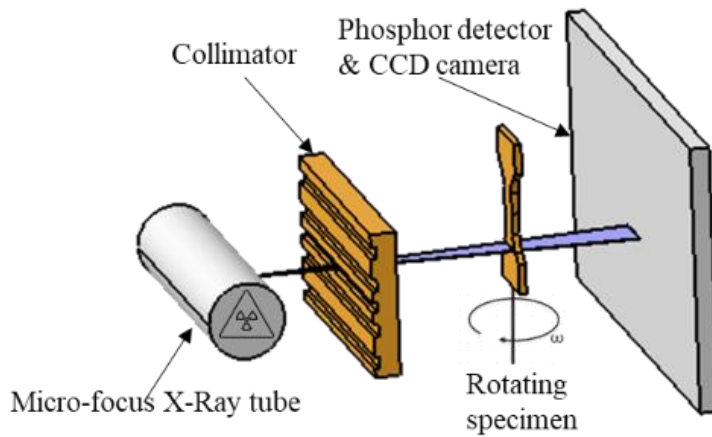


Figure 3.8. MicroCT imaging component schematic.

Before tensile tests, all test specimens are painted for digital image correlation (DIC) calculations. The painting is performed in two layers: first, a primer white paint is sprayed, and then black graphite paint is applied for speckles. Figure 3.9 depicts sample painted test specimens for DIC.

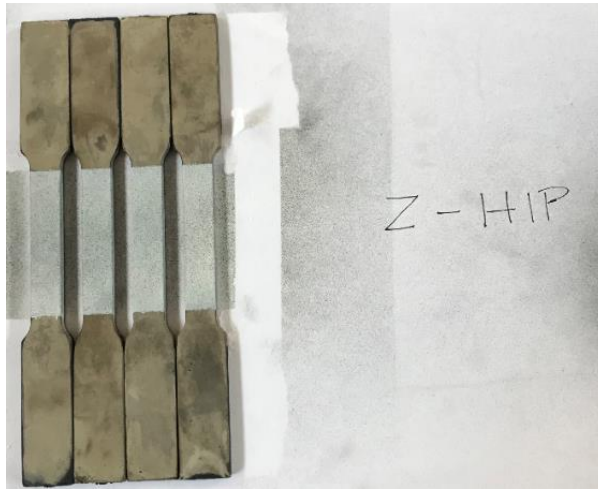


Figure 3.9. Sample painted tensile test specimens

Tensile tests are conducted by using an MTS machine with 333 kN static force capacity where an automatic controlled hydraulic jaws achieve the gripping of test specimens. A dual-camera system captures images during the whole test campaign for strain calculations. The test configuration is shown in Figure 3.10.

The tensile tests are carried out under room temperature conditions. Tensile test specimen grip length is calculated as 45 mm according to ASTM E8 standard. The tensile tests are conducted in a displacement-controlled manner at a 1 mm/min displacement rate according to the same standard. Furthermore, the displacement data acquisition rate is set as 10 Hz. Image capture for subsequent DIC analysis is started manually and simultaneously with the tensile test. The image capture rate of the dual camera is set to 1 frame/sec.

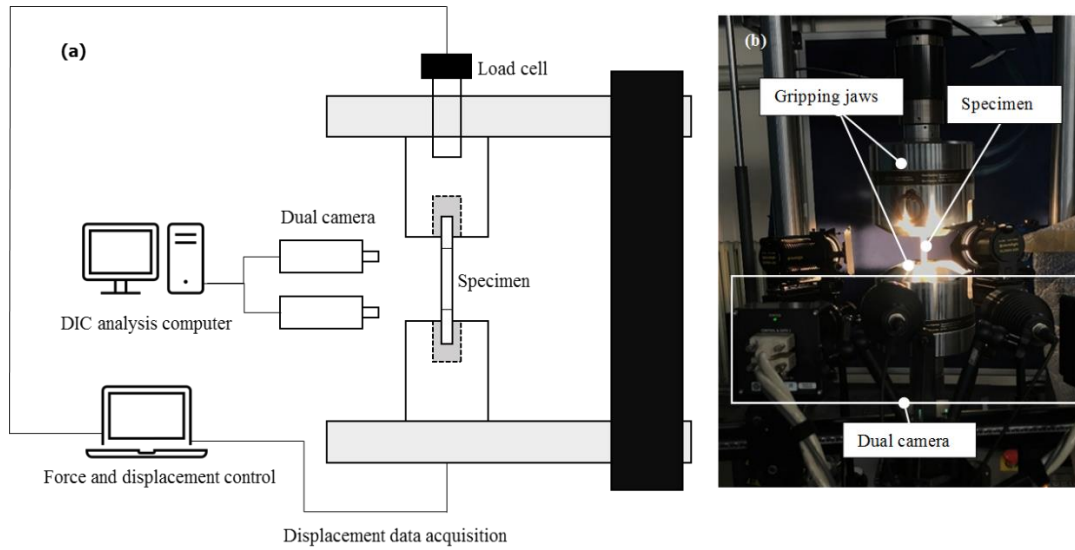


Figure 3.10. (a) Tensile test and DIC capture configuration (b) A view from the test campaign.

After completing the test campaign, captured images are post-processed by commercial GOM Correlate software in a 2D plane [46]. The strain data is calculated from pixels by locating a 50 mm extensometer to the gauge part of specimen images. Besides, two crossing 8 mm extensometers are also placed at the center of the gauge section to calculate the Poisson's ratio. Figure 3.11 shows the configuration of extensometers used during the DIC calculation. After obtaining the strain data from DIC analyses, synchronization with stress data is performed. Stress-strain curves of 24 specimens are generated by this method.

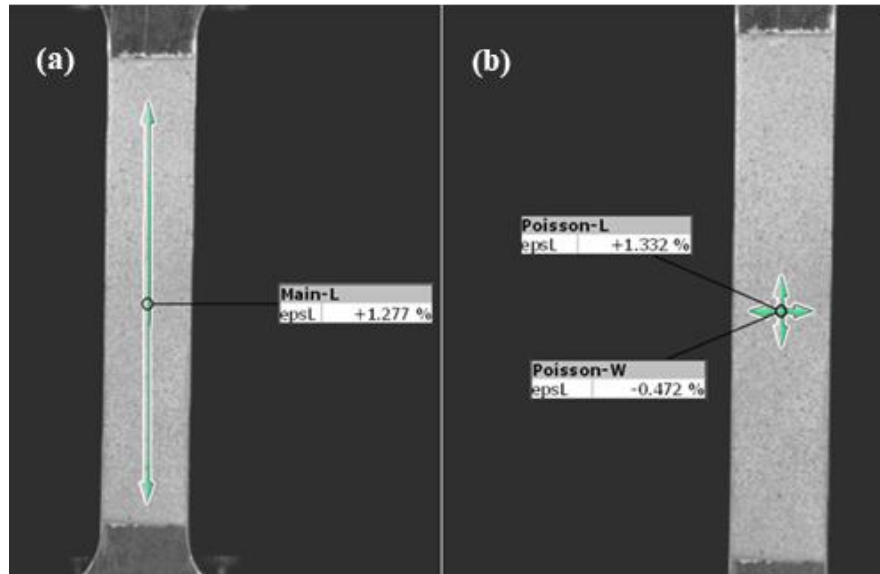


Figure 3.11. DIC extensometers to calculate strains by image processing.

(a) 50 mm extensometer according to ASTM E8 (b) Longitudinal and transverse extensometers to calculate Poisson's Ratio

Local strain distribution can also be obtained with DIC. Figure 3.12 shows the longitudinal strain distribution of a sample tensile test specimen just before the rupture. Strain accumulation is clearly observed where the fracture will occur.

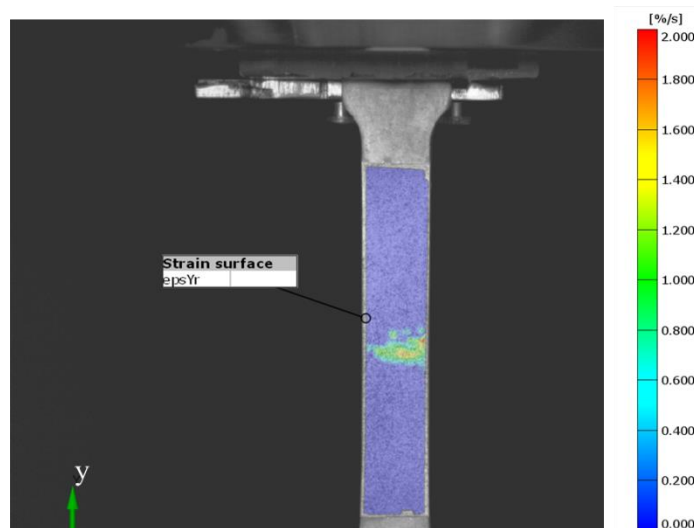


Figure 3.12. Local strain distribution before rupture.

3.2.2 Statistical analyses and results of tensile test campaign

Statistical analyses are performed to evaluate whether the elastic properties are isotropic or anisotropic. This information is required for the analysis of additively manufactured structures. Moreover, some methods, such as topology optimization, which is an iterative design process for generative design, generally utilize isotropic material assumption. Thus, this data will also shed light on structural analysis and structural optimization when needed. In addition to the elastic properties, the plastic properties are also studied to calculate the reserve factors of the final designs. However, due to the variance of test results, a statistical approach is required to evaluate the elastic and plastic characteristics.

Rice et al. [47] state that the Metallic Material Properties Development and Standardization (MMPDS) Handbook is recognized internationally as a reliable source of aircraft materials data for aerospace materials selection and analysis. MMPDS is used as a statistical analysis guide in this research as well. F-test and t-test from the technical report are used to determine if the resultant materials are isotropic or anisotropic. There are two types of tests to evaluate if specimens belong to the same family or not. F-test is used to analyze the variances of each group. If variances pass the test, then a t-test is followed to decide if the averages of specimens are in the same family or not. If F-test fails, there is no need to conduct a t-test. However, as specimen quantities of each group are limited, a t-test is conducted for groups that even fail F-test.

F-test, which is used to compare variances of two sample groups, is conducted for each manufacturing direction of as-built and HIP post-treated specimens. Table 3.2 summarizes the parameters that are used for F-test and t-test. Moreover, a 5% significance level is selected in this research to analyze the tensile test results statistically. This significance level is stated as sufficient in the MMPDS [47] guideline to lay within a 95% confidence level. The significance level is the probability of rejecting the null hypothesis. Currently, the null hypothesis for F-test and t-test is that the two groups are identical.

Table 3.2 Parameters of F-test and t-test

| | Group A | Group B |
|--------------------|-------------|-------------|
| Sample quantity | n_A | n_B |
| Standard deviation | s_A | s_B |
| Mean | \bar{X}_A | \bar{X}_B |

F-test starts by calculation of F value. F value is the ratio of variances of each group, i.e.,

$$F = \frac{s_A^2}{s_B^2} \quad 3.1$$

If the F value lies within a certain interval with a significance level $\alpha = 0.05$, then the variances of the two groups are accepted as identical. The upper and lower bounds of these values of this interval are retrieved from the table given in Table 9.10.3 of MMPDS [47]. The upper bound is $F_{0.975}$ (for $n_A - 1$ and $n_B - 1$ degree of freedom), and the lower bound is $1/F_{0.975}$ (for $n_A - 1$ and $n_B - 1$ degree of freedom). Rice et al. [47] define the degree of freedom as “Number of degrees of freedom for n variables may be defined as number of variables minus number of constraints between them. Since the standard deviation calculation contains one fixed value (the mean) it has $n - 1$ degrees of freedom.”

Following the F-test, a t-test is conducted to determine whether the averages of the two groups belong to the same family or not. Values of t are retrieved from Table 9.10.4 of MMPDS [47] for $\alpha = 0.05$ significance level. The absolute difference between the two groups $D_{\bar{X}}$ is defined as

$$D_{\bar{X}} = |\bar{X}_A - \bar{X}_B| \quad 3.2$$

If averages of two groups belong to the same family, then the $D_{\bar{X}}$ value should not exceed the u value, which is calculated by equation 3.3.

$$u = t_{0.975} s_p \sqrt{\frac{n_A + n_B}{n_A n_B}} \quad 3.3$$

If $D_{\bar{X}} \leq u$; then the averages of each group can be accepted as identical. $t_{0.975}$ has $n_A + n_B - 2$ degrees of freedom to read t -value from Table 9.10.4 of MMPDS [47], and s_p is determined by using the equation 3.4

$$s_p = \sqrt{\frac{(n_A - 1)s_A^2 + (n_B - 1)s_B^2}{n_A + n_B - 2}} \quad 3.4$$

If the modulus of elasticity values of all groups pass these statistical tests, then the elastically isotropic material assumption is validated and then the topology optimization can be conducted for weight reduction of an airframe fitting.

When tensile testing is performed, it is intended to derive a stress-strain curve. The point on this curve that corresponds to the maximum stress is called the ultimate strength (R_{pu}). Somewhere below the ultimate stress, the curve undergoes a sudden change, leaving the linear behavior. The point where this sudden change occurs is accepted as the point where plastic deformation starts and the point corresponding to 0.2% strain in industrial applications is accepted as yield strength ($R_{p0.2}$). An example graph showing yield and ultimate stress is given in Figure 3.13. The stress-Strain data is obtained by synchronizing the digital image correlation (DIC) data with the axial force data of the tensile test machine.

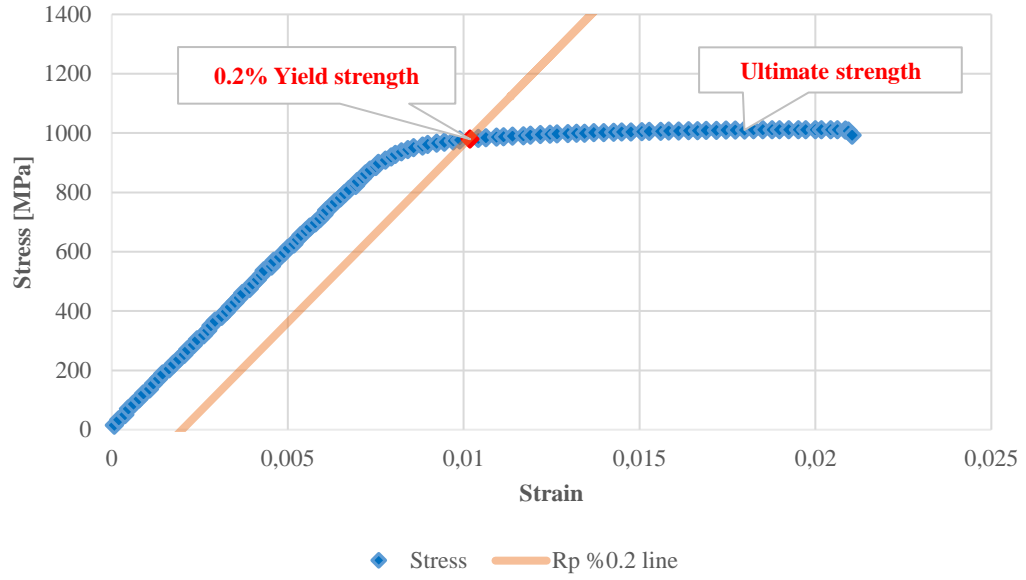


Figure 3.13. Extraction of 0.2% yield strength and ultimate strength sample

Poisson's ratio is calculated for each sample by taking the average of the ratios of the lateral and axial strain data read in both directions in the elastic region during the test by extensometers shown in Figure 3.11 (b). Figure 3.14 shows the Poisson's ratios calculated by dividing transverse strain to longitudinal strain in the elastic region as a result of a sample test. Simultaneous transverse and longitudinal strain data are used during calculations, and it is shown as a single data point in the graph after the division operation. Through these calculations, first, uncertain data set is not included since deviation occurs due to the insufficient certainty of DIC measurement at initial loading. Moreover, in the ASTM standard used to measure the Poisson's ratio [48], it is emphasized that the uncertainty in the strain measurement has a significant effect on the measurement of the Poisson's ratio, and it is recommended to evaluate the measurements after a particular load is applied in an example figure given in the reference. Besides, since the definition of Poisson's ratio is made in the elastic region [47], the region after the yield strength is not included in Poisson's ratio calculation.

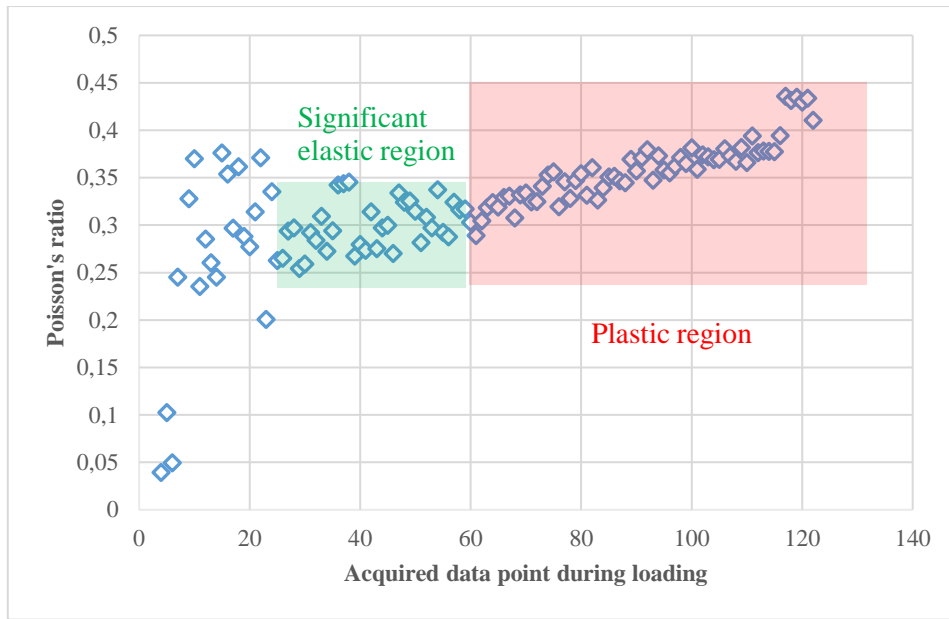


Figure 3.14. Averaging Poisson's ratio at elastic region

MicroCT images of 6 tensile test specimens and tensile test results of 24 specimens are analyzed in this section. MicroCT imaging provides information about the porosity distribution inside the specimens. Following the microCT image assessment, tensile test data is post-processed to calculate the modulus of elasticity (E), Poisson's ratio (ν), 0.2% yield strength ($R_{p0.2}$), ultimate strength (R_{pu}), elongation, and reduction of area (RA). "NH" suffix corresponds to as-built, and "H" is used for HIP post-treated specimens in figures and tables.

MicroCT images are evaluated before tensile testing to understand the effects of the HIP process and build directions. Six test specimens are scanned as three bundles; each consists of two specimens. Each imaging task takes approximately four hours to be completed. After completion of imaging, video clip files are obtained from scanning and post-processing by computer. Several longitudinal and lateral cross-sections are taken as references for observation. The cross-sections shown in Figure 3.15 represent the worst case of all layers of the aforementioned specimens. After observations, it is clear that the HIP process improves the unsolicited defect distribution. HIP removes almost all pores and defects inside the structure. Figure 3.15 shows lateral cross-sections of specimens with short transverse and transverse

build directions for as-built and HIP post-treatment cases. All cross-sections of HIP processed specimens lead to almost the same image without any pores. HIP post-treated specimens do not have any internal pores or defects. However, some surface defects may still exist after HIP. These surface defects may result from the surface milling process.

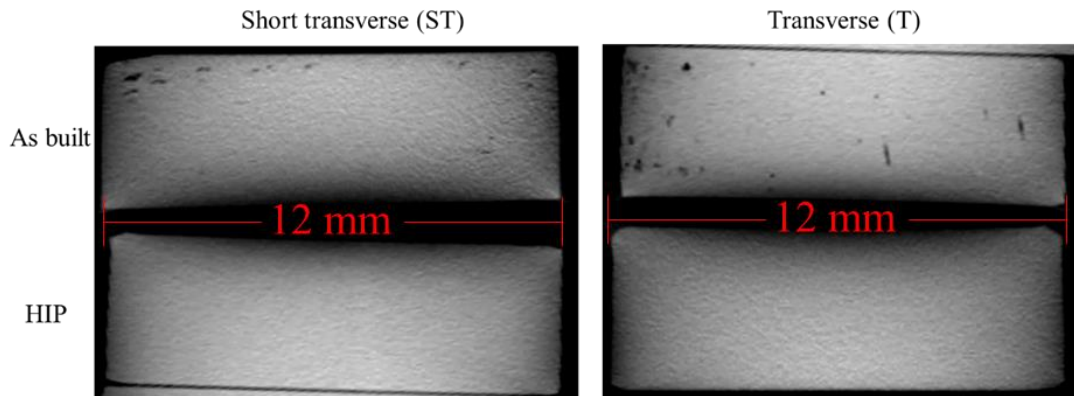


Figure 3.15. Representative lateral cross-sections of as-built and HIP post-treated specimens from microCT images.

Another essential observation from the microCT imaging is that dense pore distribution is formed near the support structure layers. Figure 3.16 depicts transverse (T) and short transverse (ST) built direction cross-section images of the gauge region of as-built tensile test specimens. Cross-sections of each specimen prove that layers close to support structures have a dense pore distribution. On the other hand, since the longitudinal built direction specimen does not have a support structure at the gauge section, this kind of pore distribution is not formed. As a result, aerospace structures manufactured by additive manufacturing must be post-treated by the HIP process to remove undesired pores and defects. Another outcome of microCT imaging is that support structures at high stress and strain regions of aerospace structures may result in unsolicited defects. Therefore, support structures at critical high-stress regions must be avoided, which must be considered during the design phase. Following the microCT analyses, four test specimens per build

direction and as-built and HIP conditions are tested using the test setup described in Figure 3.10.

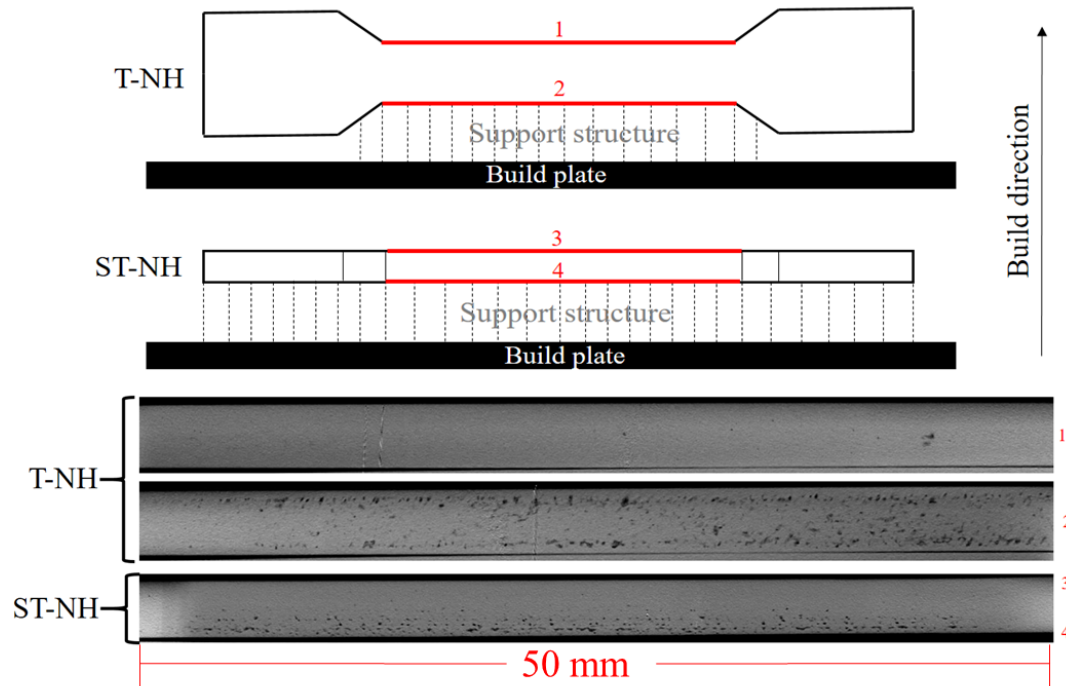


Figure 3.16. Internal defects and pores close to the support structure surface:
Schematic cross-section locations and microCT images.

Figure 3.17 summarizes the stress-strain curves from the tensile tests of as-built and HIP specimens. This graph is depicted to report the effect of the HIP process on the material's stress-strain response. Even though as-built specimens have a porous structure, as-built specimens have slightly higher strength values. However, ductility scatters significantly in as-built specimens due to porosity and the existence of defects. Since the shape, size, and distribution of pores are random, fracture also occurs randomly. Mohammadhosseini et al. [4] have studied tension, hardness, and fatigue characteristics of Ti-6Al-4V materials manufactured by EBM and applied HIP post-treatment. Moreover, grain structure has been analyzed by scanning electron microscope. At the end of the study, they observed that HIP increases grain dimensions. The increase in grain dimensions results in the ductile behavior of the

material. Hardness and yield strength decrease accordingly [4]. Although the pore quantity of as-built specimens is higher than HIP specimens, strength is also higher than HIP processed specimens (see Figure 3.17). This behavior can be explained by the fact that HIP specimens' grain sizes increase, by leading to more ductile and less fragile behavior.

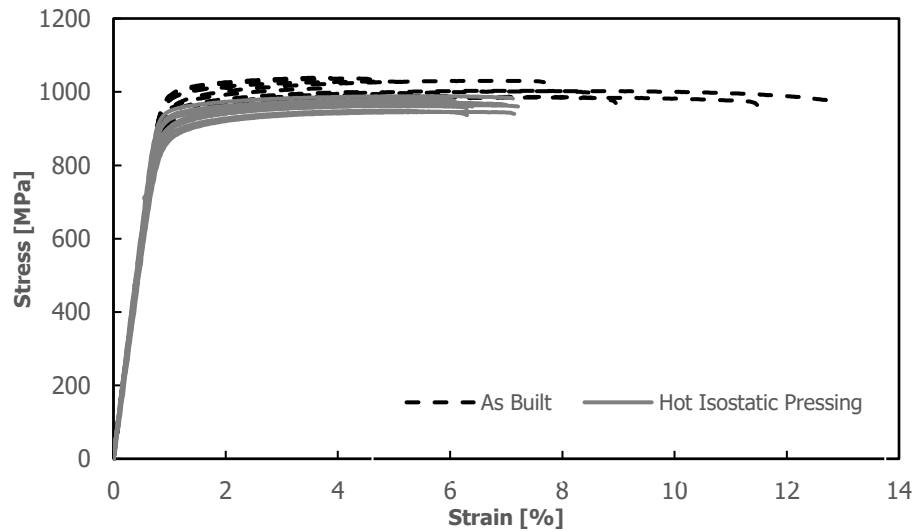


Figure 3.17. Effect of Hot Isostatic Pressing (HIP) on elastoplastic properties of Ti-6Al-4V alloy manufactured by EBM.

Figure 3.18 shows the comparison of stress-strain curves according to build directions for both as-built and HIP specimens. Yield and ultimate strength seem to have a significant direction dependency for as-built specimens; however, this dependency seems to diminish for HIP specimens. Furthermore, the elongation behavior of HIP specimens is more reliable when compared to as-built specimens, as HIP removes porosity. This result asserts that direction dependency of as-built specimen strength stems from pore density and distribution due to building direction and support structure layout. Figure 3.18 also proves that the strength of as-built specimens is slightly higher. Another conclusion that can be drawn from Figure 3.18 is the superior ductility of the short transverse as-built specimen. This behavior could be an outcome of pores leading to strain hardening due to stress concentration at pore circumference only for short transverse as-built specimens. Eudier [49] claims that

ductile porous metals may have more elongation due to strain hardening around pores and defects during tensile loading.

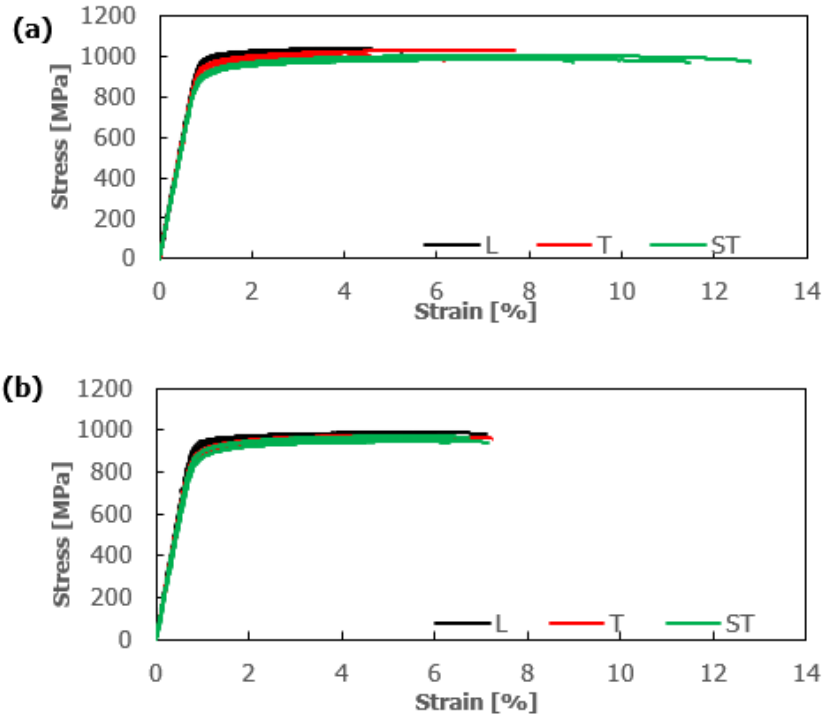


Figure 3.18. Build direction comparison, (a) As-built specimens (b) HIP specimens.

Figure 3.19 summarizes and compares the plastic properties (i.e. 0.2% yield strength, ultimate strength, and elongation) which are evaluated from the stress-strain curves of each specimen. Furthermore, area reduction is also calculated by caliper measurement of specimen cross-section dimensions before and after the test. It can also be seen from Figures (a) and (b) that the longitudinally manufactured specimens show a superior strength in comparison to transverse and short-transverse. In the literature, a similar observation was reported by Draper et al. [5] while the opposite behavior was presented in the study of Formanoir et al. [6]. It is observed from Figure 3.19 (c) and (d) that the variations in elongation and area reduction with build direction significantly decrease with the HIP post-treatment. Short transverse specimens have support structures on a widespread surface; therefore, the porosity

ratio to the whole volume is expected to be the highest compared to other build directions. Furthermore, short transverse specimen layers have more cooling areas and more support structures for conductive cooling. Thus, grain formation might be leading to more ductility compared to the other build directions which can also be observed from Figures (c) and (d). In conjunction with the effect of strain hardening of pores, high ductility is more characteristic for short transverse specimens.

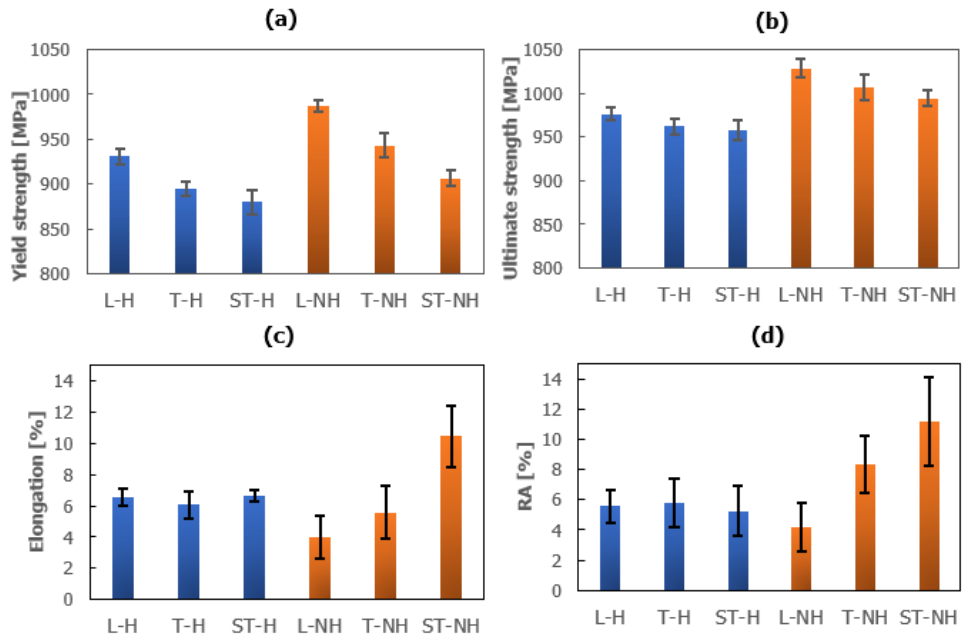


Figure 3.19. Averaged plastic properties and standard deviations; (a) Yield strength (b) Ultimate strength (c) Elongation (d) Reduction of area (RA)

Figure 3.20 presents the modulus of elasticity evaluated from each specimen's stress-strain curves and the Poisson's ratio calculated from the DIC analysis. Build direction and post-treatment dependency of elastic properties seem insignificant. However, the variance of Poisson's ratio for as-built specimens has a broader span compared to that of HIP specimens. Build direction-dependent behavior is not observed in elastic properties of both as-built and HIP specimens.

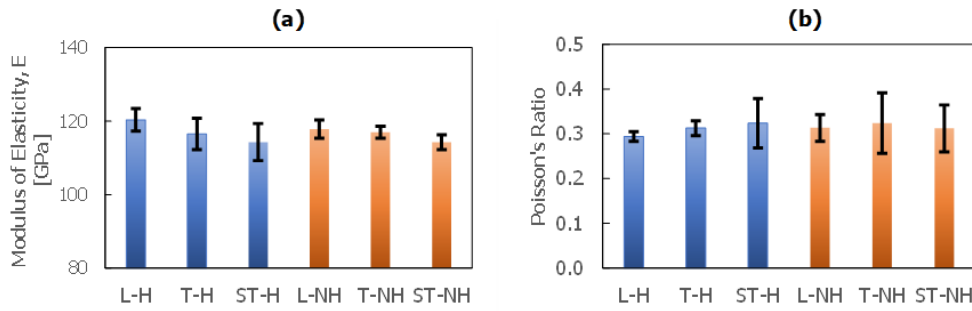


Figure 3.20. Averaged elastic properties and standard deviations, (a) Modulus of elasticity, (b) Poisson's ratio

Build direction and post-treatment dependency are also analyzed by F-test and t-test statistical methods. The F-test is used to compare variances of groups, and the t-test is used to compare averages. Table 3.3 presents the cross-comparison results of different groups. The green color corresponds to the groups that pass both the F-test and t-test, while the yellow represents the cases that fail the F-test but pass the t-test. Finally, the red color means the failure of both tests. If a property has a green color, then two groups are accepted as identical. The modulus of elasticity of all groups is identical; therefore, the material can be assumed as elastically isotropic. Hence, the topology optimization method can be applied to the target airframe part. However, there is a slight difference between Poisson's ratios of the longitudinal and short transverse samples among all groups. This difference in Poisson's ratio may cause slight deviations in the stress calculations of horizontally manufactured thin walls, which should be considered in the structural analysis. Furthermore, 0.2% yield strength values are not identical; therefore, after topology optimization, reserve factors should be calculated according to build direction strength values. Elastic properties for HIP post-treatment and as-built conditions are almost the same, but plastic properties vary significantly. The difference in yield strength also should be considered during reserve factor calculations after structural analysis or topology optimization re-analysis.

Table 3.3 F-test and t-test results of two groups.

| Group 1 | Elastic Properties | | Plastic Properties | | | | Group 2 |
|---|--------------------|---|--------------------|-----------------|----|------------|---------|
| | E | ν | R _{p0.2} | R _{pu} | RA | Elongation | |
| HIP Specimens-Build Direction Comparison | | | | | | | |
| L-H | ◆ | ◆ | ◆ | ◆ | ◆ | ◆ | T-H |
| L-H | ◆ | ◆ | ◆ | ◆ | ◆ | ◆ | ST-H |
| T-H | ◆ | ◆ | ◆ | ◆ | ◆ | ◆ | ST-H |
| As-Built Specimens-Build Direction Comparison | | | | | | | |
| L-NH | ◆ | ◆ | ◆ | ◆ | ◆ | ◆ | T-NH |
| L-NH | ◆ | ◆ | ◆ | ◆ | ◆ | ◆ | ST-NH |
| T-NH | ◆ | ◆ | ◆ | ◆ | ◆ | ◆ | ST-NH |
| Effect of HIP Within Build Directions | | | | | | | |
| L-H | ◆ | ◆ | ◆ | ◆ | ◆ | ◆ | L-NH |
| T-H | ◆ | ◆ | ◆ | ◆ | ◆ | ◆ | T-NH |
| ST-H | ◆ | ◆ | ◆ | ◆ | ◆ | ◆ | ST-NH |
| All specimens-HIP Effect | | | | | | | |
| As-Built | ◆ | ◆ | ◆ | ◆ | ◆ | ◆ | HIP |

Table 3.4 presents the average mechanical properties of HIP post-treated and as-built specimens from this test campaign, i.e., the average of three build directions and the mechanical properties of conventional AMS4911 (Ti-6Al-4V alloy) from [47]. Moreover, the results of Facchini et al. [50] and Greitemeier et al. [7], which are obtained for specimens manufactured with a different EBM machine, are given for comparison purposes. The results are presented in Table 3.4 as average values regardless of the build direction. In addition to averages, standard deviations are also included in the table. Here, σ denotes the standard deviation. These results show that, additively manufactured Ti-6Al-4V material is approximately 6% stiffer than the conventional material. The yield and ultimate strengths of HIP post-treated materials are thereabout 4% superior to conventional alloy. Moreover, as-built material yield and ultimate strengths are nearly 9% superior to the conventional alloy in comparison. However, elongation at fracture is almost 38% worse. Results of [50] and [7] are close to the conventional alloy with slightly more ductile behavior. Table 3.4 shows that additive manufacturing with Arcam Q20 Plus machine provides greater strength and stiffness properties but less ductility to the final part compared to the conventional alloy and other machines.

Table 3.4 Comparison of elastoplastic properties with build direction independent studies and conventional AMS4911 Ti-6Al-4V alloy

| | Test results | | [50] | | [7] | | AMS4911 [47] |
|--------------------------------------|------------------|------------------|------------------|----------------|------------------|-----------------|--------------|
| | HIP | As-built | HIP | As-built | HIP | As-built | |
| E $\pm \sigma$ [GPa] | 117.0 \pm 4.0 | 116.3 \pm 2.0 | 117 \pm 4.0 | 118 \pm 5.0 | - | - | 110.3 |
| $\nu \pm \sigma$ | 0.31 \pm 0.03 | 0.30 \pm 0.07 | - | - | - | - | 0.31 |
| R _{p0.2} $\pm \sigma$ [MPa] | 901.6 \pm 23.9 | 945.3 \pm 34.2 | 795.0 \pm 10.0 | 830 \pm 5.0 | 774.0 \pm 15.6 | 868 \pm 18.6 | 868.7 |
| R _{pu} $\pm \sigma$ [MPa] | 965.3 \pm 12.4 | 1010 \pm 23.8 | 870.0 \pm 10.0 | 915 \pm 10.0 | 896.0 \pm 11.6 | 972 \pm 111.7 | 923.9 |
| Elongation $\pm \sigma$ [%] | 6.4 \pm 0.6 | 6.7 \pm 3.1 | 13.7 \pm 1.0 | 13.1 \pm 0.4 | 18 \pm 0.5 | 15.0 \pm 0.0 | 10.6 |

In addition to comparing the overall results, a comparison is also carried out with the studies of Memu [51] and Yiğitbaşı [35], in which the results of the cylindrical specimens are manufactured vertically and horizontally with the same Arcam Q20 Plus machine. Moreover, the results of rectangular cross-section samples produced by Mohammadhosseini et al. [4] on another EBM machine for only horizontal directions are also compared. All these comparisons are presented in Table 3.5. The results of Memu [51] show slightly more strength and slightly ductile results. The results of Yiğitbaşı [35] exhibit close strength properties, but unexpectedly they also show high elasticity and ductility properties. This difference is thought to be sourced from the small number of samples or the measurement methodology.

Table 3.5 Comparison of elastoplastic properties with regard to build directions.

| | | | Test results | [51] | [35] | [5] | [4] |
|----------|------------|-------------------------|--------------|------|-------------|-------------|------------|
| As-built | Vertical | E [MPa] | 117.8±2.2 | - | 152.7 | 121.6±3.3 | - |
| | | v | 0.31±0.03 | | - | - | |
| | | R _{p0.2} [MPa] | 986.6±6.3 | | 942.1 | 995.7±30.2 | |
| | | R _{pu} [MPa] | 1028.8±10.7 | | 1023.7 | 1088.2±41.6 | |
| | | Elongation [%] | 4.0±2.1 | | 12.0 | 19.0±4.1 | |
| | Horizontal | E [MPa] | 115.6±2.1 | - | 139.5±17.45 | 118.3±0.5 | - |
| | | v | 0.29±0.08 | | - | - | |
| | | R _{p0.2} [MPa] | 924.6±21.3 | | 874.9±6.8 | 961.7±11.3 | |
| | | R _{pu} [MPa] | 1000.8±13.9 | | 996.0±3.6 | 1065.3±11.1 | |
| | | Elongation [%] | 8.0±2.9 | | 21.5±2.5 | 13.7±0.5 | |
| HIP | Vertical | E [MPa] | 120.3±2.7 | - | - | - | - |
| | | v | 0.29±0.01 | | | | |
| | | R _{p0.2} [MPa] | 930.6±9.1 | | | | |
| | | R _{pu} [MPa] | 976.6±8.0 | | | | |
| | | Elongation [%] | 6.6±0.5 | | | | |
| | Horizontal | E [MPa] | 115.4±4.2 | | | | - |
| | | v | 0.32±0.04 | | | | - |
| | | R _{p0.2} [MPa] | 887.1±13.4 | | | | 876.5±12.5 |
| | | R _{pu} [MPa] | 959.7±10.2 | | | | 978.0±9.5 |
| | | Elongation [%] | 6.4±0.6 | | | | 13.5±1.5 |

On the other hand, the results of Mohammadhosseini et al. [4] show a more ductile behavior, although they give close strength values for the horizontal build direction. All these results show that significant differences can be obtained in each study. Therefore, hundreds of test specimens are required to overcome these differences to obtain more reliable material properties.

In conclusion, a tensile test campaign is carried out to investigate the elastic and plastic behavior of Ti-6Al-4V alloys, which are manufactured by EBM. Fractured tensile test specimen photographs and overall test results are presented at Appendix A. In this campaign, 30 ASTM-E8 tensile test specimens are manufactured. Internal images of 6 samples in total, one representing each build direction and with or without HIP post-treatment, were visualized by micro-tomography. Strain data is calculated using the DIC method by capturing images during the tensile test, and thus stress-strain data could be extracted. Also, the Poisson's ratio could be calculated via DIC data.

The following results and scientific contributions have been obtained at the end of this research:

- Ti-6Al-4V alloy specimens which are manufactured by Arcam Q20 Plus machine, have isotropic elastic behavior for as-built and HIP post-treated conditions.
- Support structures cause dense unsolicited defects and porosity at the surface of the material. At high-stress regions and functional surfaces, support structures must be avoided. This aspect should also be considered during the topology optimization task.
- Hot Isostatic Pressing (HIP) post-treatment removes the pores almost completely. Removal of porosity provides a more coherent and reliable tensile behavior. Therefore, the HIP post-treatment must be mandatory for stress-critical aerospace structures.

- The build direction dependency of elongation and area reduction of additively manufactured Ti-6Al-4V significantly decreases with the HIP post-treatment.
- After structural analysis or topology optimization re-analysis, reserve factors (RF) must be calculated for airframe fitting. Since additively manufactured samples show build direction-dependent plastic properties, yield reserve factors should be calculated according to the build direction.
- MicroCT imaging can be used as a quality control method for critical airframe parts which are manufactured by additive manufacturing.
- The strength and stiffness of the additively manufactured Ti-6Al-4V alloy are higher than the conventional commercial one; however, it has worse ductility properties.

3.3 Fatigue test campaign

Lv et al. [52] have investigated aerospace structural failures on the research publications between 1990 and 2017 about. Investigation showed that 52% of structural failures are caused by fatigue. Figure 3.21 summarizes the failure percentages of this research. For this reason, fatigue calculations are necessary and require special attention for aerospace materials. As analysis engineers need to predict fatigue life, the materials used in the airframe must be tested, and their fatigue properties must be obtained and consequently, a fatigue test campaign is planned for this study. With this test campaign, fatigue life data of test samples produced in accordance with the ASTM E466 [37] standard is aimed to be obtained.

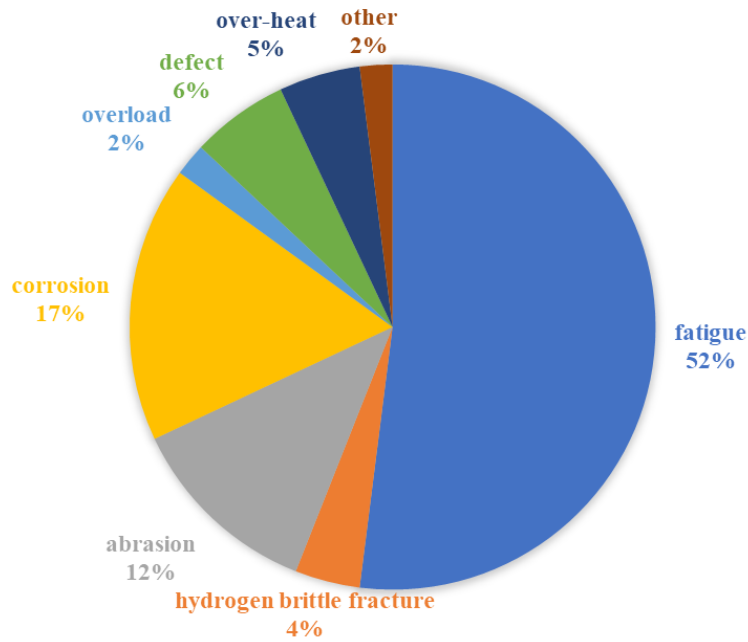


Figure 3.21. Airframe structural failure distribution [52].

The fatigue test campaign consisting of 24 test specimens is carried out at the tensile test facility. As a result of the test, the fatigue life is generally well below the fatigue characteristics presented in the literature. With the obtained results, life expectancy is estimated with the fatigue quality index (IQF) method, and it is determined that the material properties are coherent with these results.

3.3.1 Fatigue test methods and means

The typical approach for fatigue tests is to apply a cyclic load with constant amplitude to a test sample at a particular frequency. Then, cycles are counted up to the failure. If numerous specimens are tested with different stress ranges, results can plot a graph with cycles on the horizontal axis and stress levels on the vertical axis. Since cycles are vast numbers, log scale is preferred on the horizontal axis. Log scale may be preferred for the stress axis also. These curves are called S-N curves. S-N curves were first proposed by the German scientist August Wöhler while researching the 1842 train crash in Versailles, France [53]. Therefore, S-N curves are also called Wöhler Curves. Figure 3.22 shows how cyclic constant amplitude loading tests

generate S-N curves. According to this figure, fatigue failure tests can be grouped as low cycle fatigue, which occurs in the plastic region of the material, and high cycle fatigue which occurs in the elastic region of the material.

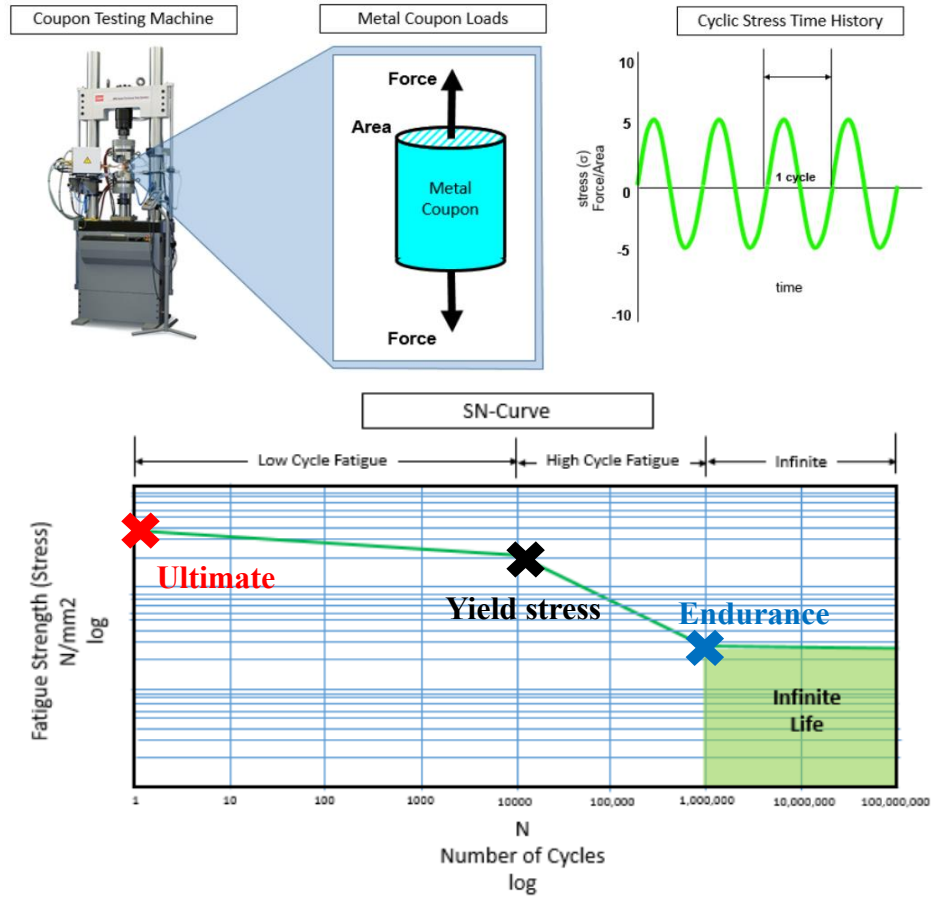


Figure 3.22. S-N Curve (Wöhler Curve) creation by coupon testing [53]

Although ferrous materials have infinite life behavior, some non-ferrous materials such as aluminum, magnesium, and copper alloys may not show a specific endurance limit. At this point, the Goodman-Haigh diagram is utilized to decide a cyclic stress time data is lay in an infinite life region for a material [54]. In order to create the Goodman-Haigh diagram, fatigue test results should be used as well as elastic and plastic properties obtained from tensile tests (see Figure 3.23). Figure 3.23 shows the mean value of constant amplitude stress loading on the horizontal axis. The difference between the applied maximum and minimum stress during the fatigue test is seen on the vertical axis. Endurance limit σ_e for each stress ratio is also obtained

from fatigue tests. An example of this endurance limit is the amplitude equivalent to 10^6 cycles. The yield strength σ_y and ultimate strength σ_u in the graph are obtained from tensile tests.

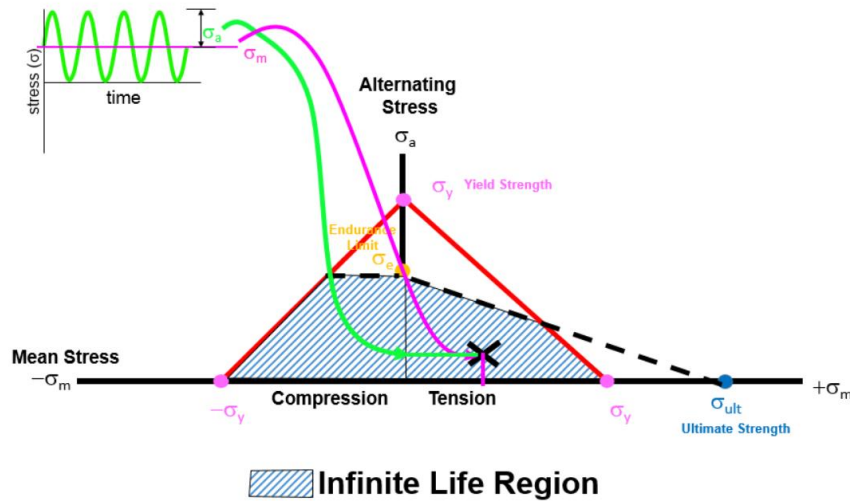


Figure 3.23. Goodman-Haigh diagram [54]

ASTM E466 Standard Practice for Conducting Force Controlled Constant Amplitude Axial Fatigue Tests of Metallic Materials standard [37] is selected as the basis of the fatigue test campaign. Test specimens are designed and manufactured by the guide of this standard. This test specimen type is intended to determine additively manufactured products' axial, unnotched, and elastic region fatigue strength at room temperature. The rectangular cross-section test specimen shown in Figure 3.24 will be used for fatigue tests.

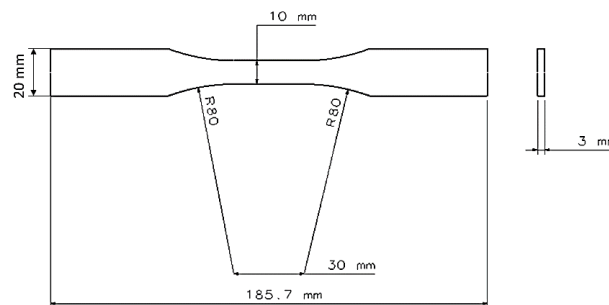


Figure 3.24. Specimens with tangentially blending fillets between the uniform test section and the ends.

Test specimens are planned to be manufactured as 15 qty. for as-built and 15 qty. for HIP post-treated. Longitudinal (L), transverse (T), and short transverse (ST) build directions are achieved by building all test specimens in a build volume as in the manufacturing of the tensile test specimens shown in Figure 3.6 (b).

The sample images of the fatigue specimens, removed after production, are given in Figure 3.25. Support structures are left on the T and ST to show their structure. After the support structures are removed, the samples are milled to remove the surface roughness. Additional care is taken to mill the gauge location where fatigue fracture is expected.

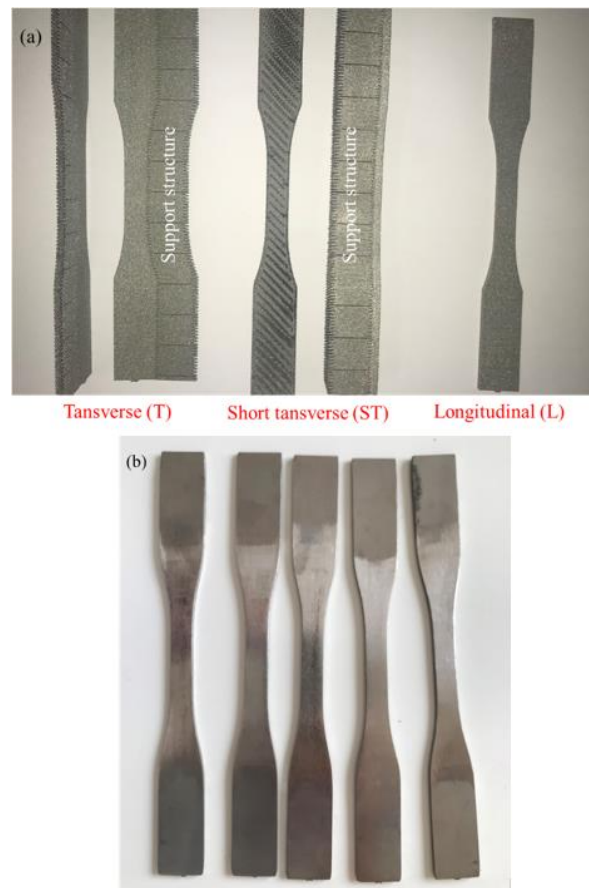


Figure 3.25. (a) Fatigue test specimen samples representing three build directions and support structures before removal, (b) sample machined specimens.

After the test specimens are additively manufactured and surfaces are prepared, fatigue tests are carried out by the fatigue testing machine. Figure 3.26 shows a constant amplitude force-controlled test setup for the whole fatigue test campaign. The fatigue test campaign is also performed in the MTS machine, where tensile and pin-bearing tests are performed. This test campaign is carried out under room temperature conditions. The control of the machine is based on a force control strategy. A constant amplitude, 20 Hz constant frequency force is applied to each specimen. The ratio between minimum and maximum amplitude is applied as $R=0.1$. In this case, the specimen always remained in tension conditions.

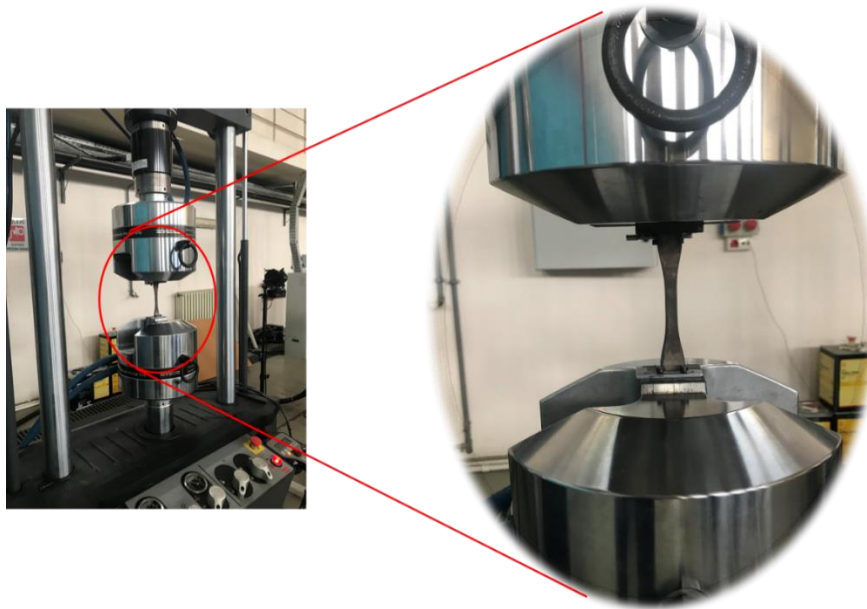


Figure 3.26. Constant amplitude fatigue test machine and test specimen.

Cycles up to the fracture of each test specimen are automatically counted by the data acquisition system of the test setup. Test specimens are removed from the setup following the fracture, and the fractured parts are stored. Pictures of fractured fatigue test specimens are presented in Appendix B. Finally, upon completion of the test, acquired force data is converted to stress by dividing the cross-section area.

3.3.2 Results of fatigue test campaign and modeling of fatigue life by Airbus IQF method using test data

HIPed specimens are named with the suffix -H, and as-built specimens are named as -NH in this section also. Four specimens for each build direction and 12 HIP post-processed specimens are tested first. The same strategy is followed for as-built specimens; however, additional 300 MPa maximum stress tests are also conducted to validate the fatigue life estimation calculations. Since HIP post-treatment will not be performed for the airframe fitting to be produced by additive manufacturing later, for fatigue calculations with the data obtained here, more sampling is desired for as-built specimens. Besides, project budget and schedule constraints and problems accessing the HIP facility are also decisive, and already manufactured specimens are used. Since as-built data showed similar elastic properties in tensile tests, after fatigue re-verification of as-built data, it is assumed that this verification would also be valid for HIP specimens. The overall fatigue life of all specimens is presented in Figure 3.27, and results are also accessible in Table B.1 in Appendix B. Results show that as-built specimens have better fatigue life properties insignificantly even with porous structures. Nevertheless, the log-log scale S-N curve slope will scientifically show the fatigue life behavior. Thus, an Airbus fatigue life estimation method, IQF method [55], will be utilized for additively manufactured specimens for both HIP and as-built conditions.

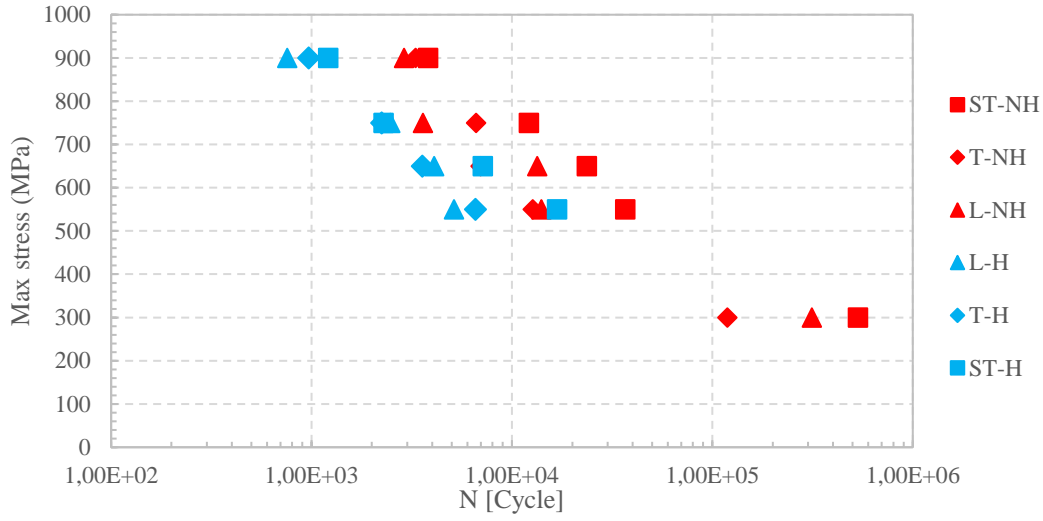


Figure 3.27. R=0.1 fatigue test overall scatter on S-N (Wöhler) curve

Fatigue life can be expressed as an approximation with equation 3.5 with the IQF method. IQF is the maximum stress at R=0.1 cyclic loading condition at 10^5 cycles. Airbus chooses 10^5 points from fatigue tests conducted at R=0.1 stress ratio, and fatigue life is approximately between 10^4 and 10^6 cycles for tested specimens. The detailed derivation of the equation is described in Appendix C. The meaning of IQF is depicted in Figure 3.28 also. IQF value can be extracted from test data where all parameters are known in equation 3.5, except IQF, then; test data from Figure 3.27 is used to extract IQF value for each specimen. Here, N denotes failure cycle, R ratio of min and max stress, S_{max} is maximum stress, p and q are constants. The p parameter is sourced from the properties such as material, surface treatment, thermal treatment, and chemical treatment, the scale of the specimen. It determines the behavior of the S-N curve. On the other hand, q is mainly affected by external effects like test and loading conditions; it usually takes values close to 0.5 [55].

$$N = 10^5 \cdot \left(\frac{IQF}{((1 - R)/0.9)^q \cdot S_{max}} \right)^p \quad 3.5$$

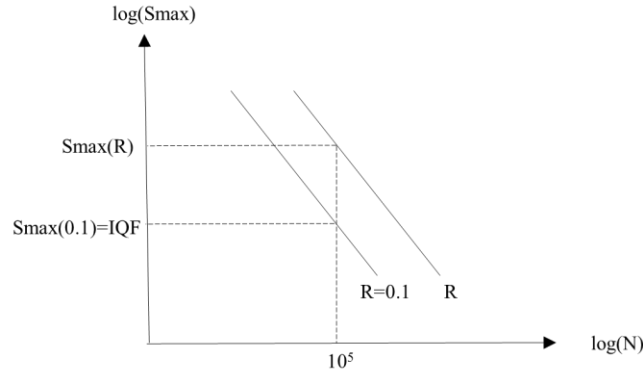


Figure 3.28. Description of IQF

Another empirical expression of IQF is given in equation 3.6. This equation is obtained from the results of numerous tests.

$$IQF = M \cdot E \cdot T1 \cdot T2 \cdot T3 \cdot T4 \cdot T5 \cdot \frac{C}{Kt} [MPa] \quad 3.6$$

In equation 3.6, M is a parameter that represents the effect of material, and E is related to the scale effect. Furthermore, parameters $T1, T2, T3, T4$ and $T5$ are responsible for the effect of surface treatment, mechanical treatment, the type of fasteners used for bolted and riveted assemblies, fastener installation conditions for bolted assemblies, and countersinking for bolted and riveted assemblies, respectively. Kt is the stress concentration factor and, C is the effect of the structural configuration type. $T1, T2, T3, T4$, and $T5$ are taken 1 when there is no particular effect. The derivation of the IQF method and the calculation or selection of C, E, Kt constants are presented in Appendix C. C is selected as 510 from the related configuration where test specimens are assessed as notched specimens. Kt is equal to 1.04 since radiuses are particularly kept large enough to diminish the stress concentration. E value is calculated as approximately 0.77.

Here, the p index in equation 3.5 and material constant M in equation 3.6 are the scopes of this research since they are affected by material properties. The p index also presents S-N curve behavior. Its value is determined by calculating the standard deviation of overall M values presented in Table 3.6 belonging to each as-built and

HIP post-treated group separately. M value is expected to be constant according to the formulation, then standard deviation test data is also expected to be minimum. Thus, standard deviations for each p -value extracted and the corresponding minimum standard deviation are selected for the p -index. Figure 3.29 gives a clue for the minimum deviation.

Table 3.6 Material constants and standard deviations

| Build Direction | Smax [Mpa] | As Built | | | HIP | | |
|-----------------|------------|----------|---------|--------|------|---------|-------|
| | | M | Average | Stdev | M | Average | Stdev |
| L | 900 | 1.08 | 1.02 | 6.50% | 0.98 | 0.95 | 6.52% |
| | 750 | 0.95 | | | 1.01 | | |
| | 650 | 1.10 | | | 0.96 | | |
| | 550 | 0.94 | | | 0.85 | | |
| | 300 | 1.02 | | | NA | | |
| T | 900 | 1.11 | 0.98 | 11.00% | 1.02 | 0.96 | 5.48% |
| | 750 | 1.08 | | | 0.99 | | |
| | 650 | 0.95 | | | 0.94 | | |
| | 550 | 0.92 | | | 0.89 | | |
| | 300 | 0.82 | | | NA | | |
| ST | 900 | 1.15 | 1.19 | 3.69% | 1.06 | 1.04 | 2.67% |
| | 750 | 1.24 | | | 1.00 | | |
| | 650 | 1.25 | | | 1.06 | | |
| | 550 | 1.16 | | | 1.05 | | |
| | 300 | 1.15 | | | NA | | |

The p -index value for as-built specimens and HIP post-treated specimens are found respectively as 4.5 and 5.5 from Figure 3.29. Airbus's p -index value for titanium alloys is already determined as 6.5, and the q value is equal to 0.6 for all alloys. The value of q will be used in calculations because it is not affected by material. It is worth mentioning a point here while calculating the standard deviation; all samples are taken as reference, and no evaluation is made according to the build directions. The minimum standard deviation of all data implicitly minimizes the standard deviation in each build direction group.

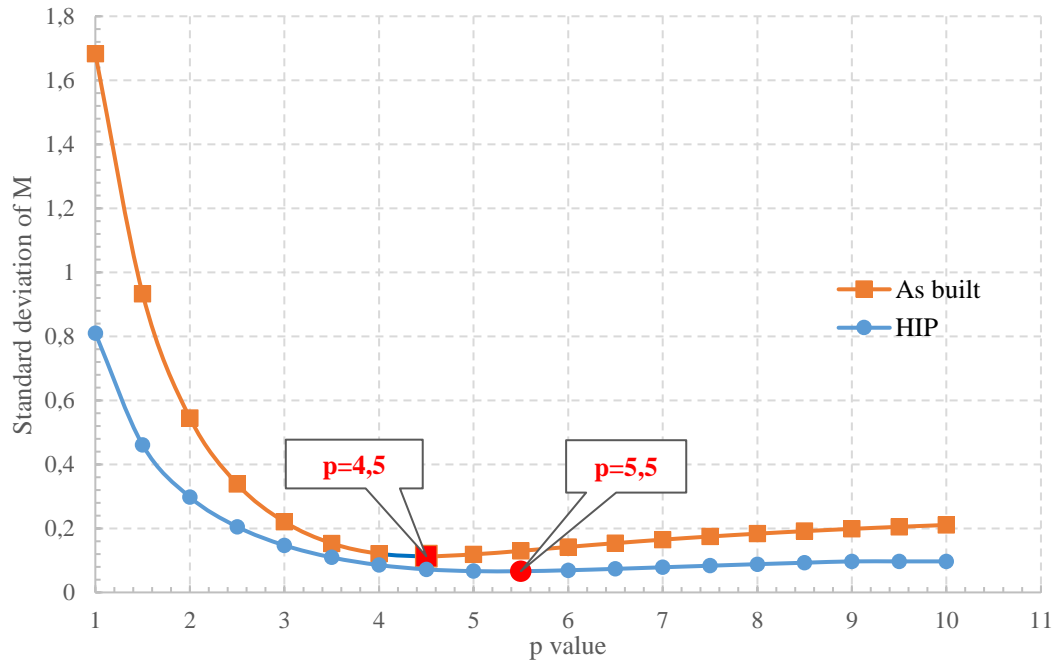


Figure 3.29. Change standard deviation of parameter M with respect to p value.

The p -index values obtained by this method and the p values used by Airbus for titanium alloys are compared in Table 3.7.

Table 3.7 Comparison of p -index values

| | As-Built | HIP | Airbus |
|------------|----------|-----|--------|
| p -index | 4.5 | 5.5 | 6.5 |

Upon completion of p -index value determination, average values of material constant M and standard deviations of each built direction are compared in Figure 3.30. The figure proves that material constants are well below the M values determined by Airbus, and the fatigue life of additively manufactured specimens are below the conventional Ti-6Al-4V alloy. When a comparison is made according to the build directions, the material constant values of the L and T directions give close results. In contrast, the ST production direction shows a better fatigue behavior. Another comparison is made for HIP and as-built cases, and it is found that as-built specimens show a better fatigue feature in terms of material coefficient.

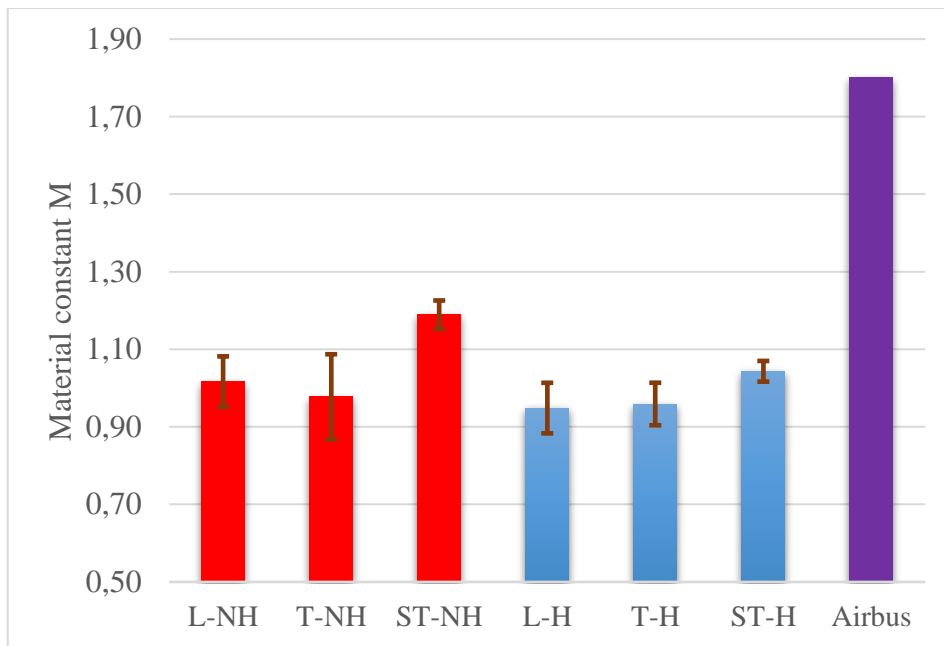


Figure 3.30. Comparison of material constant M for different build directions and Airbus Ti-6Al-4V material constant.

In order to validate the applicability of the IQF method, log-log scale S-N curves are created using the mean M value and standard deviations obtained using four test points in as-built specimens. The accuracy of fatigue life is evaluated by adding 300 MPa max stress data, which is the fifth test point on this curve. This evaluation is shown in Figure 3.31-Figure 3.33 for each build direction. The red square shows the 300 MPa test data. As can be seen in the graphics, the fatigue life estimation with the IQF method gives very consistent results.

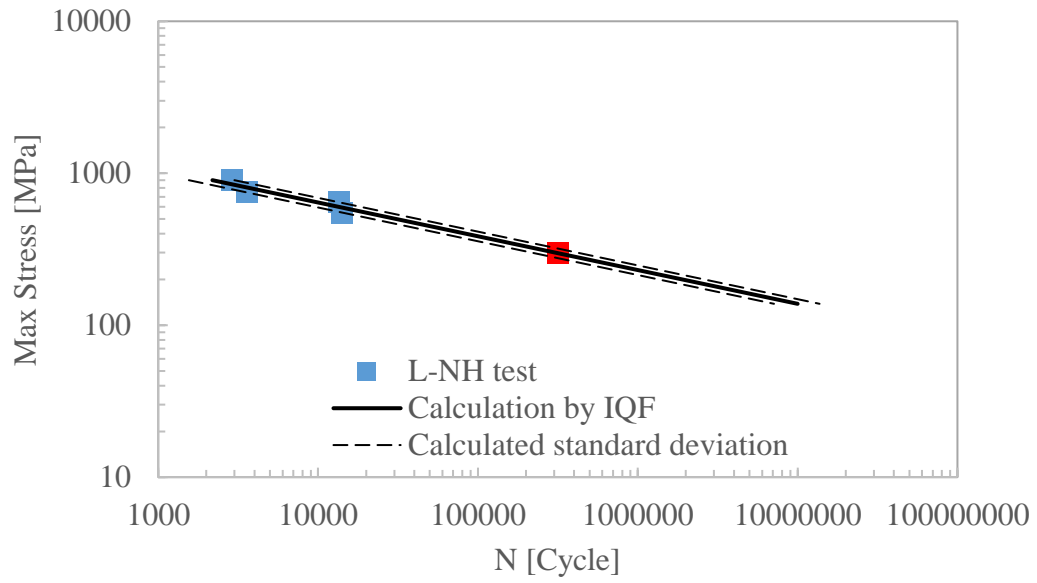


Figure 3.31. L-NH build direction fatigue life calculation using the first four data and the IQF method.

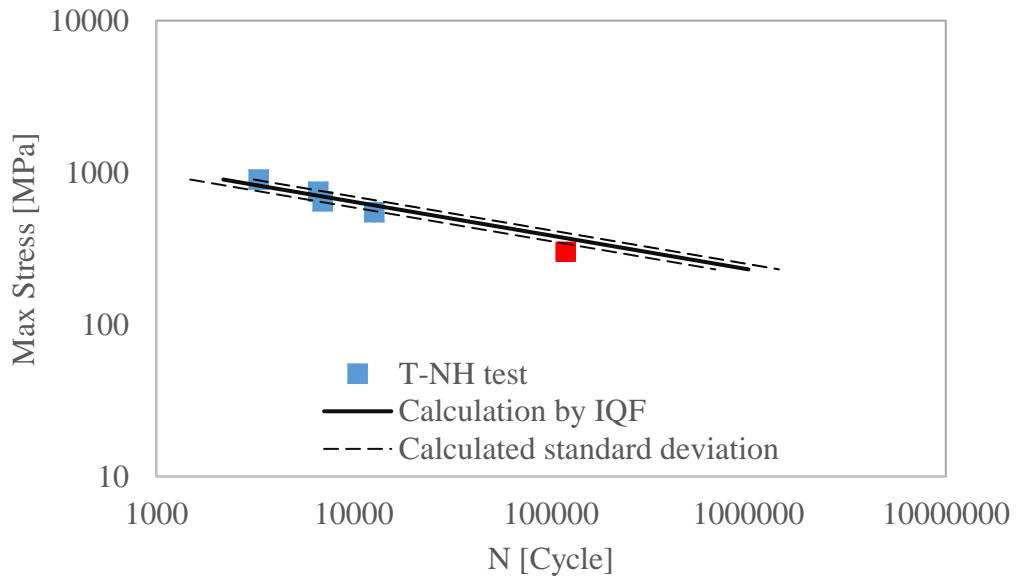


Figure 3.32. T-NH build direction fatigue life calculation using the first four data and the IQF method.

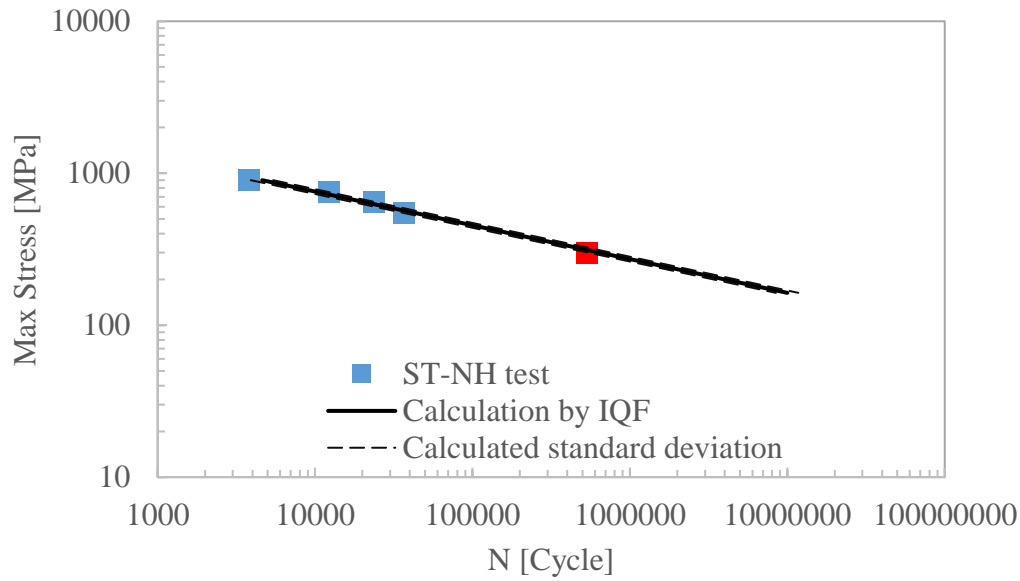


Figure 3.33. ST-NH build direction fatigue life calculation using the first four data and the IQF method.

Upon validating that the IQF method consistently results in fatigue life estimation, log-log scale S-N curves are also created for the HIP post-processed specimens. These curves can be seen between Figure 3.34 and Figure 3.36.

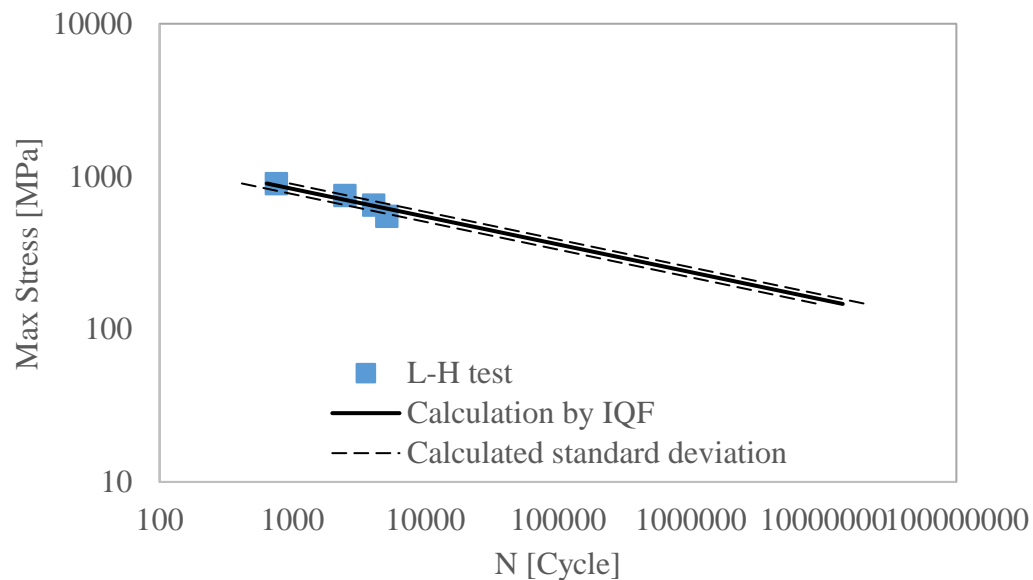


Figure 3.34. L-H build direction fatigue life calculation using the first four data and the IQF method.

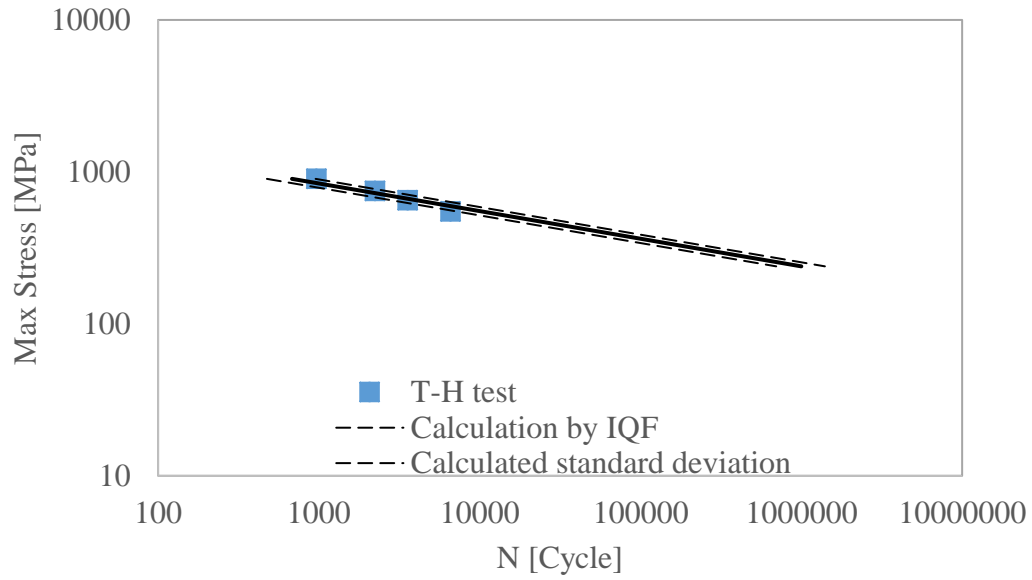


Figure 3.35. T-H build direction fatigue life calculation using the first four data and the IQF method.

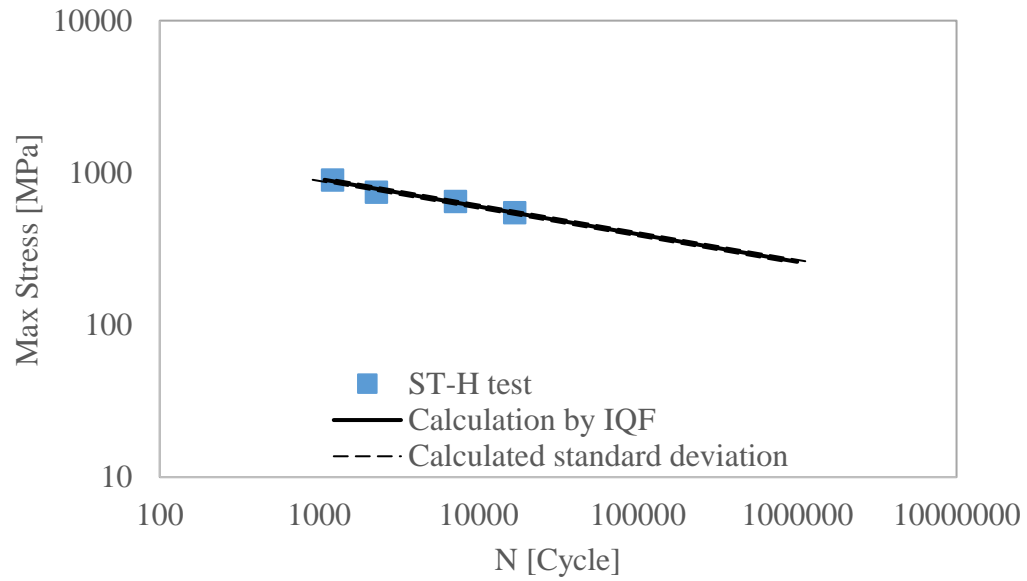


Figure 3.36. ST-H build direction fatigue life calculation using the first four data and the IQF method.

Finally, using the obtained p -index and material values, fatigue life strength is calculated for the as-built and HIP cases with the assumption of an infinite life of 10^6 cycles by equation 3.5. The Goodman-Haigh diagrams in Figure 3.37 and Figure

3.38 are derived using the fatigue life strength calculation and tensile test results. While deriving these diagrams, the minimum of elastic and plastic properties is used to be conservative. From the $R=0.1$ constant amplitude fatigue test results, fatigue strength S_{max} is calculated by IQF method for $R=-1.0$ ratio, which has zero mean stress, as 143 MPa for as-built specimens, while it is calculated as 146 MPa for HIP specimens. According to these diagrams, the σ_{lim} value, which means endurance limit of zero mean alternating stress, seems close to each other for as-built and HIP specimens. This conclusion is reached because the p-index value of HIP samples is higher than that of as-built specimens, although as-built specimens give higher cycle results for the same S_{max} values in the fatigue test results.

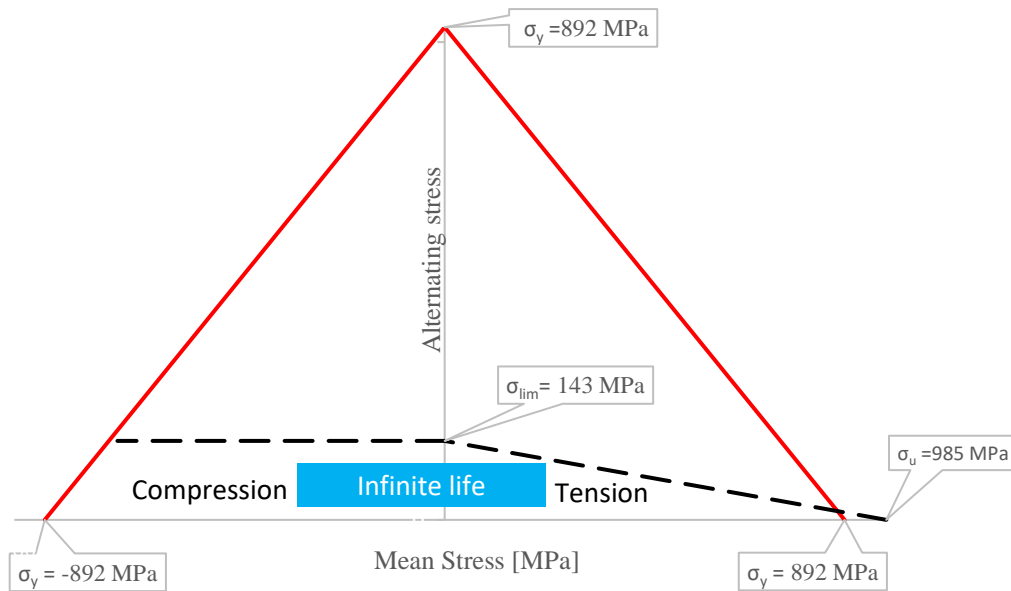


Figure 3.37. As-built specimens - Goodman-Haigh diagram.

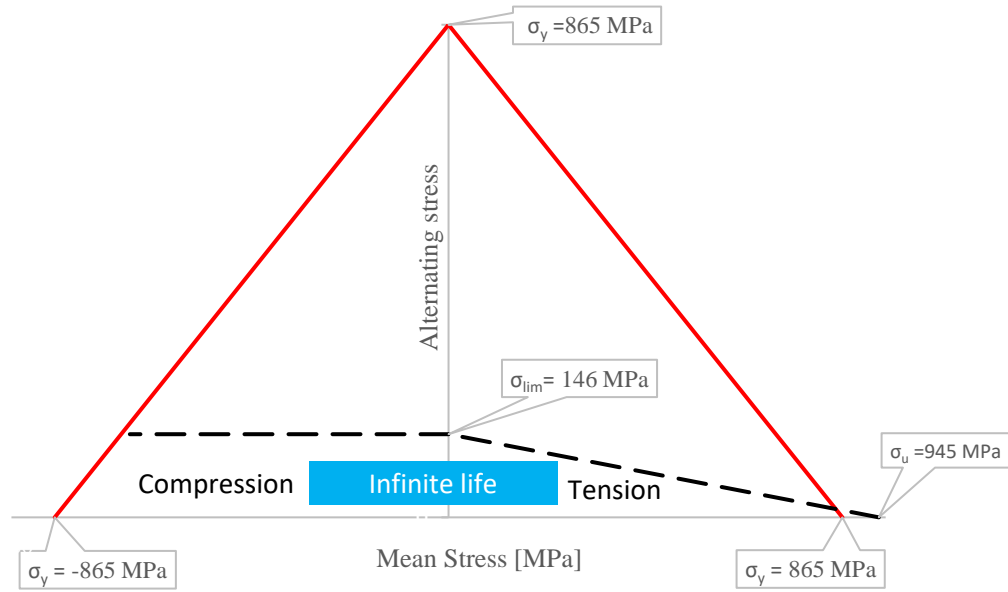


Figure 3.38. HIP post-treated specimens - Goodman-Haigh diagram.

So far, p -index and M constant values have been calculated using four samples for as-built and HIP samples and each build direction. Then, the consistency of equation 3.5 is tested by using a fifth stress level as it is possible in as-built specimens. After demonstrating the applicability of the equation for as-built additively manufactured samples, it is evaluated that it will also be used for HIP samples. Finally, since there are already as-built specimens produced, one, fatigue tests are repeated only for as-built conditions. This second as-built specimen batch is manufactured in a different production volume while different operators perform surface machining with different machines. In this way, it is aimed to see how effective the production volume and surface machining are. Second tests were conducted well after the first test campaign. In this way, the consistency of the tests is checked. As shown in Figure 3.39, no significant difference is observed between the fatigue tests performed early and later. The p -index and M constant values are also close for this test campaign. This result shows that manufacturing and machining do not affect the IQF method; with this assumption, it is concluded that the IQF method would also be used for HIP samples.

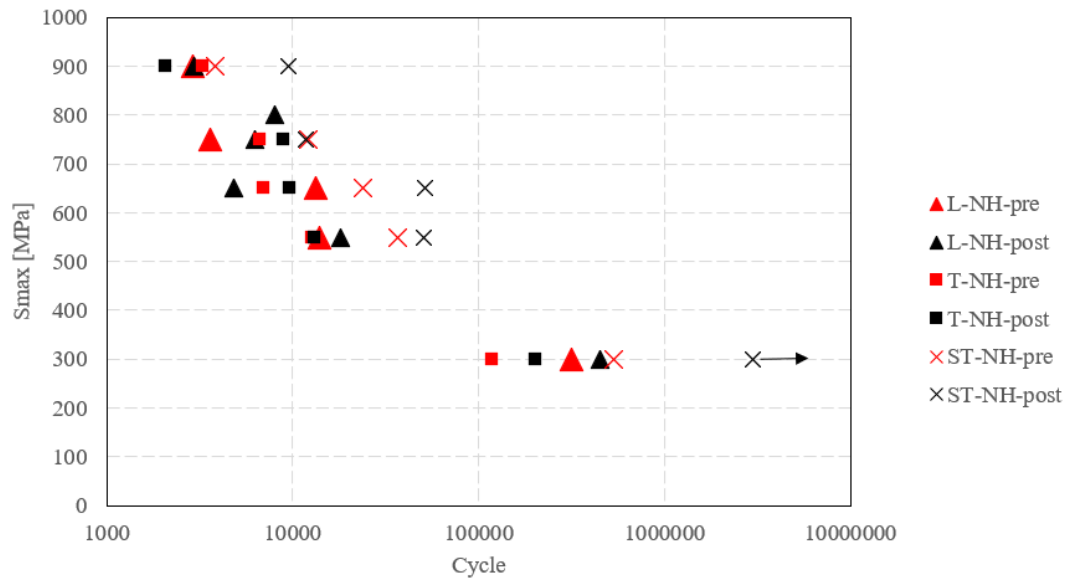


Figure 3.39. As-built-specimens pre and post-test comparison.

In conclusion, the monotonic uniaxial loaded fatigue test campaign of test specimens manufactured by EBM for as-built and HIP post-treated cases is presented. The effects of surface roughness are excluded from the results, and milled surface cases are presented. Furthermore, test results are modeled by the Airbus IQF method, and the model fits the results of the as-built case. Furthermore, it is assessed that manufacturing and surface machining has no effect in this test campaign. Only material properties are extracted by the IQF method; therefore, IQF will fit the HIP post-treated case. This modeling will allow future users to utilize it for monotonic and complex loading.

Moreover, the following findings are obtained from the fatigue test campaign:

- The p -index values of HIP post-treated specimens and as-built specimens are 5.5 and 4.5, respectively. It is smaller than the conventional Ti-6Al-4V; thus, the fatigue response of additively manufactured Ti-6Al-4V is worse than the conventional one.
- M material constant of additively manufactured specimens is well below the conventional alloy; therefore, fatigue properties are also observed well below the conventional alloy.

- As-built specimens seem to be better fatigue life behavior; however, after IQF calculations, fatigue life discrepancy is found insignificant.
- Short Transverse (ST) build direction gives comparably better fatigue life behavior.
- Derived Goodman-Haigh diagrams can be used for future safety factor calculations for fatigue analyses.
- Repeated tests on as-built test specimens showed the same fatigue life tendency compared to the first batch.

3.4 Pin-bearing testing campaign

An ideal airframe is a single unit made from a single material and manufactured from one piece. However, current airframes are built from numerous aluminum parts connected by joints. These joints consist of rivets, adhesives, bolts, screws, lugs, fittings, etc. [56]. Furthermore, many of these joints have holes for fasteners. Stress concentrations occur due to the cross-section reduction caused by these holes. While performing airframe stress analysis, these stresses need to be calculated analytically.

Joints are observed as the most common failure points from the experiences. Various factors can cause failures, but it is not easy to evaluate them. These factors affect static strength and stiffness, as well as fatigue life. Figure 3.40 shows the most common splice joint failure patterns [56].

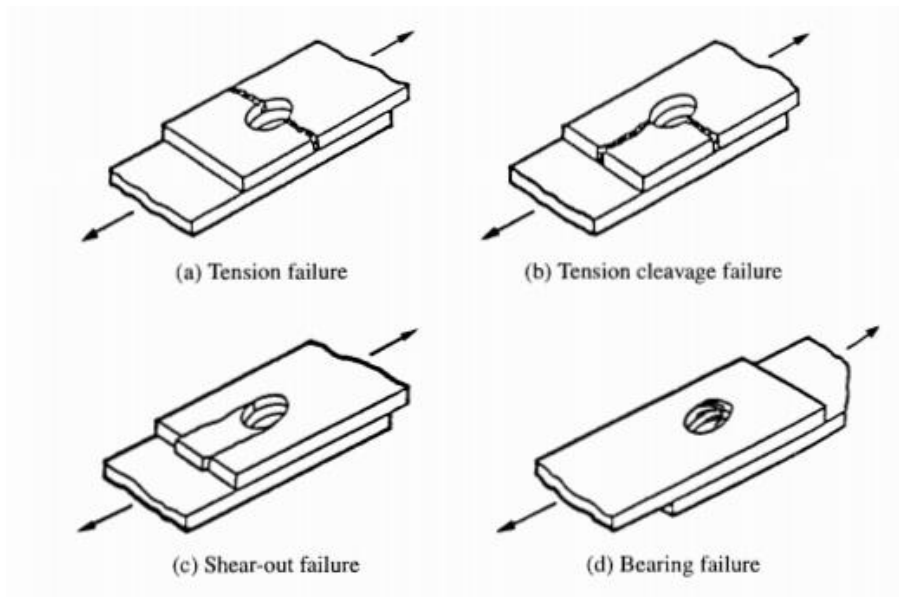


Figure 3.40. Typical failure modes of joints [56].

The bearing characteristics should be revealed since the parts produced by additive manufacturing will also use the same joint types. Bearing stress limits are the values used in joint and lug calculations with a mechanical fastener [47].

Bearing properties are of two types which are yield and ultimate bearing strengths. In order to determine these properties, test samples similar to the one in Figure 3.41 are used by utilizing the ASTM E238 standard [38]. In Figure 3.41, D represents the hole diameter, and e is the hole's distance to the edge in the direction of the applied load (F).

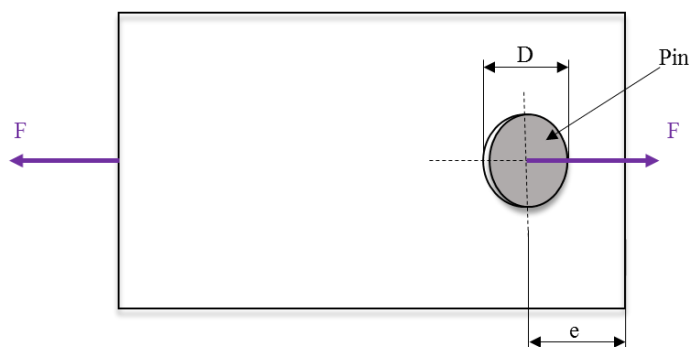


Figure 3.41. Dimensions for pin-bearing properties.

3.4.1 Pin-bearing test means and methods

Pin-bearing test specimen is manufactured in two different edge distances of the hole configuration. The pinhole diameter is selected as 6.35 mm. e/D ratios are taken as 1.5 and 2.0 and edge distances are the same as in MMPDS material properties tables. However, dimensions deviate from ASTM E238 standard due to additive manufacturing constraints of ST building direction. Pin bearing test specimen is shown in Figure 3.42. The thickness value is reduced by approximately 0.7 mm due to surface machining.

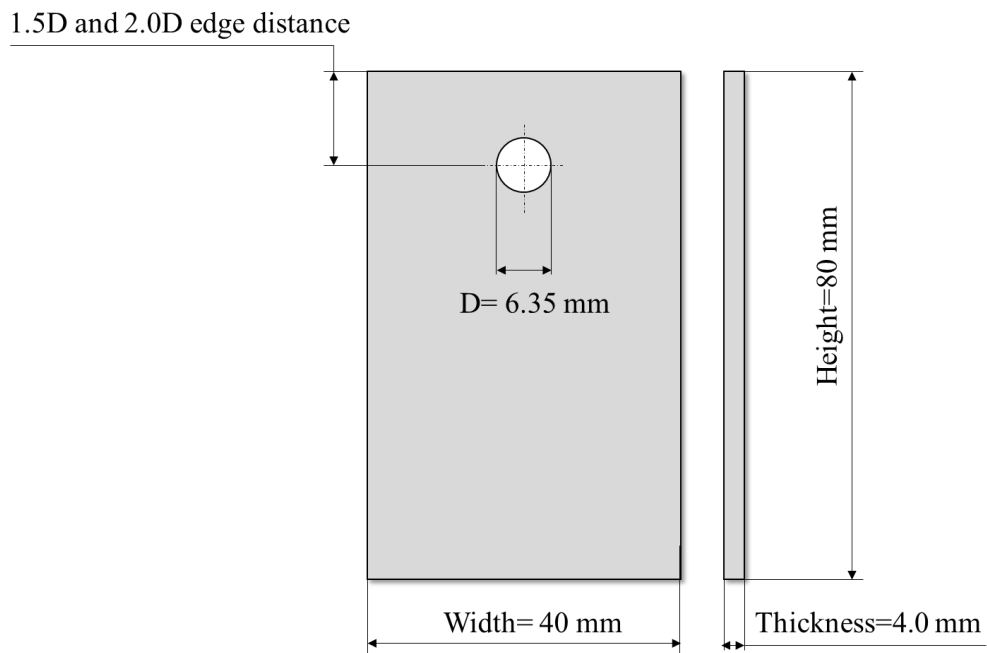


Figure 3.42. Pin bearing specimen.

A steel clevis is designed to perform the pin-bearing test. How the test specimen is attached to the clevis is shown in Figure 3.43. EN6115L4 standard bolt from the conventional Inconel material is chosen to serve as a pin. Later, this configuration is subjected to tension in the MTS device, where the tensile and fatigue tests are carried out, and the force-displacement values are recorded.

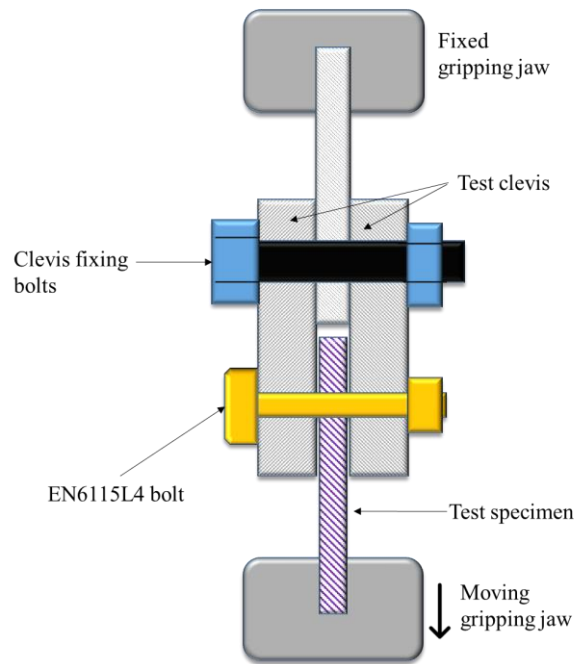


Figure 3.43. Pin bearing test schematic with tensile test machine.

The test configuration is also shown in Figure 3.44. A DIC capture is done only for the first specimen; bolt displacement calibration is done according to machine displacement values.

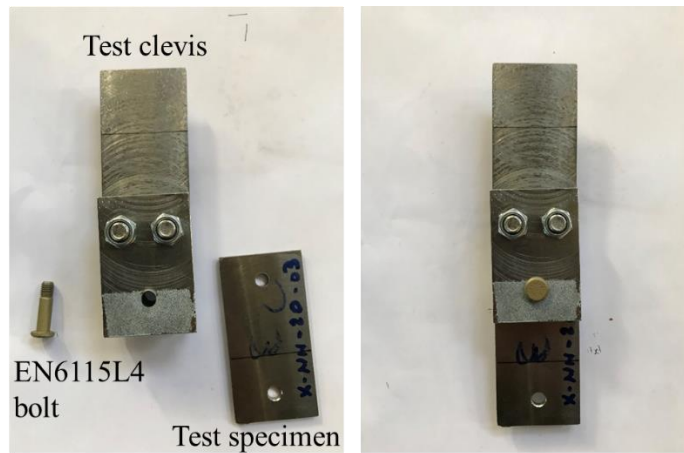


Figure 3.44. Pin bearing test configuration.

After DIC capture, an extensometer is placed from the bolt center and close to the gripping jaw. Instead of strain value, displacement is calculated from the image. The displacement calibration extensometer is shown in Figure 3.45.

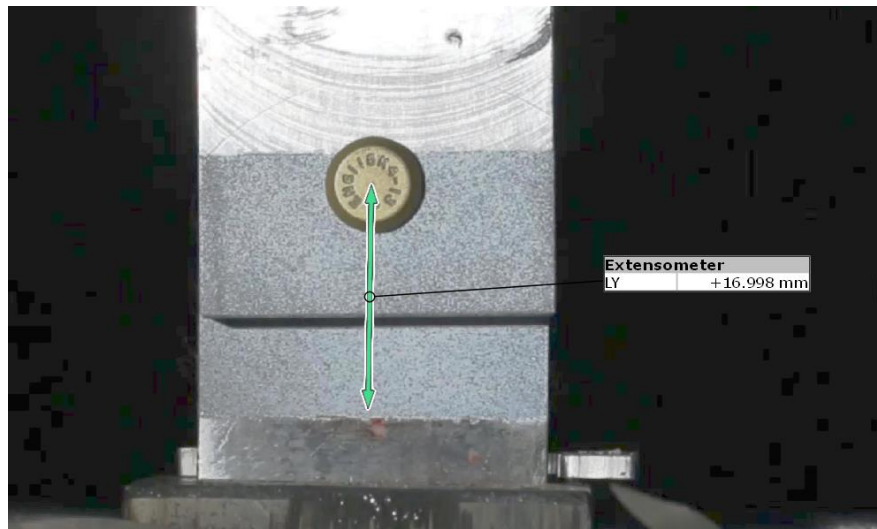


Figure 3.45. Pin bearing test displacement calibration by DIC.

Due to fixing bolts and testing clevis flexibility, characteristic pin displacement is different from machine displacement. Displacement conversion is done according to the chart in Figure 3.46.

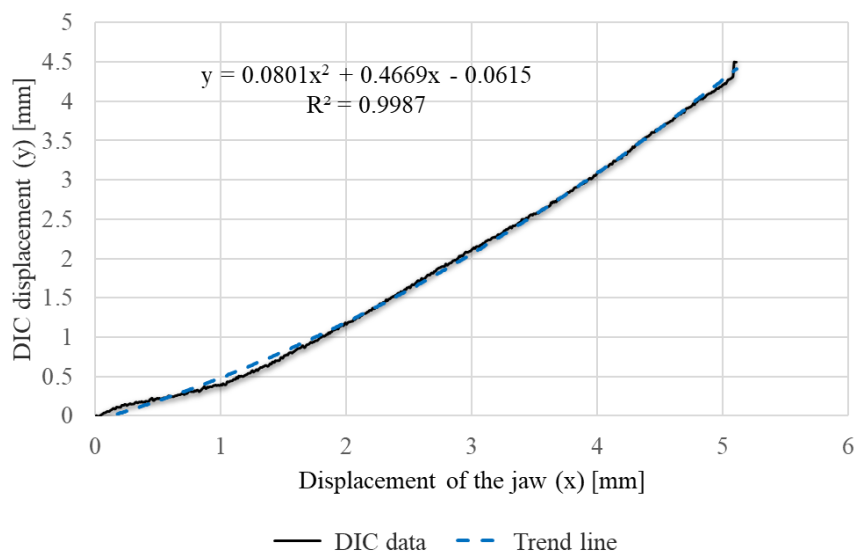


Figure 3.46. Calibration data

Finally, stress is calculated by dividing the applied force to the cross-section area obtained by multiplying the thickness of the specimen and the hole diameter. MMPDS recommends maximum stress value as ultimate bearing strength. Therefore, maximum stress values are extracted for ultimate bearing strength from test results. Furthermore, yield strength is not easy to extract from the results. Although EN6115L4 strong titanium bolts are used, these bolts also deform during the tests at the first step. Then EN6115L4 Inconel bolts are used as a pin. Test result graphs also include bolt deflection, and it is not easy to distinguish it. MMPDS recommends a parallel line shifted 0.02 times pin diameter with elastic region slope to calculate tensile strength. Figure 3.47 explains how yield and ultimate bearing strengths are extracted on a sample test data visually. It gives consistent results for 1.5D edge distance specimens; however, it does not work for 2D edge distance specimens. Figure 3.48 shows the deformation of the specimen and the bolt with a 2D edge distance, and this figure gives clues about the difficulty of obtaining tensile strength data.

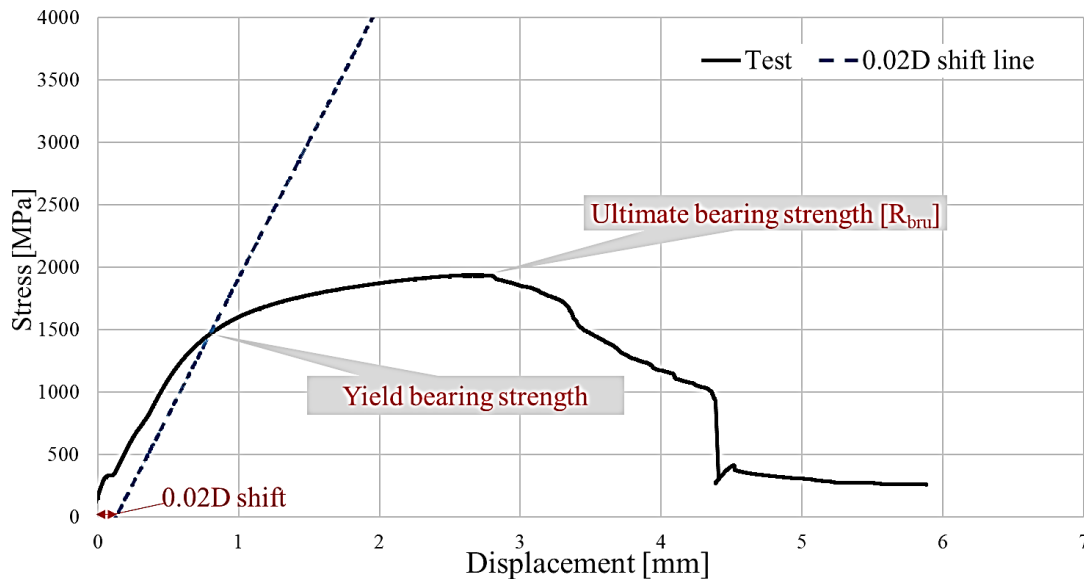


Figure 3.47. Extraction of yield and ultimate bearing strengths from a sample test data.



Figure 3.48. First pin-bearing specimen and deformed bolt after failure.

3.4.1 Results of pin-bearing test campaign

A total of 30 specimens are tested. The strengths of the two specimens cannot be measured due to bolt shear failure. Maximum three specimens are tested per edge distance in a build direction group and then standard deviation calculation is excluded in these results. No statistical comparison is made since there will not be a reliable comparison considering that there is one datum in these data sets. The summary of results given in Table 3.8 represents averaged values of each build direction and AMS4911 pin-bearing strength from MMPDS [47]. There is a slight difference between the build direction and the conventional bearing strength values. Moreover, the yield strength of $e/D=2.0$ specimens cannot be adequately calculated due to bolt deflection; however, it can be assumed equal to conventional bearing yield strength from ultimate bearing strength results. The yield bearing strength data given for $e/D=2.0$ in Table 3.8 are not reliable, they are given for informational purposes only.

Table 3.8 Averaged summary pin bearing results according to build direction and edge distance and comparison of AMS4911.

| | As-built | | | HIP | | | AMS4911 |
|-----------------|----------|--------|---------|--------|--------|---------|---------|
| | L-1.5D | T-1.5D | ST-1.5D | L-1.5D | T-1.5D | ST-1.5D | 1.5D |
| R_{bru} [MPa] | 1417 | 1522 | 1490 | 1307 | 1504 | 1421 | 1469 |
| R_{bry} [MPa] | 1319 | 1267 | 1330 | 1270 | 1421 | 1334 | 1179 |
| | L-2D | T-2D | ST-2D | L-2D | T-2D | ST-2D | 2D |
| R_{bru} [MPa] | 1882 | 1925 | 1935 | 1880 | 1875 | 1850 | 1875 |
| R_{bry} [MPa] | 1280 | 1158 | 1441 | 1123 | 1053 | 1527 | 1434 |

In Figure 3.49, ultimate and yield strength comparisons of $e/D=1.5$ specimens are carried out. According to these results, ultimate strength is almost equal to AMS4911 bearing strength. However, the yield strength of additively manufactured samples is higher than AMS4911 and shows a behavior close to the ultimate bearing strength except for the as-built T-1.5D case. This result is due to the brittle response of the additively manufactured samples. Similar brittle behavior can be seen in Table 3.4 since the elongation values are lower than that of the conventional alloy. Besides, it should be noted that the necking phenomenon, which is more prominent in ductile materials, is not seen in these samples produced by additive manufacturing, see the tensile test sample pictures given in Appendix A. In addition, samples produced in both as-built and HIP longitudinal build directions have a significantly lower pin-bearing strength tendency than in other build directions. Furthermore, no significant effect of the HIP process is observed in the additively manufactured samples.

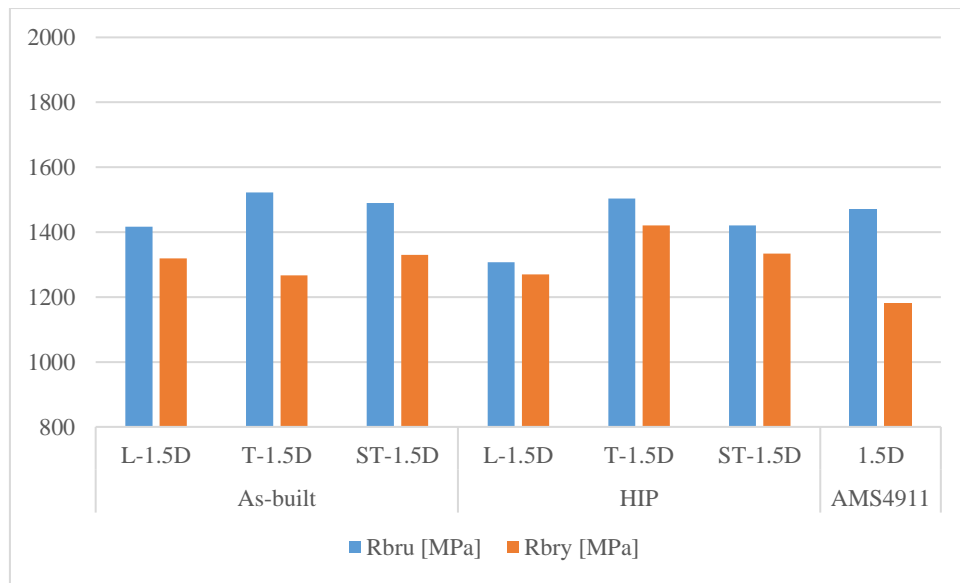


Figure 3.49. $e/D=1.5$ Ultimate and yield pin-bearing strength comparison.

In $e/D=2.0$ samples, the bearing yield strengths cannot be calculated correctly due to the deflection of the bolt. However, the ultimate strength values are close to the conventional AM4911 sample, as shown in Figure 3.50. No significant effect of HIP and build direction is observed in these samples.

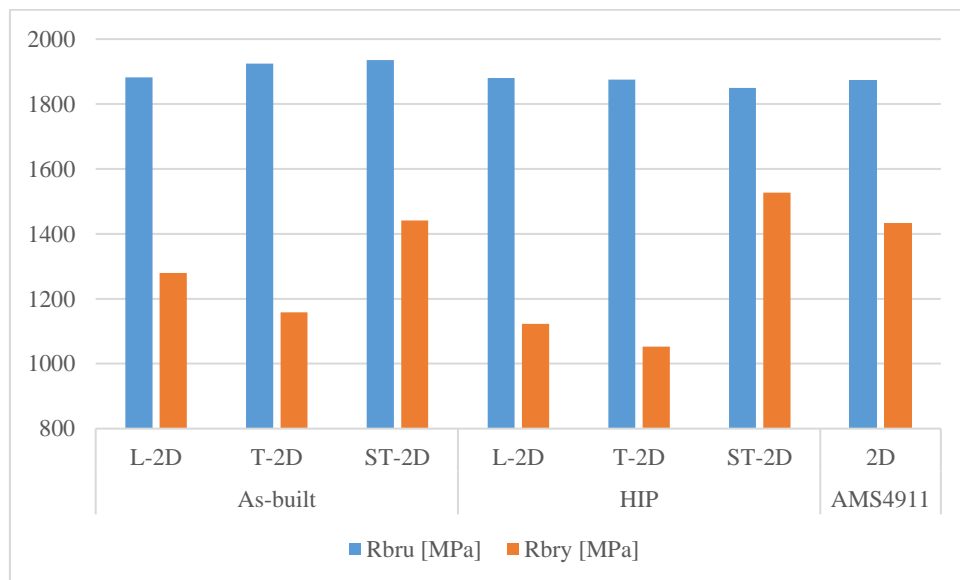


Figure 3.50. $e/D=2.0$ Ultimate and yield pin-bearing strength comparison.

Photographs of the specimens used for the pin-bearing tests, taken after fracture, are given in Appendix D and test results for each specimen are also presented. As can be seen in the photos, shear-out failure is dominant among the failure modes given in Figure 3.40 for as-built samples. On the other hand, tension cleavage failure mode is more common in L build direction of as-built samples. Moreover, HIP post-processed test specimens often show tension cleavage failure modes resulting from more ductile behavior.

In conclusion, 30 pin-bearing test specimens with 6.35 mm hole diameter, $e/D=1.5$, and $e/D=2.0$ edge distance are tested by a custom design fixing apparatus on an MTS tensile test machine.

The following findings can be listed as outcomes of the pin-bearing test campaign:

- The ultimate pin-bearing strength of all additively manufactured specimens is obtained close to the conventional AMS4911 pin-bearing ultimate strength.
- The yield strength of $e/D=1.5$ can be successfully determined. Additively manufactured specimens have higher pin-bearing strength than AMS 4911 and, the yield strengths are close to their ultimate strength due to fragile behavior.
- The yield strength of $e/D=2.0$ specimens cannot be extracted due to excessive bolt bending.
- No significant effect of HIP post-treatment and build direction on pin-bearing strength is observed from test results.
- The dominant failure mode in most as-built specimens is the shear-out mode. However, tension cleavage is more commonly observed in HIP post-treated samples.
- As seen from the photos of the pin-bearing samples in Appendix D, shear out failure mode is dominant in as-built specimens. However, tension cleavage failure mode is also detected in two $e/D=2.0$ and one $e/D=1.5$ longitudinal build direction.

- In specimens with HIP, tension cleavage and bearing failure modes are dominant in $e/D=2.0$ samples, whereas tension cleavage and shear out modes are significant in samples of $e/D=1.5$.

CHAPTER 4

A CASE STUDY TO LIGHTEN AN UNMANNED AERIAL VEHICLE PYLON FITTING BY TOPOLOGY OPTIMIZATION AND ELECTRON BEAM MELTING

4.1 Introduction

Structural optimization is gaining significant importance in the automotive and aerospace industries. Optimization methods have been used to reduce costs for years in the automotive industry. On the other hand, in the aerospace industry, compliance with airworthiness requirements and weight come before the cost. Especially in space structures, weight reduction significantly contributes to the spacecraft's successful mission and its extended life. At this point, structural optimization tools are beneficial for design engineers. This study it is aimed to lighten a pylon fitting of an unmanned aerial vehicle (UAV) by using the topology optimization method.

The operating altitude of unmanned aerial vehicles can be affected by many parameters. Weight reduction of the structural parts to achieve the target altitude is one of the design efforts and can be achieved by converting primary and secondary structures from metallic to carbon composite material. Furthermore, some secondary structures, such as fittings, must be produced metallic and usually made of aluminum alloys. In addition to the weight disadvantage, aluminum alloys have galvanic incompatibility with carbon composite materials. At this point, additive manufacturing methods offer solutions with a combination of topology optimization. Additive manufacturing methods can easily manufacture complex geometries obtained from topology optimization during weight reduction campaigns of unmanned aerial vehicles such as fittings. Goh et al. [32] state that according to the Breguet method, aerodynamic parameters must be maximized, and weight must be minimized for longer endurance of fixed-wing unmanned aerial vehicles (UAV).

However, complex inner structures cannot be manufactured by conventional methods. Additive manufacturing brings a new challenge for UAVs in the manner of shape and inner structure. The introduction of additive manufacturing has not just revolutionized the field of UAVs but has impacted the entire manufacturing arena by simplifying the design and easing the fabrication process [32].

In this chapter, a UAV pylon fitting weight reduction campaign will be performed by topology optimization using Hypermesh and Optistruct commercial software through Altair® HyperWorks® Version 2019 [57]. Then, the fitting lightened by optimization will be produced by Electron Beam Melting (EBM) additive manufacturing method. Moreover, verification and validation of the manufactured fitting with static, dynamic, and fatigue analyses are also explained. Here, the material properties obtained in Chapter 3 are used instead of the standard Ti-6Al-4V properties, unlike other studies in the literature. Finally, a static test setup for qualification is designed, and the manufactured fitting is qualified with this test setup which could also be used for qualification purposes during mass production.

4.2 Topology optimization of the unmanned aerial vehicle pylon fitting

The payload carrying UAV has four payloads, having two on each wing. The most loaded one is selected, and three different worst-case load cases are applied among all fittings and load cases. Load cases are divided into launch, flight, and landing groups. Choosing the most challenging loads in each group aims to design and manufacture a light fitting that will withstand these loads. UAV and pylons for payload connections are shown schematically in Figure 4.1.

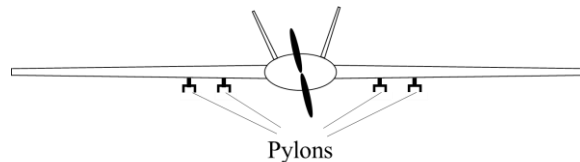


Figure 4.1. Schematic view of UAV and pylons which hold the payloads (not scaled).

Each pylon is connected to the wing structure with forward and rear fittings, and one of these fittings is chosen for the weight reduction campaign. The fitting is shown in Figure 4.2, and the overall weight reduction campaign is summarized in Figure 4.3 as a flowchart.

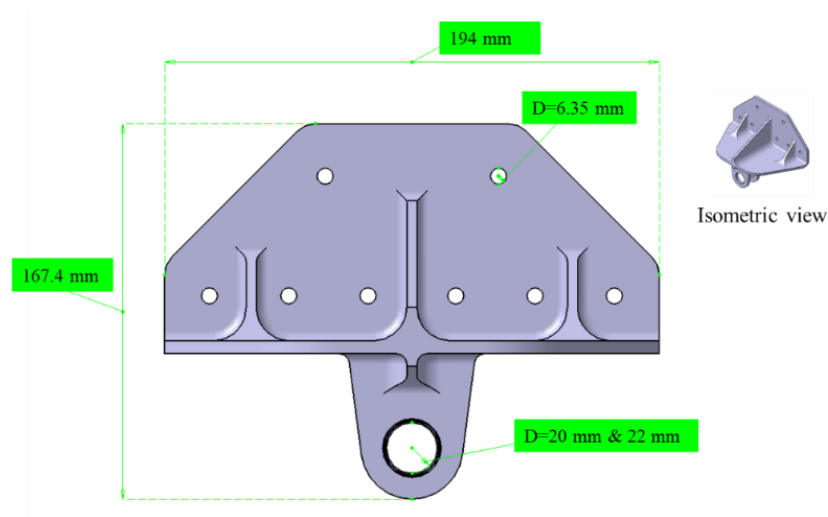


Figure 4.2. Front and isometric view of pylon fitting to be optimized.

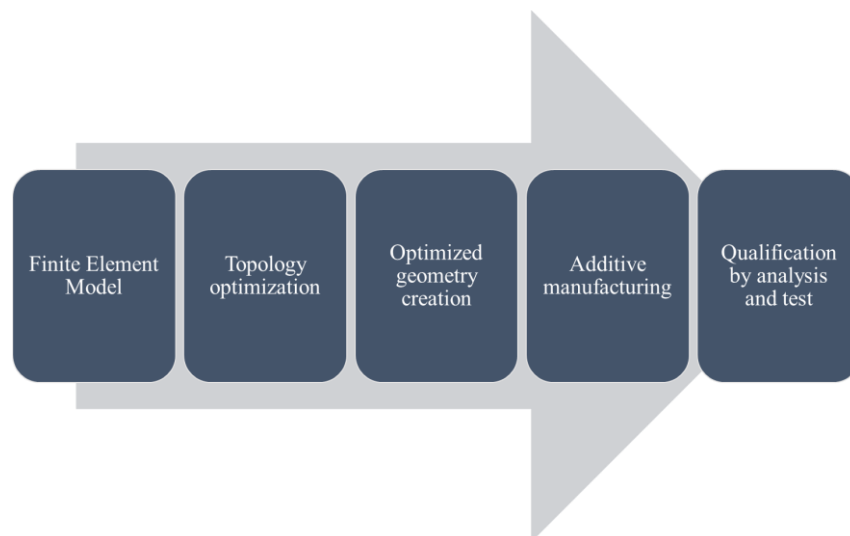


Figure 4.3. Generic process flow of weight reduction campaign.

4.2.1 Finite element modeling of the fitting

The first step of the fitting weight reduction campaign is creating an accurate Finite Element Model (FEM). This model is established according to the flowchart given in Figure 4.4. This campaign uses a solid model for meshing, material properties assignment, and boundary conditions generation. The worst three load cases are applied to the model, and the model is run for quasi-static analysis.

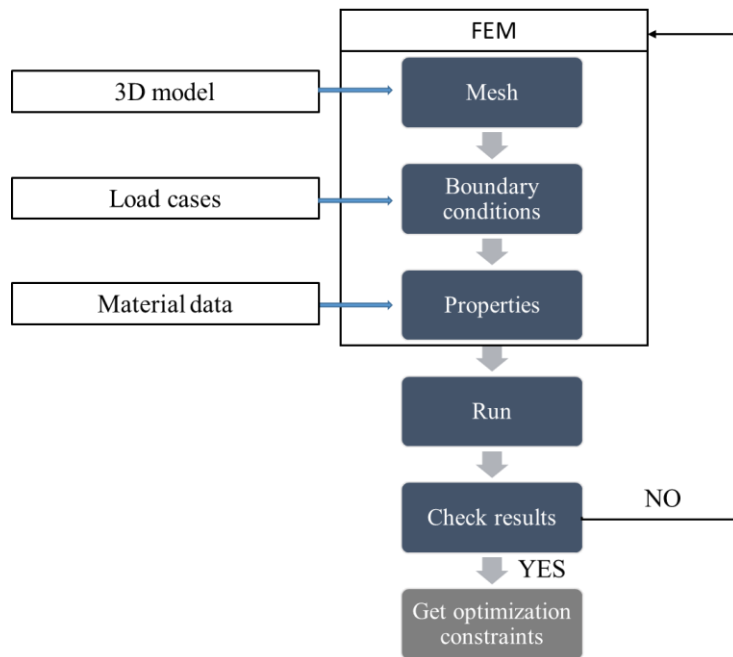


Figure 4.4. Process flowchart for FEM creation.

The fitting material is an aluminum alloy, and the material specifications are taken from the Metallic Material Properties Development and Standardization (MMPDS) Handbook. Rice et al. [47] state that the MMPDS Handbook is recognized internationally as a reliable source of aircraft materials data for aerospace materials selection and analysis.

The fitting installation model is presented schematically in Figure 4.5. The opposite part of the fitting is taken as symmetrical. Placing a fitting on the opposite side aims to model flexibility as loads are applied to the center of gravity of the whole system.

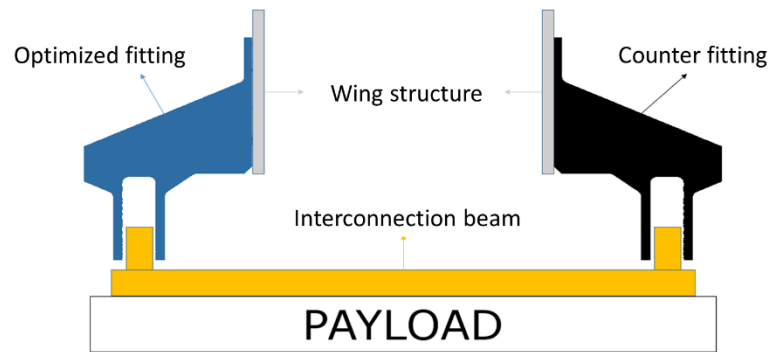


Figure 4.5. Generic presentation of the simulation.

Loads are evaluated from the global FEM as they expose the center of gravity (CoG) of the interconnection beam and payload. The generic view of the model is shown in Figure 4.6. Applied forces and moments to the CoGs in 6 degrees of freedom (DOF) are also visualized in the figure.

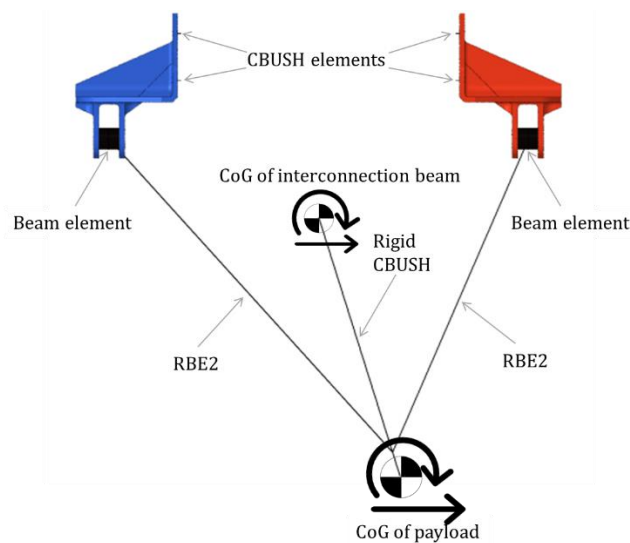


Figure 4.6. FEM of the fitting.

The interconnection beam of each endpoint attachment to the clevis is modeled by a cylindrical steel beam element that fits the lug shown in Figure 4.7. This beam element is attached to the inner surface of the lug by rigid RBE2 elements.

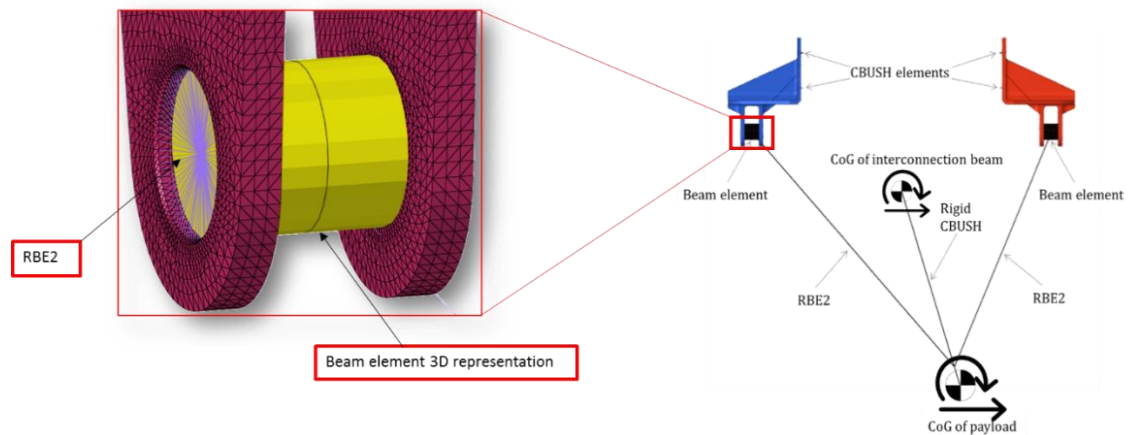


Figure 4.7. Clevis pin modeling as steel beam element.

The fitting is connected to the wing structural walls using bolts. It is necessary to give flexibility to the fasteners for a realistic model. This flexibility of the fasteners can be achieved with CBUSH elements. Figure 4.8 shows sample CBUSH elements representing bolt fasteners.

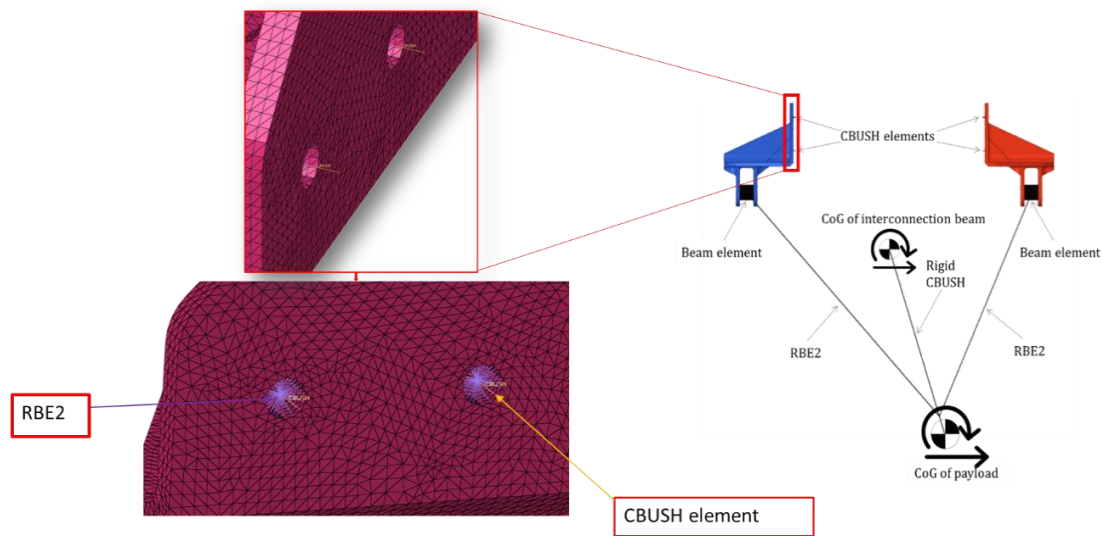


Figure 4.8 Fastener modeling as CBUSH.

CBUSH defines a generalized spring-damper structural element for 6 DOF. Six stiffness values depicted in Figure 4.9 for CBUSH elements must be specified. The Huth method determines the shear stiffness [58], whereas a bar element in axial loading calculates the axial stiffness.

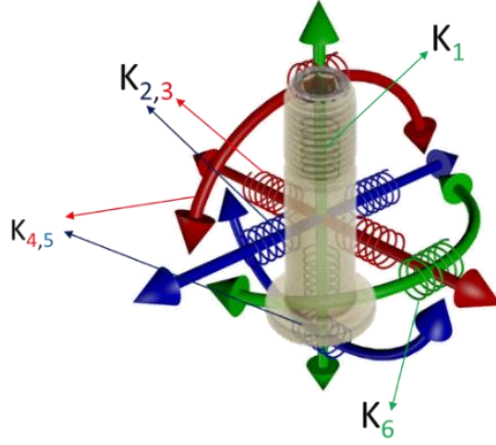


Figure 4.9. CBUSH element spring constants representation for a fastener.

Shear stiffness calculation by the Huth method is carried out according to equation 4.1 and axial stiffness is calculated according to equation 4.2

$$\frac{1}{k_{fast,shear}^{FEM}} = \left(\frac{t_A + t_B}{2 \cdot \emptyset} \right)^a \left(\frac{b_A}{t_A E_A} + \frac{b_B}{t_B E_B} + \frac{b_A}{2 \cdot t_A \cdot E_{fast}} + \frac{b_B}{2 \cdot t_B \cdot E_{fast}} \right) \quad 4.1$$

$$\frac{1}{k_{fast,axial}^{FEM}} = \frac{E_{fast} \cdot \pi \cdot \emptyset^2}{4 \cdot L_{fast}} \quad 4.2$$

Bending stiffness values may be calculated according to equation 4.3 when the contact between the joints is not modeled; however, using 10^9 value is an accepted practical approach also.

$$\frac{1}{k_{fast,bending}^{FEM}} = 100 \cdot \left(\text{Max}(k_{fast,shear}^{FEM}) \cdot \frac{L_{fast}^2}{4} \right) \quad 4.3$$

where; t_A and t_B denotes the thickness of parts A and B, E_A and E_B modulus of parts A and B, \emptyset fastener diameter, E_{fast} modulus of the fastener, $a = \frac{2}{3}$ for bolt and $a = \frac{2}{5}$ for rivet, b_A , $b_B = 3.0$ for metal and 4.2 for carbon material. Rotational fastening stiffness in the direction of the fastening axis is taken as 100 N/rad. Stiffness values

for aluminum fitting and Ti-6Al-4V fitting mounted on aluminum wing structures are listed in Table 4.1.

Spring coefficients are updated accordingly when titanium is used during the optimization and re-analyses phase.

Table 4.1 CBUSH element stiffness values

| Stiffness components | Aluminum-Aluminum | Ti6Al4V-Aluminum |
|--------------------------------------|-------------------|------------------|
| Axial stiffness, K_1 [N/mm] | 407377 | 931205 |
| Shear stiffness, $K_{2,3}$ [N/mm] | 30583 | 43673 |
| Bending stiffness, $K_{4,5}$ [N/rad] | 1×10^9 | 1×10^9 |
| Rotational stiffness, K_6 [N/rad] | 100 | 100 |

The fittings are meshed with CTETRA solid elements. Mesh dependency is checked by running FEM analysis with three different mesh densities. The FE model with 266050 CTETRA elements is selected for optimization based on the results from these FEM analysis presented in Appendix E.

4.2.2 Topology optimization of the fitting

There are different approaches to structural optimization. These can be classified as; size, shape, and topology optimization [59]. Size optimization is essential for structural optimization. Shape optimization, on the other hand, aims to find the optimal shape where the variable becomes the shape of the domain. It is necessary to determine the optimum one from the previously determined shapes. Topology optimization is a method to define optimum material distribution with the assumption of elastic isotropic material, and it aims to devise the optimum material layout within a borderline [8]. Known quantities in this optimization are only load, support structure application region, final volume, and other constraints such as

displacement, stresses, strains, natural frequencies, etc. In this particular problem, the physical size and shape are unknown. Figure 4.10 summarizes the different types of structural optimizations via simplified presentations.

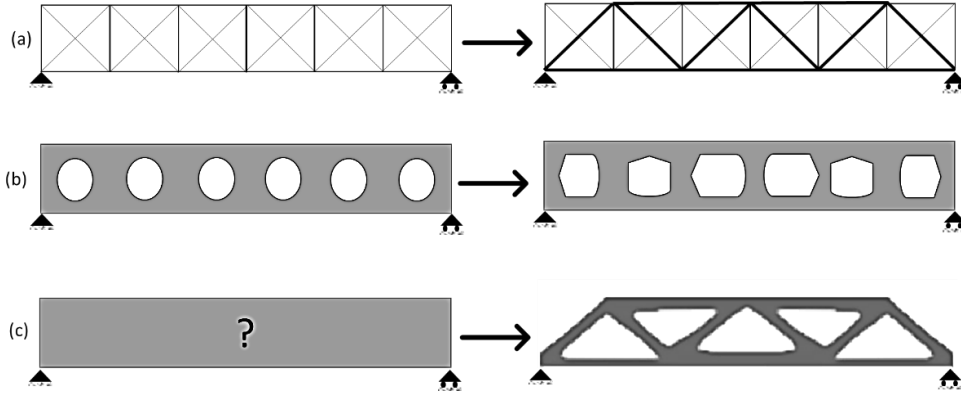


Figure 4.10. Structural optimization categories. a) sizing optimization of a truss structure b) shape optimization c) topology optimization [59].

This study will use a gradient-based topology optimization having the density method. Gradient-based topology optimization problems with the density method are based on finite element analysis, and the stiffness of these elements in the finite element model is penalized by a factor m with three different approaches as in equation 4.4 by assuming each element is quasi-porous with an artificial density ρ ranging from 0 to 1. In this study, Solid Isotropic Material with penalization (SIMP) formulation is preferred, which is used by the vast majority, and it does not sacrifice the performance of the optimized part. The density value of zero means no material, and the value of one means solid material. Intermediate densities result in a penalized stiffness value. Here, solid elements are assumed to have isotropic material behavior. $\tilde{\mathbf{K}}$ is the stiffness matrix searched in the topology optimization problem, and \mathbf{K} is the stiffness matrix of the solid element. Since the established problem results in a 0-1 problem, discrete stiffness values are distributed over the material domain. This approach requires iterations, and the most optimum material distribution is made according to the constraints and the objective function.

| | | |
|------------|--|-----|
| SIMP | $\tilde{K}(\rho) = \rho^m K$ | |
| RAMP | $\tilde{K}(\rho) = \left(\frac{\rho}{1 + m(1 - \rho)} \right) K$ | 4.4 |
| Polynomial | $\tilde{K}(\rho) = \left(\left(\frac{a-1}{a} \right) \rho^m + \left(\frac{1}{a} \right) \rho \right) K$ | |

In equation 4.4, a denotes the order of the polynomial.

In order to build up a topology optimization sequence in practice, first of all, a suitable domain must be chosen. Then, non-design material regions should be applied, if applicable. Under these circumstances, FEM must be created with fine enough element sizes. After creating the optimization model, a homogenous material distribution is first applied, and then FEM calculations are performed. After checking compliance with the objective function, density values are recalculated and assigned to materials. This process continues iteratively up to the optimization constraints, and objectives are satisfied. Here, low pass filtering is also utilized for sensitivity filtering, where element sensitivities are calculated and addressed to elements by weighing neighboring sensitivities. The overall topology optimization calculations and material distribution can be summarized in the flow chart presented in Figure 4.11.

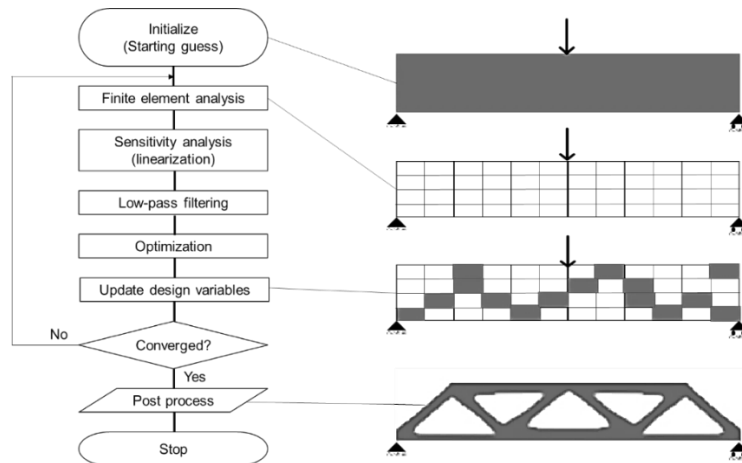


Figure 4.11. The topology optimization computation flow [59].

While carrying out topology optimization in commercial software, the manufacturing method can also be selected as a parameter. The overhang angle

(OHA) parameter emerges as a manufacturing method parameter in additive manufacturing. In order to explain the OHA requirement, some temporary support structures may be needed to prevent material warping or disintegration in additive manufacturing [60]. Depending on the geometry, these support structures are used in regions that cannot self-support. The ability to support itself comes from a certain angle. This angle is called the overhang angle (OHA). Powder bed selective laser melting machines mostly have 45° OHA; however, the OHA for Arcam Q20 Plus EBM machine used in this research is 60°. Figure 4.12 depicts OHA region samples depending on the geometry. OHA is not only the constraint for material integrity as thermal distortions are also prevented by providing sufficient heat transfer through the support structures [61].

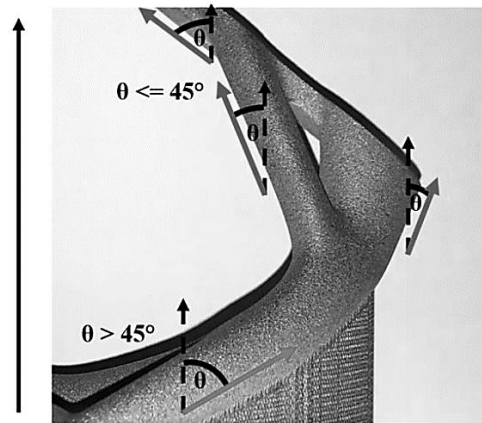


Figure 4.12. An example of an additive-manufactured part with build direction indicated with the black arrow, showing self-supporting build angles in green, and areas overhanging greater than 45° requiring support structure in red [61].

Some commercial topology optimization software also includes this overhang constraint in their algorithms. Altair OptiStruct® V2019 [57], a solver, used for this case study, can constrain the OHA depending on the additive manufacturing method used for the optimization problem. While defining the build direction and OHA for this solver, the direction should be defined with two nodes, as shown in Figure 4.13. The angle should be entered according to the aforementioned figure. Here, the acronym GID (Grid Identifier) is used for node identification.

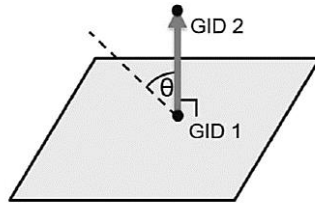


Figure 4.13. Definition of the build direction vector and OHA definition [61].

Figure 4.14 depicts the results of a topology optimization problem solved with two different OHA angles of 45° and 30° to observe the effect of different angles. Here, the effect of the OHA is clearly evident [61].

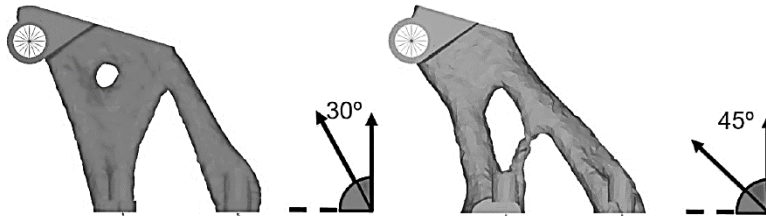


Figure 4.14. Example of the results obtained by varying the allowable OHA parameter [61].

Returning back to the topology optimization problem in this case study, the previously created FEM is used for topology optimization of the pylon fitting. The material is aluminum alloy in the original fitting model, but since the final fitting will be manufactured by EBM, the material properties changed to Ti-6Al-4V alloy. The flowchart of the optimization process is summarized in Figure 4.15. The optimization process of the weight reduction campaign is performed according to this flow.

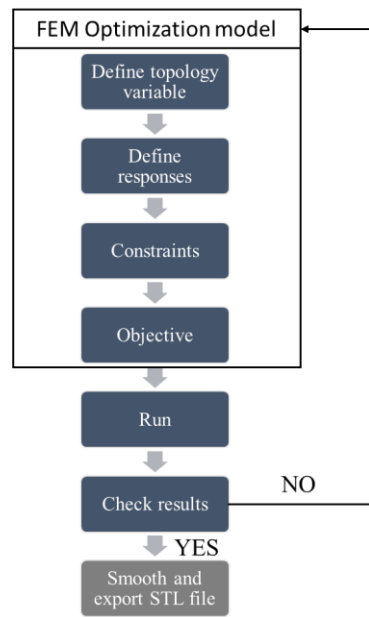


Figure 4.15. Process flowchart for topology optimization.

On the other hand, some non-design regions must be assigned. In this problem, non-design regions are shown in yellow in Figure 4.16. Besides, properties such as symmetry plane, additive manufacturing build direction, and overhang angle value can be specified when defining the topology variables at the first step.

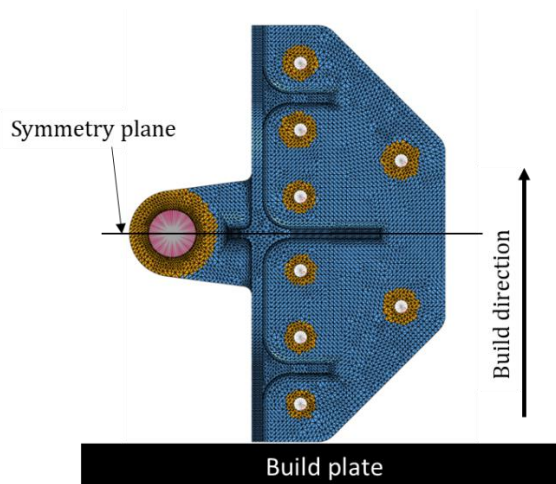


Figure 4.16. Optimization model including build direction.

The OHA, build direction, and penalty scheme are set by the window shown in Figure 4.17, specific to the additive manufacturing method. The symmetry plane and build direction are also entered as a part of the topology variable, in line with Figure 4.16.

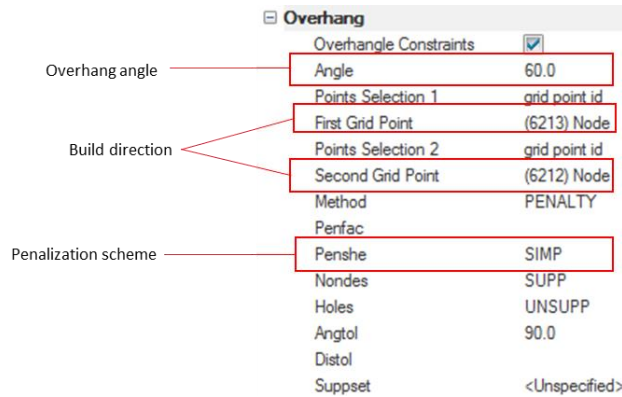


Figure 4.17. Additive manufacturing properties defined at the topology variable.

This optimization model's primary constraint is the lug tip's displacement. Other constraints are Von Mises, max, and min principal stresses, which are crucial in fitting strength analysis. The stress values obtained from the FEM of the original fitting are used for the determination of stress constraint levels. In Ti-6Al-4V alloy, since the modulus of elasticity value is higher than aluminum alloy, more stress is expected at the same displacement. Therefore, the stress constraints have been increased to match the ratios of the yield strengths, while the displacement constraint is the same as the original fitting. These determined constraint values are summarized in Table 4.2. The objective function is chosen as minimizing the volumetric fraction (vfrac); then, this will provide implicit weight reduction even if the density value is not entered.

Table 4.2 Optimization constraints.

| Constraint | Lower bound | Upper bound |
|----------------------------|-------------|-------------|
| Lug tip displacement [mm] | -0.65 | 0.65 |
| Von Mises Stress [MPa] | - | 475 |
| Max Principal Stress [MPa] | - | 607 |
| Min Principal Stress [MPa] | -607 | - |

In the optimization model, element sizes are changed while keeping all parameters identical, and some trial analyses are performed for three different meshes. The element density distribution contour and the obtained geometries from these optimization analyses are given in Appendix F. After this trial runs, the convenient optimization model is preferred among three models, giving a result close to the desired 0.30 ν frac value. The objective and constraint convergence graphs obtained for the selected model are also presented in Appendix F. With regard to the solution parameter, the software takes the penalty factor $m=2$, as described in its user manual, since the optimization model is solid element weighted [57]. Besides, it is desired that the ideal solution consists of 0 and 1 element densities, but in reality, there are also elements with intermediate densities. Therefore, one of the performance indicators, discreteness, is also calculated. The discreteness value is calculated at the end of each iteration as the ratio of the volume of the elements with a density of 0.9 and above to the volume of all elements. Discreteness of 1 is expected for the ideal solution, but it is not possible; however, solutions with discreteness above 0.5 are acceptable. In the last iteration of this optimization, the discreteness value is calculated as 0.67.

Finally, the design obtained at the end of the optimization step does not have a smooth geometry, then it is smoothed and exported as an STL (Standard Triangle Language) file. This STL file is neither a surface nor a solid; it is a mesh of triangles. This mesh data needs to be converted to a solid model for further steps.

4.2.3 Optimized solid geometry creation

After exporting the STL file of the optimum design obtained after a few optimization loops, this data should be converted to a surface or a solid geometry. The converted geometry will then be used for re-analysis and, if deemed appropriate, be produced by additive manufacturing. These conversion and analysis steps are summarized in the flowchart in Figure 4.18. This flowchart is developed during this weight reduction campaign.

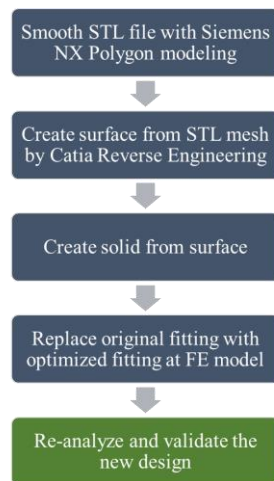


Figure 4.18. Process flowchart for optimized geometry creation.

Next, using Siemens NX polygon modeling, STL mesh data having a dispersed structure is smoothed. Then, the smoothed mesh data is transferred to the Catia V5 Reverse Engineering module as an STL file again, and the mesh data is converted to a surface and filled into a solid. Finally, this solid model is replaced with the fitting in the first FEM, and verification re-analysis is performed. Since the elements with intermediate density are also effective on the results during the optimization, re-analysis with a solid model is the most reliable method to verify the solution since the elements are at full density [57]. After last step of the optimization, obtained and verified final geometry will be lighter; however, it will have a complex shape.

4.2.4 Result of the topology optimization and finite element re-analysis

Constraint values are obtained by running the Finite Element Analysis (FEA) of the original aluminum fitting. The displacement data, which has the most decisive feature among these limit values, is shown in Figure 4.19. The clevis lug endpoint has the maximum displacement on the fitting and is displaced by 0.64 mm.

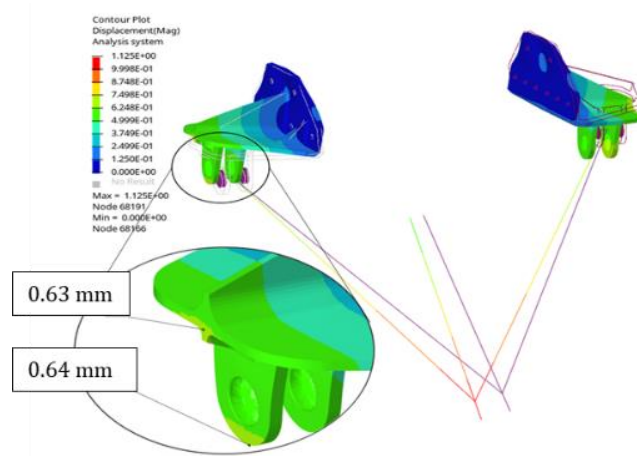


Figure 4.19. Displacement magnitude values distribution.

Values of Von Mises, maximum principal, and minimum principal stresses are retrieved after FEA and these values will then be used to determine the constraint values in the optimization step. Maximum Von Mises stress, maximum principal stress, and minimum principal stress are 278 MPa, 298 MPa, and -311 MPa, respectively. Figure 4.20 shows the locations and values.

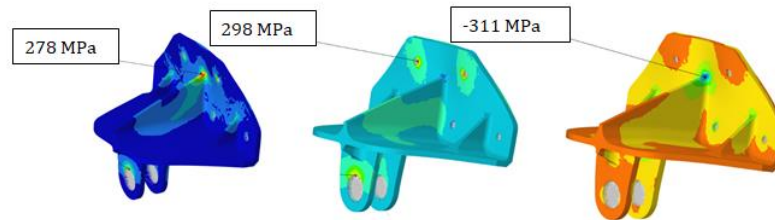


Figure 4.20. Von Mises, Max, and Min principal stresses, respectively.

While determining the displacement constraint in the topology optimization, a value close to the displacement value in the original fitting is selected. Excessive displacement of the fitting may damage the counter fitting and/or the aircraft airframe structural part. The optimization model is run several times for different options, including the build direction and symmetry plane options. Finally, the geometry is smoothed and exported as an STL file after deciding on the appropriate

optimal result. Figure 4.21 shows the exported STL mesh geometry. Unfortunately, it does not have the desired smoothness after the optimum result is smoothed and exported. Moreover, this design needs to be converted to solid geometry by further smoothing for subsequent use.



Figure 4.21. Smoothed and exported STL mesh data.

With the help of Siemens NX polygon modeling and Catia V5 Reverse Engineering, the geometry is further smoothed, and the final optimum design in Figure 4.22 is obtained. Holes and lugs are replaced from the original geometry for isoparametric design purposes. Although this design is made of the denser Ti-6Al-4V alloy, it is lighter than the original fitting with less density. The weight of the new design is 376 g, leading to a 31% weight reduction as the original aluminum fitting was 544 g.

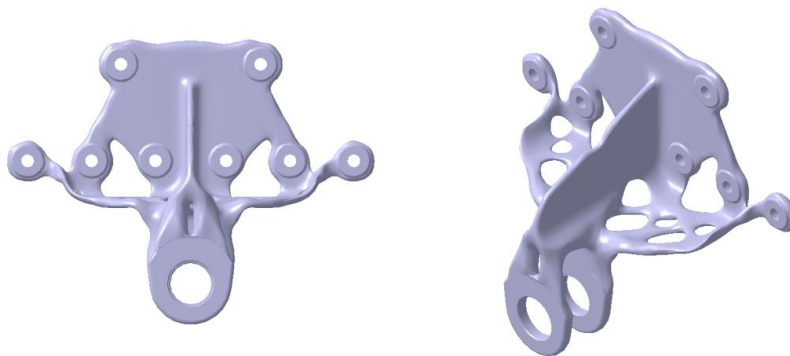


Figure 4.22. Optimized final solid geometry, front and isometric view.

After the desired solid model is obtained, the analysis is repeated by replacing the original fitting with the optimized fitting to repeat the FEA. As a result of the analysis, the displacement magnitude at the clevis lug endpoint shown in Figure 4.23 is obtained as 0.60 mm. This does not exceed the constraint determined as 0.65 mm.

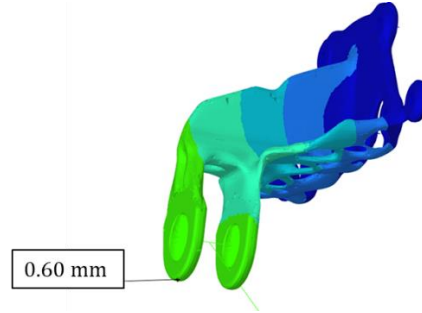


Figure 4.23. Displacement magnitude values distribution of optimized fitting.

Furthermore, the stress values are also taken from the points where the maximum stress values retrieved in the original fitting are read. Then these values are checked to see whether they exceed the constraint values or not. The original and optimized fitting FEA results are compared in Table 4.3. Reserve factor (RF) values, calculated by yield strength/actual stress, are also included in this table. According to these results, the optimized fitting is lighter and more reliable in quasi-static loads due to higher reserve factors.

Table 4.3 Comparison of FEA maximum values.

| | Original fitting (7050 Aluminum) | RF (yield) Yield/Actual | Optimized fitting (Ti-6Al-4V) | RF (yield) Yield/Actual |
|-----------------------------|-------------------------------------|----------------------------|----------------------------------|----------------------------|
| Modulus of Elasticity [GPa] | 71 | NA | 110 | NA |
| Max Displacement [mm] | 0.64 | NA | 0.60 | NA |
| Von Mises Stress | 278 [MPa] | 1.58 | 334 [MPa] | 2.60 |
| Max Principal Stress | 298 [MPa] | 1.48 | 345 [MPa] | 2.51 |
| Min Principal Stress | -311 [MPa] | 1.46 | -372 [MPa] | 2.47 |
| Weight [g] | 544 | NA | 376 | NA |

4.3 Validation of the optimized fitting

Following the FEA generation and topology optimization, the static and dynamic finite element analyses will be performed with tensile properties obtained in Section 3.2. Moreover, the pin-bearing calculations will also be performed with the properties obtained in Section 3.4.1. This section aims at a comparative validation of the original fitting with the optimized fitting. After validation, the fitting will be manufactured by EBM, and static qualification tests will be carried out.

4.3.1 Comparison of static finite element analysis results of original and optimized fitting

Prior to commencing the static analysis, the surface of the solid model is covered with a 0.001 mm thick shell element to read the stresses on the surface better by assuming this thickness does not affect the results significantly. The elements used here are also called “reading elements” and are used to capture the peak stresses on the free surfaces of the solid part by using shell elements with membrane properties [62]. After the original and optimized fitting are covered with the shell elements, analyses are performed, and comparisons are carried out. Modulus of elasticity and Poisson’s ratio for optimized fitting are taken for as-built properties from Table 3.4 as the modulus of elasticity is 116 GPa, and Poisson’s ratio is 0.30.

As mentioned before, the counter fitting or the primary structure to which the fittings are attached should not be damaged because of topology optimization. For this purpose, the opposite fitting is also examined by static finite element analysis.

Table 4.4 is created to summarize all static FEA trade-off studies. When the RF values in this table are checked, the optimized and counter fittings are more reliable than the original condition. Consequently, the optimized fitting can be manufactured and utilized on UAVs without HIP post-treatment if the design is evaluated in terms of the static case.

Table 4.4 Static FEA result comparison

| Optimized fitting | | Original fitting | RF (yield) Yield/Actual | Optimized fitting (No HIP) | RF (yield) Yield/Actual |
|-------------------|-----------------------------|----------------------|----------------------------|----------------------------------|----------------------------|
| | Modulus of Elasticity [GPa] | 71 | NA | 116 | NA |
| | Max Displacement [mm] | 0.64 | NA | 0.59 | NA |
| | Von Mises Stress | 278 MPa | 1.58 | 327 MPa | 2.89 |
| | Max Principal Stress | 298 MPa | 1.48 | 320 MPa | 2.95 |
| | Min Principal Stress | -317 MPa | 1.43 | -367 MPa | 2.57 |
| Counter fitting | | Pre- optimization | RF (yield) Yield/Actual | Post- optimization | RF (yield) Yield/Actual |
| | Modulus of Elasticity [GPa] | 71 | NA | 71 | NA |
| | Max Displacement [mm] | 0.66 | NA | 0.64 | NA |
| | Von Mises Stress | 343 MPa | 1.28 | 337 MPa | 1.30 |
| | Max Principal Stress | 391 MPa | 1.12 | 384 MPa | 1.15 |
| | Min Principal Stress | -138 MPa | 3.19 | -134 MPa | 3.28 |

4.3.2 Comparison of modal and transient load analysis results

Upon comparing the static FEA of the optimized and original fitting, it was concluded that the new fitting is more reliable than the original one in terms of static loading. In addition to the comparison of static FEA results, a dynamic FEA is also performed to compare the results of the analyses performed on the original and optimized fitting. Dynamic analysis is carried out in two steps. First, the comparison includes only free and constrained modal analysis of fitting. Then, the complete system model's modal and transient load response analyses are carried out in the second step. The following material properties are used for optimized fitting in the FEA campaign steps. Non-HIP material properties obtained from tensile tests are utilized for Ti-6Al-4V elastic properties. Aluminum alloy properties are used as-is. The analysis is carried out by utilizing Hypermesh® and Optistruct® commercial software. Material properties for both original and optimized fitting are listed in Table 4.5

Table 4.5 Material properties for dynamic analysis.

| | Original fitting (7050 Aluminum) | Optimized fitting (Ti-6Al-4V) |
|------------------------------|-------------------------------------|----------------------------------|
| Modulus of elasticity [GPa] | 71 | 116 |
| Density [kg/m ³] | 2823 | 4429 |
| Poisson's ratio ν | 0.33 | 0.30 |

Free case modal analysis is carried out for both fittings. The frequencies of the first three modes, excluding rigid body modes, are listed in Table 4.6. Although the first mode frequencies are close to each other, the natural frequencies of the optimized fitting are lower due to its comparably less stiff nature. If the optimized fitting is excited on these modes, relatively higher displacements may be expected compared to that of the original fitting, but fortunately, as these frequencies are so high (i.e., at the kHz levels), the corresponding displacements will still be relatively low.

Table 4.6 Free mode frequencies excluding rigid body modes

| Mode # | Frequency [Hz] | |
|--------|----------------|-----------|
| | Aluminum | Ti-6Al-4V |
| 1 | 1290 | 1240 |
| 2 | 2370 | 1670 |
| 3 | 2400 | 1710 |

Although both fittings have almost equal stiffness as the first eigenfrequency, there is a noticeable deviation in later modes' stiffness. However, these frequencies are still very high and will not be an obstacle from a dynamic point of view. The first three mode shapes are also shown in Figure 4.24 to see if new mode shapes are formed because the geometry has changed. It has been observed that the first three mode shapes are similar.

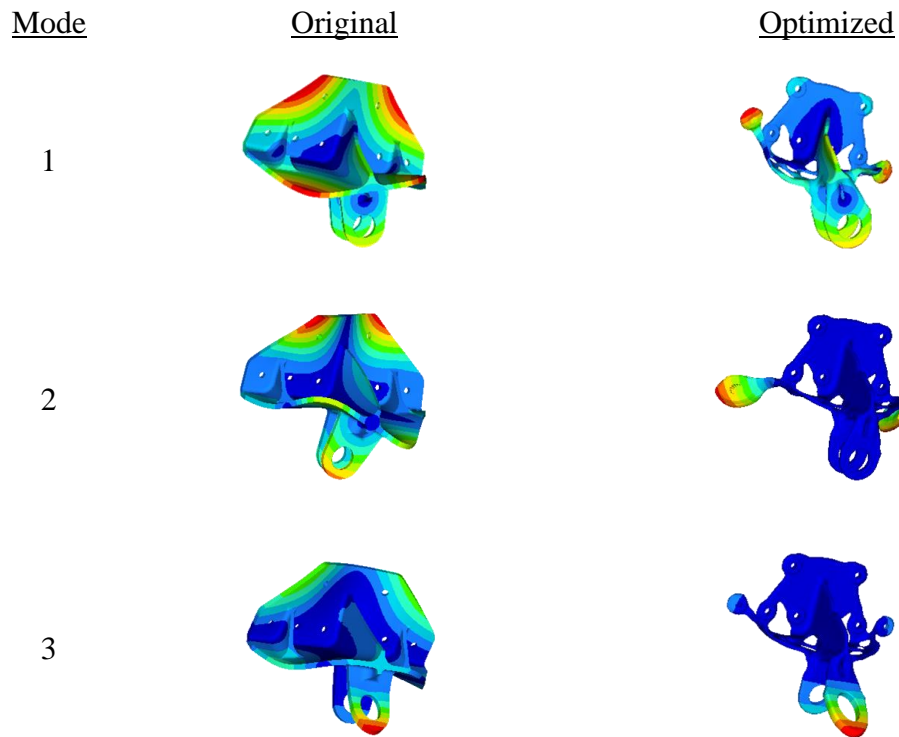


Figure 4.24. Comparison of the first three modes of pre- and post-optimization for an unconstrained case.

The FEM depicted in Figure 4.25 is utilized for modal and transient load analysis of the whole system. This model is also established for the original fitting, and it represents the interconnection beam and payload as concentrated masses. The interconnection beam and payload are rectangular prisms with approximate dimensions and their moments of inertia are calculated accordingly. The mass properties entered in the FEM data are also given in Figure 4.25

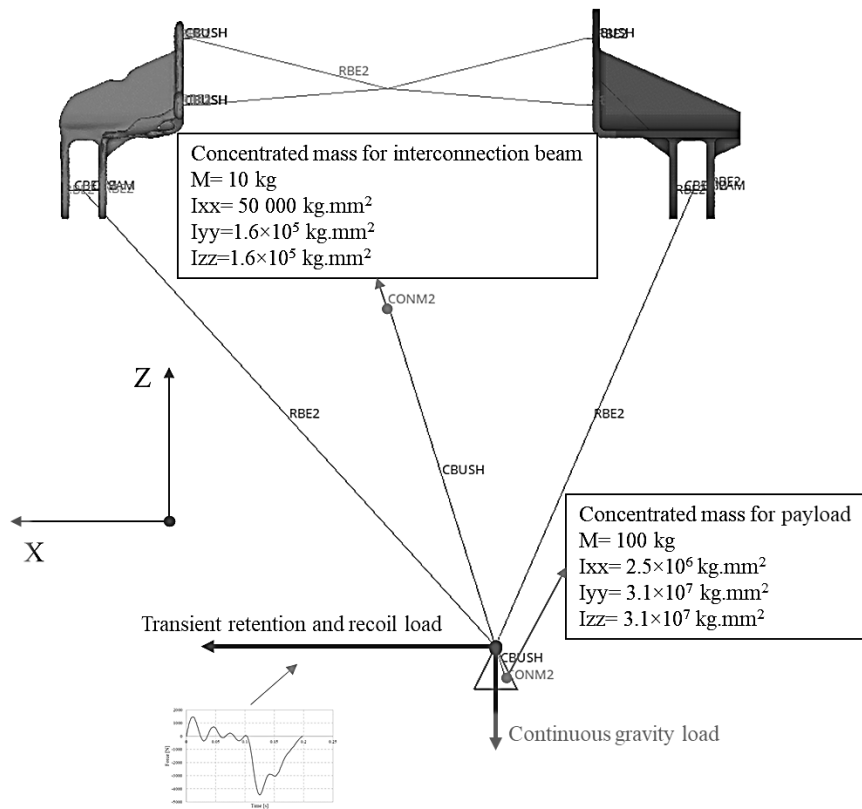


Figure 4.25. FEM for calculation of system modes and transient load response.

Transient load resulting from the payload's retention and recoil is applied to the center of gravity (CoG) of the interconnection beam and payload. The applied transient load takes 0.2 s, which is shown in Figure 4.26. This force acts parallel to the ground, as depicted in Figure 4.25. Gravity load is also applied to the CoG continuously.

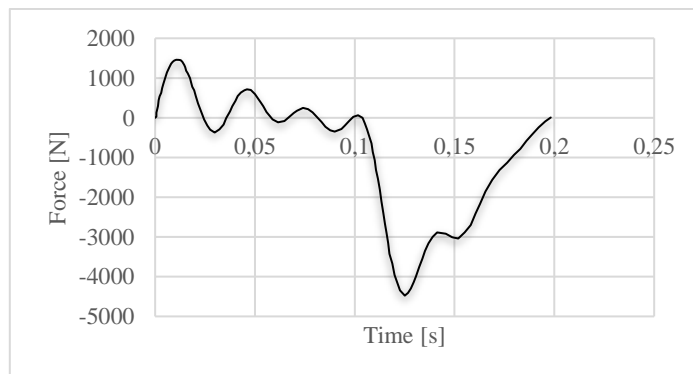


Figure 4.26. Retention and recoil force in parallel to the ground direction.

Transient load analysis at Optistruct® is carried out by modal based solution. This solution method gives natural frequencies as a result and solves the problem faster when compared to the direct method. After the analysis is completed, the natural frequency data is then extracted from the output file. A comparison of the first five natural frequencies is listed in Table 4.7. Although there are discrepancies, percentage differences are mostly at low levels. Transient response analysis will show the effect of dynamic behavior differences more clearly.

Table 4.7 System natural frequencies

| Mode # | Frequency [Hz] | | |
|--------|----------------|-----------|--------------|
| | Aluminum | Ti-6Al-4V | % difference |
| 1 | 6.69 | 5.56 | - 16.89 |
| 2 | 22.70 | 23.40 | + 3.08 |
| 3 | 50.60 | 41.70 | - 17.59 |
| 4 | 118.00 | 121.00 | + 2.54 |
| 5 | 190.00 | 189.00 | - 0.53 |

While establishing the FEM, acceleration data for both models are requested as output for 1.2 s; after some trial analysis, it was observed that the response vibrations are attenuated in 1.2 seconds. Upon completing the analyses, the acceleration data is extracted from the point shown in Figure 4.27 for three orthogonal directions as the maximum displacement and acceleration occur at this particular point.

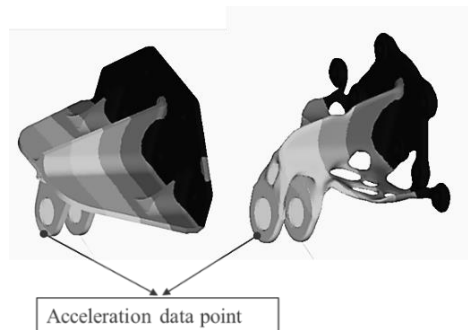


Figure 4.27. Acceleration data acquisition point for each model.

Shock Response Spectrum (SRS) analysis is performed for both acceleration outputs to assess the vibration data that is a response to the transient load. SRS analysis is valuable for predicting mechanical shock loads' damage potential and obtaining shock test data [63]. SRS is a method that graphically displays the response of a single degree of freedom (SDOF) mass-spring system after a shock or any other transient load input [64]. SRS modeling converts the continuous system to a discrete group of linear SDOF mass-spring systems. Maximum responses of each mass-spring system are extracted and plotted in the frequency domain. Furthermore, damping is also required for SRS analysis. Generally, in most applications, damping is usually taken as 5%, equal to $Q=10$. The Q factor also called the quality factor of a resonant vibration, is defined as the ratio of the center frequency of the resonance to the half-power bandwidth. A higher Q value indicates lower damping and lower energy loss. Figure 4.28 illustrates the SRS modeling fundamentals.

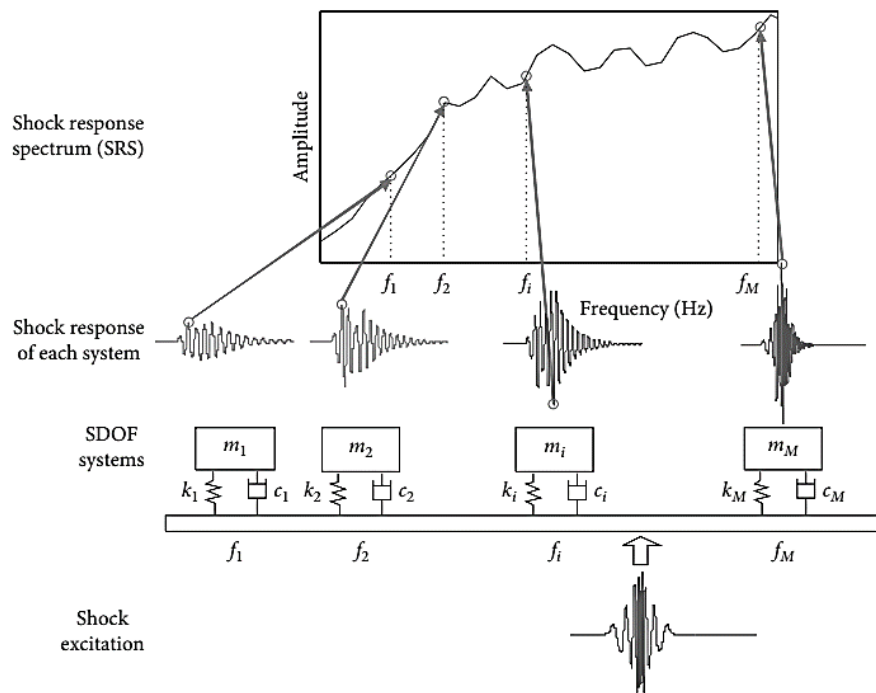


Figure 4.28. Explanation of shock response spectrum [64]

This research uses a Matlab® script written by Irvine [65] for SRS analysis. Figure 4.29 summarizes the results of the SRS analysis of acceleration time data extracted

from the tip point of original and optimized fittings in three orthogonal directions, X, Y, and Z, shown in Figure 4.25. The acceleration in the Y-axis is negligibly low. It does not contain any information for comparison. The SRS results in the X and Z axes are almost identical to the original and optimized fittings. Therefore, the optimized fitting will not adversely affect the structures or electronic equipment where it has the interaction. Effects of the initial two-mode frequencies are also shown in the graph.

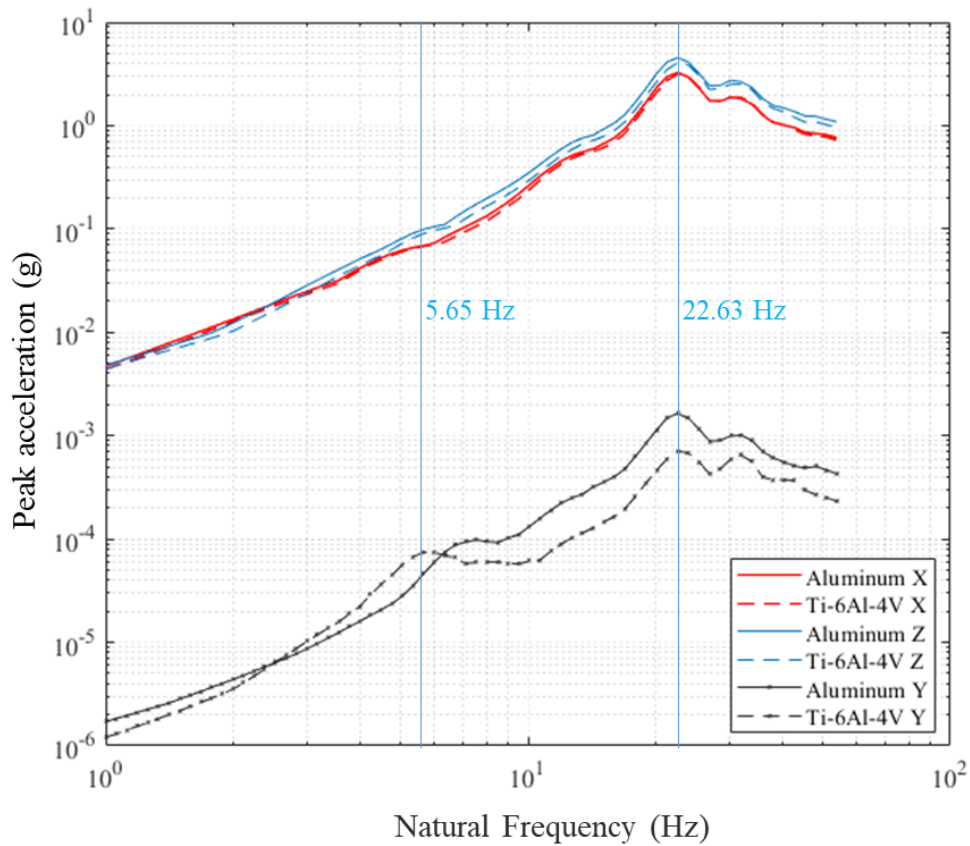


Figure 4.29. Calculated shock response spectrum for $Q=10$.

4.3.3 Double shear lug static analysis

The method in [66] is used for the lug analysis of the fitting. The methods in this resource are widely used and accepted in the aerospace industry. The method for double shear lug static analysis is elaborated in Appendix G. The formulation and

coefficients in these methods are obtained by testing for different aluminum and titanium alloys and steels.

Bearing yield strength data is retrieved from the pin-bearing test results in Section 3.4 and is utilized for the calculations. The minimum yield strength among averages of each build direction is taken to be conservative. In this lug analysis calculations for optimized fitting, yield strength for $e/d = 1.5$ is required, and for $e/d = 2.0$ yield strength is not required. If so, conventional material yield properties could be used for ultimate bearing strength since test results were not reliable due to the extreme bending of the pin. However, the pin-bearing characteristic is close to the conventional results. Figure 4.30 shows bearing yield strength presentations and used yield strength value.

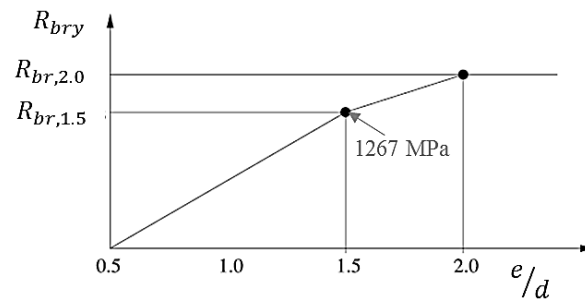


Figure 4.30. Bearing yield strength data obtained from pin-bearing tests.

The smallest of the calculated values will be load-carrying capacity. The calculations assume that there is no gap between male lug and clevis. The dimensions given in Figure 4.31 are those used in this calculation. The main clevis is a tapered lug with two lugs with different inner diameters of 22 mm and 20 mm.

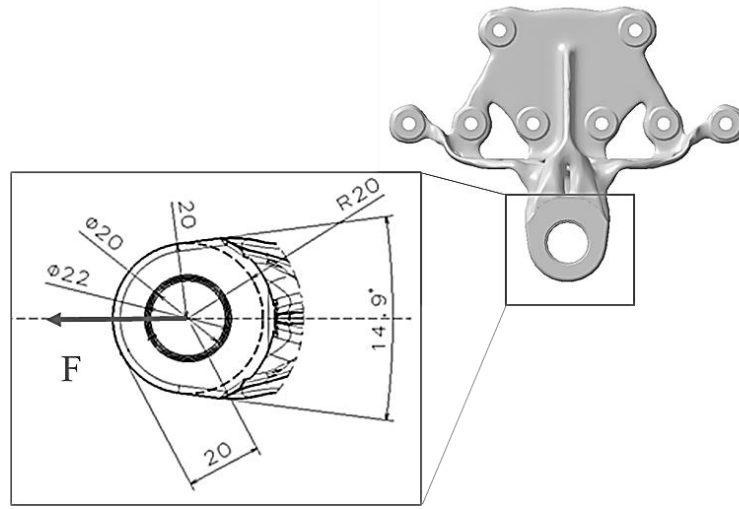


Figure 4.31. Geometric dimensions for calculation.

The representation of calculated forces of clevis lugs is depicted in Figure 4.32. The free-body diagram generation is achieved via a Hypermesh ® tool and force direction is retrieved from this free body diagram. . The analysis gives results for compression; however, the lug analysis tension case is considered since it may also be exposed to the tension. The calculation summary is presented in Table 4.8. Here the least load exposed to one of the clevis lugs is F_{Lu} , which is 75272 N. Therefore, the maximum force the clevis can carry is $2 \times 75272 = 150544 \text{ N}$ which is equal to 15346 kgf. Multiplication by 2 comes from two lugs. The equivalent force calculated for 28° loading direction is 277 kgf, as explained in Section 4.3.5. Furthermore, the force coming into the lug will be $2 \times F_{Lu} / \cos(28) = 17380 \text{ kgf}$. Then reserve factor for clevis will be $17380 / (1.15 \times 277) = 54$. A 2.5 reserve factor is required if shock or vibration with infrequent rotation is present. Gun mounts, landing gear, hoisting, and towing connections may be among these types of structures. 1.15 fitting factor is recommended in [67] and used here for reserve factor calculations.

Table 4.8 Calculation summary for double lug shear analysis

| Parameter | 22 mm lug | 20 mm lug |
|-----------------|-----------|-----------|
| F_{Lu} [N] | 75272 | 79927 |
| F_{Ly1} [N] | 107588 | 119543 |
| F_{Ly2} [N] | 116206 | 123392 |
| $F_{Ly,br}$ [N] | 94075 | 104528 |

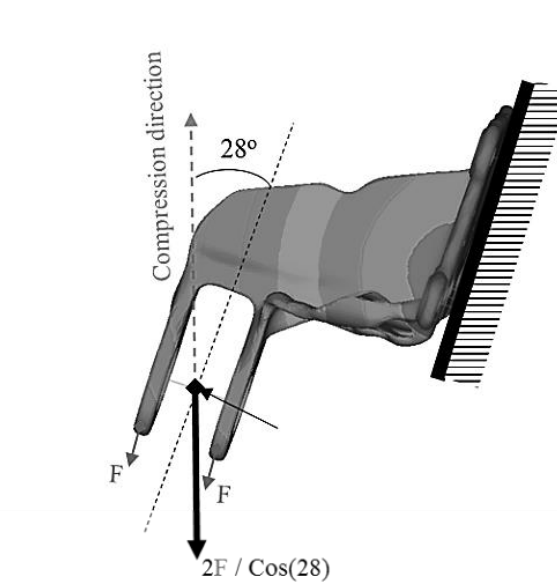


Figure 4.32. Representation of equivalent force direction.

4.3.4 Estimation of fatigue life of the optimized fitting

The fatigue properties of the material under constant amplitude with the $R=0.1$ stress ratio are already determined by ASTM E466 standard testing. However, fitting is exposed to random amplitude loads with different cycles in the operating conditions. These amplitudes are classified by rain-flow cycle counting analysis, depicted in Figure 4.33. This method is called “rain-flow” because cycle counting is done by modeling drops sliding from a pagoda tree.

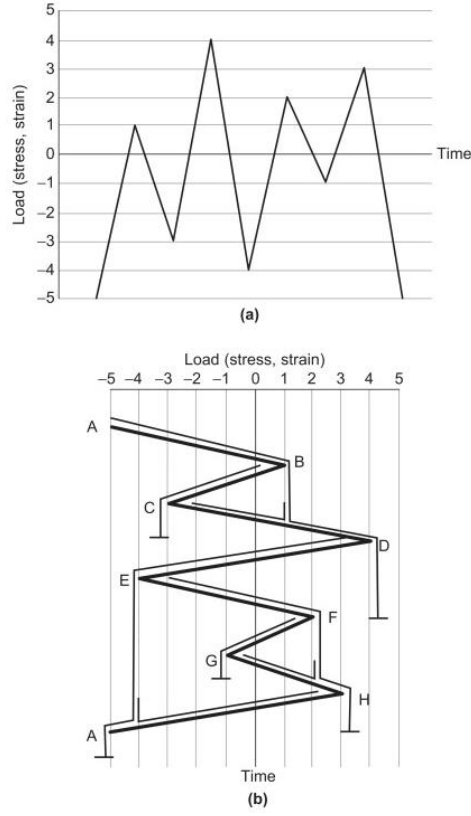


Figure 4.33. (a) load-time history, (b) rain-flow cycle counting [68].

On the other hand, Miner's rule calculates the damage by counting the cycles according to stress levels. Damage to the structure with maximum stress S_{\max} and R stress ratio is assumed as linear accumulation. If N_i is the life of the corresponding stress level, damage can be calculated after n_i cycles by equation 4.5.

$$d_i = \frac{n_i}{N_i} \quad 4.5$$

According to Miner's rule, the total damage is the sum of these damages. Finally, damage occurs after D reaches value one, where D is calculated by equation 4.6.

$$D = \sum_i \frac{n_i}{N_i} \quad 4.6$$

Random loading can be converted to quasi-monotonic loading by rain-flow cycle counting and Miner's rule, as depicted in Figure 4.34, in order to calculate an equivalent stress S_{eq} .

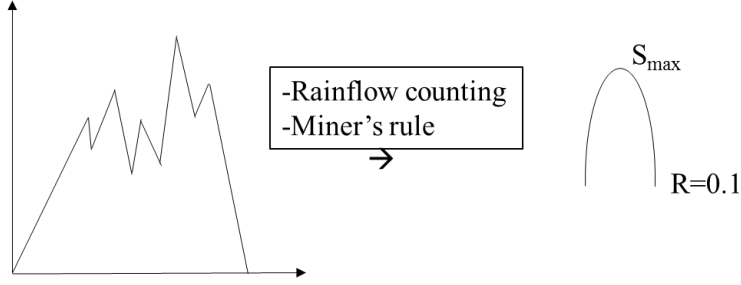


Figure 4.34. Conversion to monotonic loading.

The fatigue equivalent stress will represent S_{max} of simulated monotonic loading, which is used in equation 4.7 [55].

$$\frac{1}{N} = \sum_i \frac{1}{N_i} \rightarrow \frac{1}{10^5 \left\{ \frac{IQF}{S_{eq}} \right\}^p} = \sum_i \frac{1}{10^5 \left\{ \frac{IQF}{((1 - R_i)/0.9)^q \cdot S_{max}} \right\}^p} \quad 4.7$$

Then S_{eq} can be simplified by equation 4.8;

$$S_{eq} = \left\{ \sum [((1 - R_i)/0.9)^q \cdot S_{max}]^p \right\}^{1/p} \quad 4.8$$

If there is a specific fatigue life cycle load data, a coefficient can be deduced for S_{eq} calculation from equation 4.9.

$$C_S = \frac{S_{eq}}{S_{FLC}} = \frac{\left\{ \sum [((1 - R_i)/0.9)^q \cdot S_{max}]^p \right\}^{1/p}}{S_{FLC}} \quad 4.9$$

However, if there is no available data, then C_S can be taken as 0.75 for the pre-sizing purpose from the inheritance of aircraft projects, as it is used here as 0.75 for fatigue life calculations. S_{FLC} must be positive stress for tension cases for equation 4.10.

$$S_{eq} = C_S \cdot S_{FLC} \quad 4.10$$

For the optimized fitting, Von Mises stress has the highest value compared to max principal stress, and therefore, Von Mises stress will be S_{FLC} for calculations. Von Mises stress is retrieved from Table 4.4 and the life cycle is calculated according to the IQF method described in Section 3.3.2. IQF will be the minimum average of the as-built case in three build directions to be conservative. On the other hand, since surface quality is not good enough at the fitting, a surface factor of 0.33 will be utilized. Fatigue tests in this study are performed on machined specimens, and machining can increase fatigue life by leading to residual stress on the surface [11]. The surface coefficient typically exists in the IQF equation; however, it is already taken as one from previous calculations. Then, it must be included for fitting calculations since the fitting surface is not machined.

$$N = 10^5 \cdot \left(\frac{0.33 \times IQF}{S_{eq}} \right)^p = 10^5 \cdot \left(\frac{0.33 \times 385}{0.75 \times 327} \right)^{4.5} = 5184 \text{ cycles}$$

If the value of 5 is used as the scatter factor, 1037 cycle is calculated for the fatigue life after reduction with scatter factor. This fatigue life cycle complies with the min 1000 cycle requirement of this UAV; therefore, the fitting has the desired features in terms of fatigue.

4.3.5 Additive manufacturing and testing of the optimized fitting

During this study, the literature and industry applications research and the experience gained during the production of test specimens are used to select build direction (Figure 4.16) according to the functionality of the fitting. A guideline is prepared to optimize the build direction and prepare the manufacturing data. The optimized pylon fitting is additively manufactured in light of this particular guideline.

Build direction optimization criteria need to be established to ensure that part manufacturing is repeatable. Following build direction optimization criteria is a valuable guide for additive manufacturing designers:

- Minimize support structure by minimizing hanging surfaces.
- Avoid converging geometries along the build direction.
- Orient the part inside the build tank to obtain support-free surfaces.
- Vertical direction surface regions should be maximized.
- Thermal heat sinks towards the layers should be minimized.
- Avoid sharp cross section variations along build direction.

This optimization criteria are also given in Figure 4.35 summarizes the general guidelines for the build direction optimization. Here, the build direction optimization criteria are valid for metallic powder bed fusion additive manufacturing methods and may differ from other additive manufacturing methods.

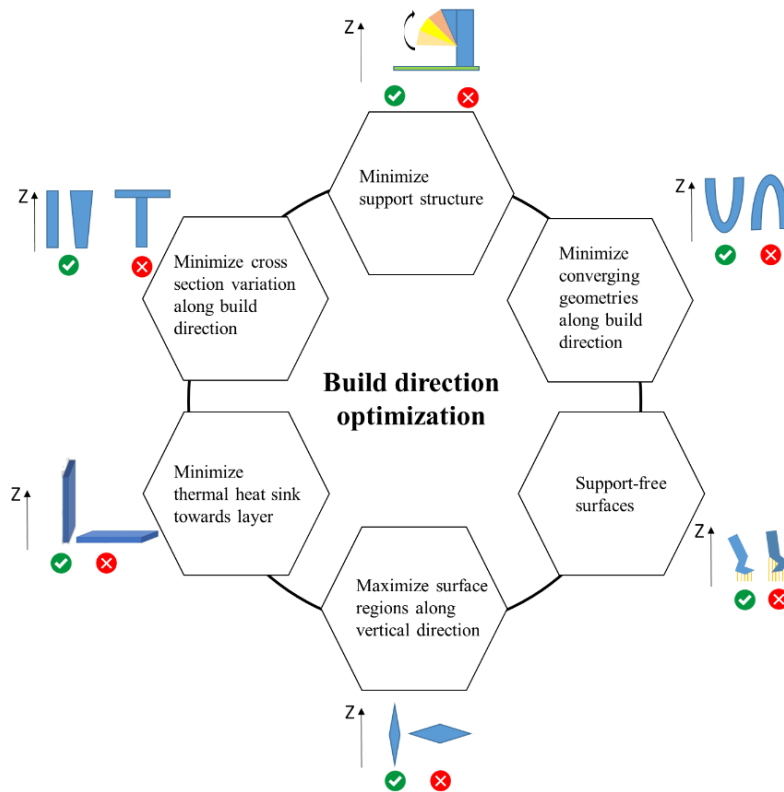


Figure 4.35. Build direction optimization.

Following the optimization of the part's orientation in the manufacturing volume and the 3D model creation, the quality of the 3D model must be checked. Since it is transferred to manufacturing as an STL file, the resolution of the 3D model must

have sufficient details. It should be ensured that the build direction data, support structure information, functional zones, roughness, material offset, part tolerance, and additive manufacturing engineering requirements such as heat treatment or protective coating of the part are also available in the overall design data set during the model quality check.

Build direction data should be displayed in 3D models and explanatory 2D drawings. By adding a new axis set in 3D models, the z-axis of this new axis set can show the build direction, and it must be shown that it is the build direction by naming. In 2D drawings, the build direction can be shown as depicted in Figure 4.36.

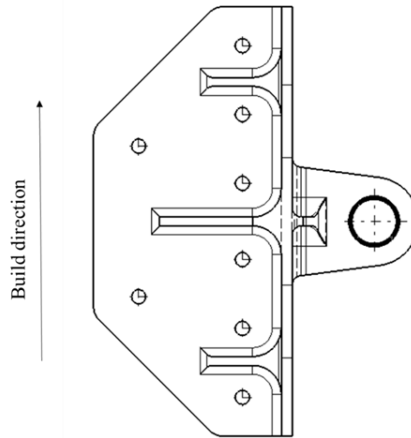


Figure 4.36. Sample build direction on the 2D drawing.

The regions where the support structures are applied should also be shown in the 2D drawing. These support structures may differ according to the manufacturing method. The representation of a sample support structure zone in the 2D drawing is shown in Figure 4.37. The functional or contact surfaces must be shown on the 2D drawing. An example is shown in Figure 4.38.

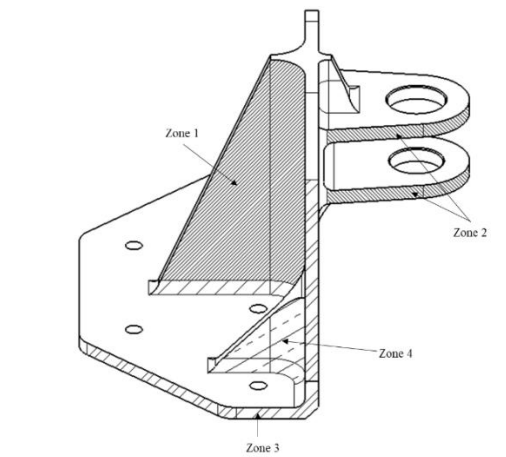


Figure 4.37. Sample support structure definition on drawing as “Zones” by hatching.

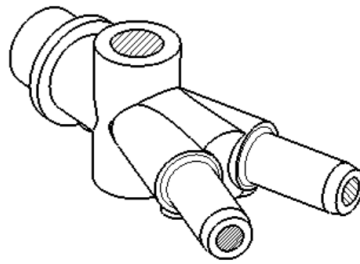


Figure 4.38. Functional zone examples shown by hatching.

Finally, leaving an offset between the rough and final parts is necessary. These offsets are then machined to ensure minimal porosity in these areas. The sample rough and final parts are depicted in 2D drawing dimensions in Figure 4.39.

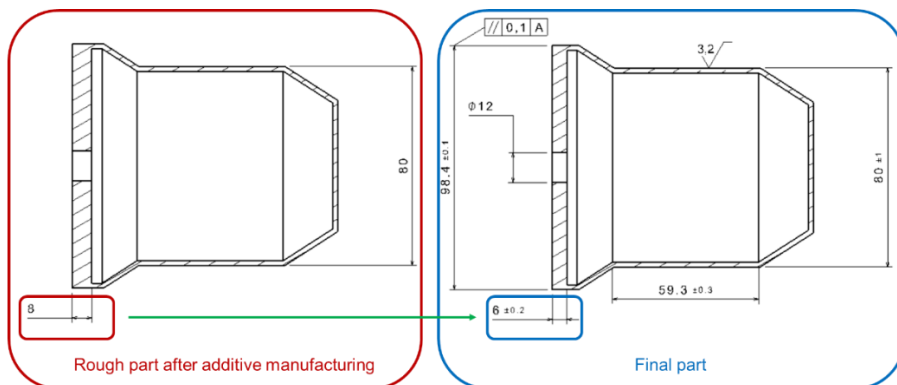


Figure 4.39. Material offset example.

After the optimized fitting is validated according to the results obtained from static, dynamic, lug, and fatigue analyses with the mechanical properties obtained from material characterization tests in Chapter 3, it is manufactured by EBM. Manufacturing with the support of design for additive manufacturing guidelines is achieved after two attempts. Figure 4.40 shows the manufactured fittings at each attempt. Moreover, since the desired surface quality for functional surfaces is insufficient after EBM manufacturing, the holes are left as pilot holes with a diameter of 2.5 mm.

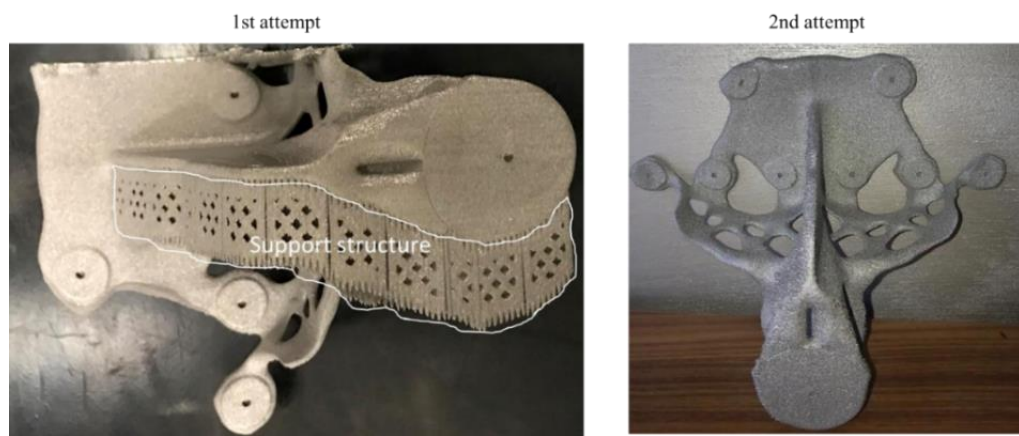


Figure 4.40. Optimized fitting manufactured by EBM after two attempts.

After additive manufacturing, the fastener and lug hole diameters are expanded to their final dimensions, and weight measurement is carried out. Weight measurement is given in Figure 4.41, where pre and post-geometry are also shown. Instead of the expected weight of 376 grams, 379.8 grams is measured with an insignificant deviation that may be due to the powders sintered on the fitting surface.

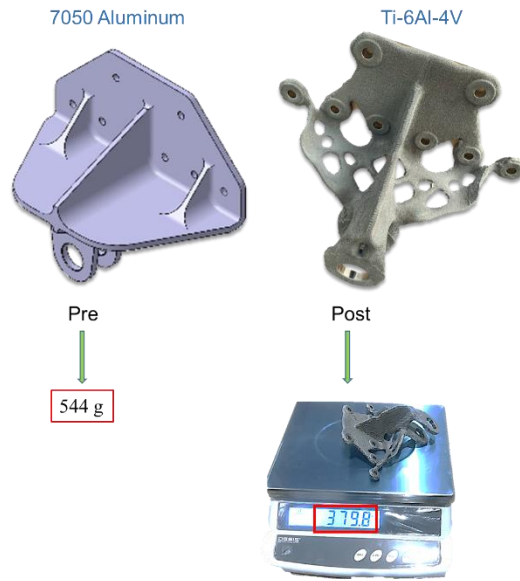


Figure 4.41. Original fitting and final optimized fitting comparison.

Subsequently, a test setup is designed to perform the static test of the manufactured fitting, and it is given as a schematic in Figure 4.42. The test is carried out by forcing the fitting in both compression and tensile directions with a mechanical jack containing a reduction gear. While loading, the amount of force is measured through a 2-tonne capacity load cell. The displacement values are obtained by image processing of images captured by a video camera and 2 scale points with a 10 mm distance are included in the test setup for calibration.

Furthermore, in order to assure that the stress values are at the level of the static FEA results, strain is measured with a 350 Ohm strain gauge placed on the stiffener. Strain and load data are also amplified by HX711 24-bit 80 Hz analog-to-digital converter. An Arduino UNO® electronic card then processes the signals. Data are transferred to a display to record during video capture, and finally, the video files are converted to sequence image files for image processing. Displacement data acquired by image processing are recorded manually in order to synchronize the displayed force and strain values.

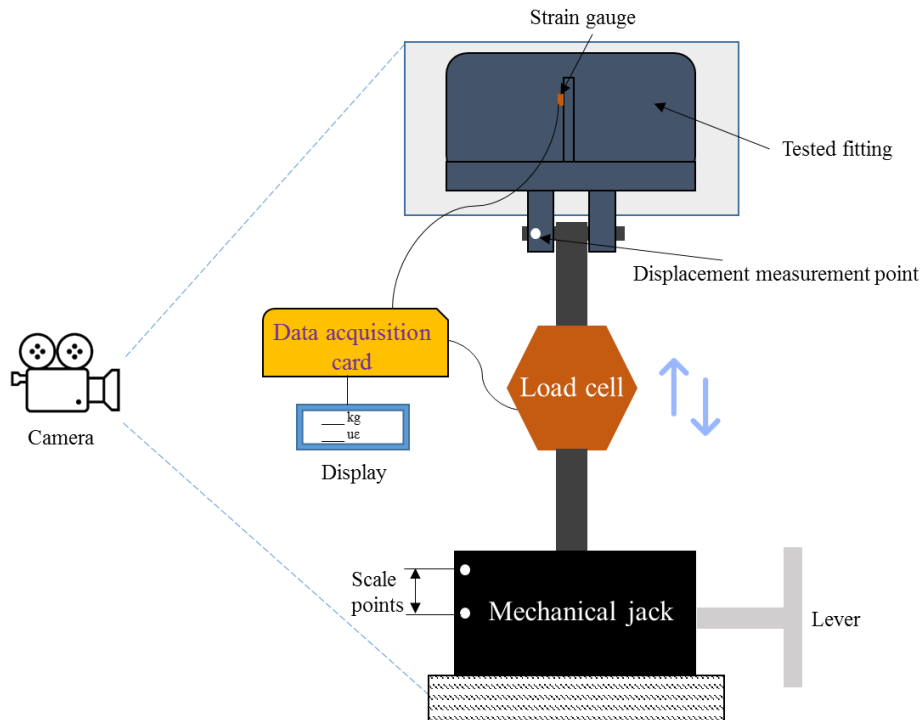


Figure 4.42. Static test setup schematic for qualification of the optimized fitting.

Since the test setup applies only linear force in a fixed direction, it will not be possible to apply the forces in the system-level FEA. Therefore, an equivalent force must be determined. In the static analysis, the free body diagram of the node in the middle of the lug is retrieved. In this free body diagram, it is observed that the force acts at an angle of 28° . While carrying out the tests, forces will also be applied at this angle. In order to determine the forces to be applied, a static FEA is performed, showing the test case in Figure 4.43. Since the load cell is calibrated according to kg, the unit of forces applied in the FEA is also in kgf.

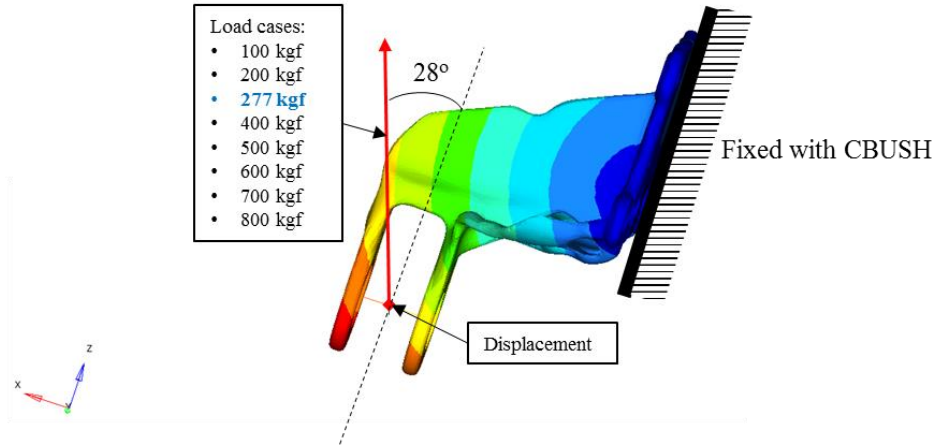


Figure 4.43. Test case FEA and loadings.

In the test case FEA, the load is applied gradually, and the force equivalent to the system level maximum Von Mises stress is calculated by interpolation as 277 kgf. This force is also added to the analysis, and the applied force values are shown in Figure 4.43. Furthermore, displacement data is obtained for gradual loadings at the lug center node point. As a result of these analyses, it is calculated that the fitting can withstand up to 600 kgf, which is approximately twice the maximum launch load where the yield limit is reached. The von Mises stresses for these two loads are shown in Figure 4.44 where 600 kgf is at the threshold of yield strength.

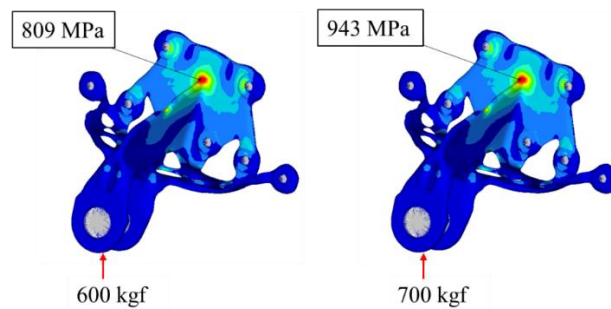


Figure 4.44. Resultant max von Mises stresses for 600 kgf and 700 kgf.

A location is selected for the strain gauge measurement (Figure 4.45) to check whether the stresses on the fitting are in line with the FEA due to the applied loads. This point is selected since it is easy to bond strain gauge and solder the cables. The direction of the minimum principal strain is selected from tensor displays, and those values for each load step are obtained from FEA for later comparison with test data. Upon the calculation of forces to be applied, the displacement and strain values, the test setup is established, and the view of the test setup is shown in Figure 4.46. A Wheatstone bridge for the quarter bridge is built for strain measurements.

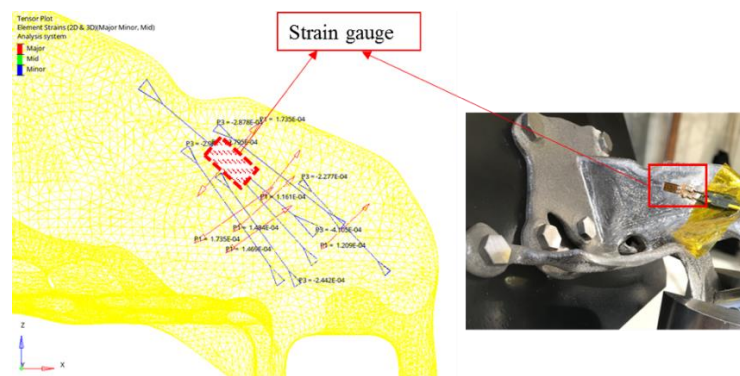


Figure 4.45. Strain gauge bonding location selection.

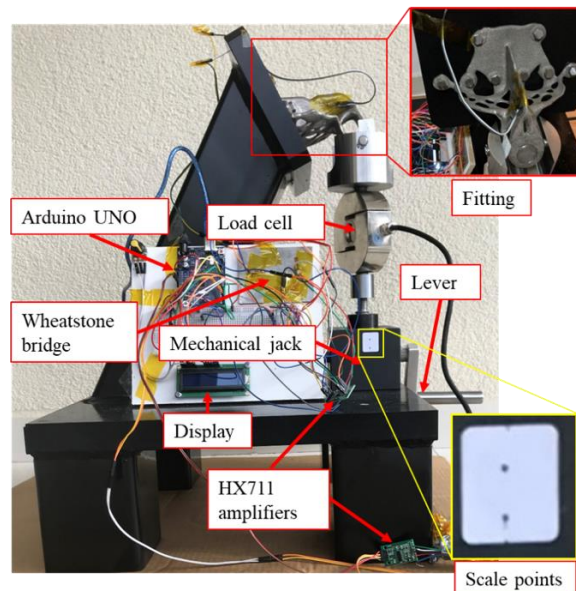


Figure 4.46. Test setup installation.

A video is recorded with the video camera by orienting the scale and measurement points in the center of the image during the fitting loading. The captured video is converted into image frames divided into equal time intervals. Then, the section where only the measurement part of these images is cut, and it is ensured that pixels are captured from the desired measurement points. Finally, the calibration is carried out with scale points. A snapshot of the measurement is shown in Figure 4.47.

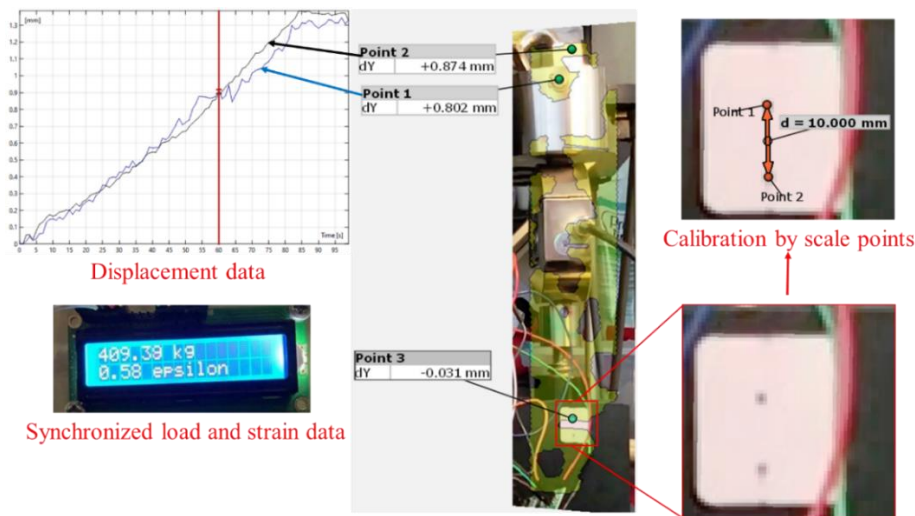


Figure 4.47. Image processing and data acquisition.

After the calibration, measurements are taken from Point 1 and Point 2 located on the captured images. While the displacement measurement on the images is carried out, the change of the location of the points and the colors corresponding to the pixels on the image are traced with the help of image processing, although some changes in pixels cannot be captured at the same desired quality for every point. Here in this part, data on Point 2 is used to obtain the displacement as this data is captured more consistently than the ones provided by Point 1. Corresponding force and microstrain values are retrieved manually by the same frame number from the relevant image. The obtained data from these measurements and the data obtained from the FEA are then compared in Figure 4.48. The load values used in the FEA and the static test are on the graph's horizontal axis, and both the displacement and microstrain values are on the two vertical axes. The deviation in displacement is calculated for each loading

point from the analysis result. According to these results, there is around 4% to 20% displacement deviation between test and analysis data, where deviation varies at almost every point. Furthermore, although the deviation in strain values seems to be high at low-level strains, it regresses to 2% as the load increases.

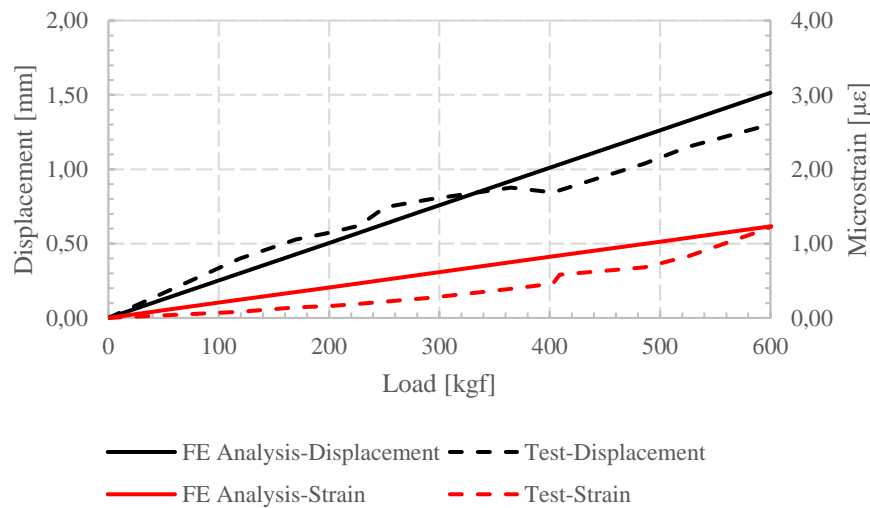


Figure 4.48. Comparison of static FEA results and the test data.

Finally, the fitting is intended to be qualified under both compression and tension. For this purpose, a 600 kgf loading is applied (Figure 4.44), which provides results close to yield strength and is approximately twice the equivalent load of 277 kgf. Following the application of the loading both in compressive and tensile directions for the duration of three minutes, the load is then released, and it is observed that the fitting returns to its original undeformed position by showing a complete elastic deformation. Even though the weight of the fitting is reduced, it still provides conservative results. If a factor such as a casting factor is applied in the future, this excess in static strength will create a safety margin for the casting factor for calculations.

The case study concluded that the fitting manufactured by EBM with Ti-6Al-4V material with 31% less weight could be used instead of the original aluminum fitting. Furthermore, the new design is not only lighter than the original one and also more reliable according to the calculated reserve factors.

CHAPTER 5

CONCLUSION

5.1 General conclusions

The use of additive manufacturing, previously used only for rapid prototyping, has not only recently gained momentum in the manufacturing of aerospace structural parts but also in many other industries. Furthermore, airframe manufacturers put significant investments and research into this particular area.

The additive manufacturing method brings many advantages, such as directly producing design data, reducing lead times, eliminating the need for spare parts storage, producing assemblies consisting of many parts as a single piece, near-net-shape production, and rapid prototyping. In addition to these advantages, the manufacturing constraints in conventional production methods could also be eliminated by additive manufacturing. Thus, complex-shaped but lighter parts are designed as a free-form design that can be manufactured quickly and efficiently. This paves the way for structural optimization and weight reduction in aerospace structural parts, resulting in decreased fuel consumption and increased aircraft flight performance.

Additive manufacturing can be divided into two main groups such as; non-metallic and metallic, which include various additive manufacturing methods. This thesis focuses on the electron beam melting (EBM) method, which is a powder bed fusion metallic additive manufacturing method. The additive manufacturing machine used in this study is called Arcam Q20 Plus, and it was developed especially for the manufacturing of airframe structures. Moreover, since the machine is calibrated only for Ti-6Al-4V titanium alloy, the investigation and the modeling of the effect of this additive manufacturing method on the output material's mechanical performance is the primary aim of this study. For this purpose, a series of tensile, fatigue, and pin-

bearing tests have been performed to investigate whether the final product can be used in aerospace applications.

In these test campaigns, two different types of specimens, such as; as-built specimens, which are not exposed to any post-treatment method, and hot isostatic press (HIP) post-treated specimens, have been used. This post-treatment aims to close unwanted pores under high pressure and high temperature. In order to investigate the aimed effect of this particular post-treatment, the internal structure of three as-built and three HIP post-treated tensile test specimens, each representing a build direction, have been visualized by computerized microtomography. Moreover, the test specimens are manufactured with three orthogonal build directions so that the effect of build direction on material properties can also be investigated.

After the investigation of mechanical performance, it has been aimed to benefit from the design freedom feature of additive manufacturing together with the topology optimization, and for this purpose, a case study has been carried out. Topology optimization is a structural optimization method used for weight reduction by free-form design for many years to obtain lightened but inevitably complex geometries that are difficult to produce by conventional manufacturing methods. At the end of this particular study, the mechanical properties obtained from the test campaigns are used to show structural compliance of the output part from the EBM additive manufacturing method. As a result of this weight reduction campaign, a lightened yet a complex-shaped design has been obtained. Although the original fitting has been manufactured with a less dense aluminum alloy, a 31% weight reduction has been achieved by additive manufacturing with a denser Ti-6Al-4V alloy through topology optimization. Considering that the original fitting is 544 grams and four pieces are used in an aircraft, a total of 675 grams of weight reduction shows that a combination of topology optimization with additive manufacturing may provide excellent weight reduction opportunity. Having completed the weight reduction of the fitting, it has also been validated in terms of static strength, dynamic behavior, and fatigue life according to the material properties obtained from the test

campaigns. Finally, the static strength of the fitting is validated by testing it on the custom-designed static test rig with a dedicated data acquisition system.

In conclusion, this research investigates the mechanical performance of Ti-6Al-4V alloy manufactured by EBM additive manufacturing. Moreover, a scientific philosophy about research on additively manufactured materials is established, and all the outcomes are then applied to a UAV fitting. Although this study is limited to the use of EBM and Ti-6Al-4V alloy, the findings provide a guideline for various additive manufacturing methods and materials.

Stress-strain graphs of the material are obtained from the tensile test campaign, and mechanical properties such as modulus of elasticity, Poisson's ratio, yield strength, ultimate strength, and elongation are then extracted from these graphs. The digital image correlation (DIC) method is also used for both strain measurements during the tensile tests and Poisson's ratio measurements, as the samples have rectangular cross-sections. As a result of the measurements, it is observed that both as-built and HIP samples show isotropic material properties in the elastic region regarding three build directions. However, there is a slight difference between Poisson's ratios of the longitudinal and short transverse samples among all statistical analysis groups. This difference in Poisson's ratio may cause slight deviations in the stress calculations of horizontally manufactured thin walls, which should be considered in the structural analysis. On the other hand, in the plastic region, the material shows negligible anisotropic behavior. Although the modulus of elasticity is slightly higher than the conventional alloy, the Poisson's ratios are measured close to each other. When the yield and the ultimate strengths in the plastic region are compared, as-built samples are observed to be the highest strength material among all, followed by HIP samples and conventional alloy as comparably the lowest strength material. However, considering the elongation and the reduction of area properties for the ductility, the samples produced by additive manufacturing show fragile behavior. Investigation of the tensile properties showed that Ti-6Al-4V material manufactured by EBM additive manufacturing is approximately 6% stiffer than the conventional alloy. The yield and ultimate strengths of HIP post-treated materials are approximately 4%

superior to conventional materials. Also, the yield and ultimate strengths of as-built materials are approximately 9% superior to conventional alloy; however, the elongation is almost 38% worse. Therefore, EBM results in higher strength and stiffness properties with a lower ductility in comparison to the conventional alloy. In the tensile test results, it is observed that HIP post-treatment does not affect elastic properties. It slightly reduces yield and ultimate strength but has limited effect. However, although as-built specimens show more random elongation behavior, HIP post-treated specimens exhibit a more reliable behavior. Considering all these results, there is no need for HIP post-treatment on the aerospace structural parts to be used in the elastic region. On the other hand, HIP post-treatment must be applied to structural parts which are anticipated to work in the plastic region.

Following the completion of the tensile tests, fatigue properties are also aimed to be obtained by performing a test resulting in the SN curves and the Goodman-Haigh diagrams for high cycle constant amplitude loading with a stress ratio (R) of 0.1. Furthermore, a power index and a material constant reflecting the fatigue characteristics are also recalculated for the additively manufactured specimens by using the test results. It is observed from the fatigue test results that as-built specimens show better fatigue life properties than the HIP ones; however, the fatigue properties of both as-built and HIP specimens are far below the conventional alloy when material and index constants are compared. Nevertheless, fatigue life can be modeled with the aforementioned material constants and used for future fatigue life calculations of aerospace structures. Moreover, when analyzed in terms of the p -index used in the IQF method used by Airbus for the fatigue life calculations and reflecting the material properties, the p -index values of HIP post-treated and as-built samples are calculated as 5.5 and 4.5, respectively. This value is actually given as 6.5 in the Airbus fatigue manual for titanium alloys. The M coefficient, which reflects another material property to fatigue life calculations, is approximately below 40% of conventional alloy coefficients. Both p -index and M coefficient show that the fatigue properties of additively manufactured Ti-6Al-4V are well below conventional material for both as-built and HIP post-treated specimens; however,

these findings still shed light on forthcoming studies and applications. Regarding the obtained fatigue properties, it is recommended that both HIP post-treated and as-built aerospace structural parts manufactured with EBM should not be used in critically essential parts in manned flights. Instead, using the EBM additive manufacturing method in unmanned aerial vehicles and spacecraft parts is more appropriate.

Finally, a pin-bearing test campaign has been carried out for two different hole edge distances, namely, $e/d=1.5$ and $e/D=2.0$. The pin-bearing test campaign results in almost similar strengths compared to the conventional material pin-bearing yield and ultimate strength properties. In addition to revealing pin-bearing yield and ultimate strengths, failure modes that occur in the holes resulting from pin-bearing have also been investigated and classified. As a result, the dominant failure mode in most as-built specimens is the “shear-out” mode, and the “tension cleavage” failure is more commonly observed in HIP post-treated samples. To summarize, pin-bearing properties are similar to conventional Ti-6Al-4V alloy. On the other hand, HIP post-treatment has no significant effect on pin-bearing properties, so there is no obstacle in using the EBM additive manufacturing method on aerospace structural parts in terms of pin-bearing properties.

When it is aimed to evaluate outcomes in terms of design criteria, although the build direction has little effect on mechanical performance, it should be taken into account that the longitudinal build direction in designs gives better results for the target geometry. Furthermore, another outcome of this study is that although the HIP closes the unwanted pores, the support structures should be avoided since these temporary structures give rise to dense pores which can be observed through microtomography imaging.

As a result, outcomes show that the materials obtained from additive manufacturing can be used for producing aerospace structures and contains great potential for weight reduction of the fittings and the brackets. With the further advancement in

this technology, larger structures, even the entire structure of an aircraft, will be able to be produced via additive manufacturing.

5.2 Recommendation for future work

This study investigated the mechanical performance of Ti-6Al-4V alloy manufactured by an electron beam melting (EBM) additive manufacturing machine. When this machine is to be used in the mass production of aerospace structural parts, the approval of the relevant aviation authorities is required. When this particular need and the other scientific gaps in this area are considered together, the following studies are recommended for future work:

- Crack propagation properties should be investigated for damage tolerant parts.
- Mechanical performance should be investigated for elevated and cryogenic temperatures for specific use.
- The effect of surface roughness on fatigue life should be investigated.
- Residual stresses sourced from thermal effects during the manufacturing should be researched to include in fatigue life models.
- Although the material properties obtained from EBM seem suitable for aerospace structures in light of the obtained as-built and HIP properties, the effects of different heat treatments may also be further investigated.
- Chemical and/or mechanical methods could be developed to reduce the surface roughness after manufacturing.
- The number of specimens must also be increased for airworthiness certification applications. MMPDS [47] can be used as a reference for the number of test specimens that is required for material properties to be reliable in aerospace applications.
- A factor such as the “casting factor” may be derived for as-built and HIP materials for airworthiness regulations.

- Galvanic corrosion properties should be researched to show compliance with other materials.
- Rapid quality control methods such as ultrasonic measurement can be developed to show that material properties are repeatable. Relationships between the grain structure and the speed of sound can also be investigated.
- Since the as-built material has a porous structure, the porous plasticity can be modeled with the Gurson-Tvergaard-Needleman (GTN) nucleation model. Moreover, modeling the plasticity with Johnson Cook and Ramberg-Osgood model also can be carried out to reveal which model gives the best results.
- Thermal properties may be investigated to include thermal effects in structural analysis.

REFERENCES

- [1] ISO/ASTM, *ISO/ASTM 52900:2015-Additive manufacturing — General principles — Terminology*, 2015-12.
- [2] S. Mellor, L. Hao and D. Zhang, "Additive manufacturing: A framework for implementation," *International Journal of Production Economics*, vol. 149, pp. 194-201, 2014.
- [3] ARCAM, "ARCAM Q20 Plus," General Electric, 2013. [Online]. Available: <http://www.arcam.com/wp-content/uploads/Arcam-Q20-final.pdf>.
- [4] A. Mohammadhosseini, D. Fraser, S. H. Masood and M. Jahedi, "Microstructure and mechanical properties of Ti–6Al–4V manufactured by electron beam melting process," *Materials Research Innovations ISSN*:, 2013.
- [5] S. L. Draper, B. A. Lerch, J. Telesman, R. E. Martin, I. E. Locci , A. Garg and A. J. Ring, "Materials Characterization of Electron Beam Melted Ti-6Al-4V," National Aeronautics and Space Administration (NASA), Cleveland, Ohio, 2016.
- [6] C. de Formanoir, S. Michotte, O. Rigo, L. Germain and S. Godet, "Electron beam melted Ti–6Al–4V: Microstructure, texture and mechanical behavior of the as-built and heat-treated material," *Materials Science and Engineering: A*, vol. 652, pp. 105-119, 2016.
- [7] D. Greitemeier, F. Palm, F. Syassen and T. Melz, "Fatigue performance of additive manufactured TiAl6V4 using electron and laser beam melting," *International Journal of Fatigue*, vol. 94, pp. 211-217, 2017.

- [8] S. Tammas-Williams, P. J. Withers, I. Todd and P. Prangnell, "The Influence of Porosity on Fatigue Crack Initiation in Additively Manufactured Titanium Components," *Scientific Reports*, vol. 7, no. 1, 2017.
- [9] H. Shen and L. Brinson, "Finite element modeling of porous titanium," *International Journal of Solids and Structures*, vol. 44, pp. 320-335, 2007.
- [10] M. R. Kabir and H. Richter, "Modeling of Processing-Induced Pore Morphology in an Additively-Manufactured Ti-6Al-4V Alloy," *Materials*, vol. 10, p. 145, 2017.
- [11] H. A. Chern, P. Nandwana, T. Yuan, M. M. Kirka, R. R. Dehoff, K. L. Peter and E. D. Chad, "A Review on the Fatigue Behavior of Ti-6Al-4V Fabricated by Electron Beam Melting Additive Manufacturing," *International Journal of Fatigue*, vol. 119, pp. 173-184, 2019.
- [12] Ruag Group, "Additive manufacturing partnership for space applications," RUAG Space, [Online]. Available: <https://www.ruag.com/en/news/additive-manufacturing-partnership-space-applications>. [Accessed 2021].
- [13] S. Kim, X. Chen, G. Dreifus, J. Lindahl, I. Kang, J.-H. Kim, M. Selim, D. Nuttall, A. Messing, A. Nycz, R. Minneci, K. Stephenson, J. C. Bowers, B. Braswell, B. Pipes, A. A. Hassen and V. Kunc, "An Integrated Design Approach For Infill Patterning Of Fused Deposition Modeling And Its Application To An Airfoil," in *SAMPE Conference Proceedings*, Seattle, WA, 2017.
- [14] T. Wohlers and T. Gornet, "History of Additive Manufacturing," Wohlers Associates, INC., 2016.
- [15] I. Gibson, D. W. Rosen and B. Stucker, *Additive Manufacturing Technologies*, Boston, MA: Springer, 2010.

- [16] "Disrupting the Disruptors Low Cost 3D Metal Printing," 3D Printing Industry, [Online]. Available: <https://3dprintingindustry.com/news/disrupting-the-disruptors-low-cost-3d-metal-printing-149122/>. [Accessed 03 04 2022].
- [17] T. D. Ngo, A. Kashani, G. Imbalzano, K. T. Nguyen and D. Hui, "Additive manufacturing (3D printing): A review of materials, methods, applications and challenges," *Composites Part B: Engineering*, vol. 143, pp. 172-196, 2018.
- [18] D. Bourell, J. P. Kruth, M. Leu, G. Levy, D. Rosen, A. M. Beese and A. Clare, "Materials for additive manufacturing," *CIRP Annals*, vol. 66, pp. 659-681, 2017.
- [19] L. E. Murr, S. M. Gaytan, D. A. Ramirez, E. Martinez, J. Hernandez, K. N. Amato, P. W. Shindo, F. R. Medina and R. B. Wicker, "Metal Fabrication by Additive Manufacturing Using Laser and Electron Beam Melting Technologies," *J. Mater. Sci. Technol*, vol. 28, no. 1, pp. 1-14, 2012.
- [20] GE Additive, "Inside Electron Beam Melting," 2021. [Online]. Available: <https://www.ge.com/additive/download-ebm-white-paper>.
- [21] J. Karlsson, T. Sjögren, A. Snis, H. Engqvist and J. Lausmaa, "Digital image correlation analysis of local strain fields on Ti6Al4V manufactured by electron beam melting," *Materials Science & Engineering A*, vol. 618, pp. 456-461, 2014.
- [22] Y. Kok, X. Tan, S. B. Tor and C. K. Chua, "Fabrication and microstructural characterisation of additive manufactured Ti-6Al-4V parts by electron beam melting," *Virtual and Physical Prototyping*, vol. 10, no. 1, pp. 13-21, 2015.

- [23] W. Everhart, J. Dinardo and C. Barr, "The Effect of Scan Length on the Structure and Mechanical Properties of Electron Beam-Melted Ti-6Al-4V," *Metallurgical And Materials Transactions A*, vol. 48, pp. 697-705, 2016.
- [24] H. Tang, J. Wang, C. Song, N. Liu, L. Jia, J. Elambasseril and M. Qian, "Microstructure, Mechanical Properties, and Flatness of SEBM Ti-6Al-4V Sheet in As-Built and Hot Isostatically Pressed Conditions," *Minerals, Metals & Materials Society*, vol. 69, pp. 466-471, 2017.
- [25] S. Liu and Y. C. Shin, "Additive manufacturing of Ti6Al4V alloy: A review," *Materials & Design*, vol. 164, 2019.
- [26] S. Siddique, M. Awd, J. Tenkamp and F. Walther, "2.4.2 Development of a stochastic approach for fatigue life prediction of AlSi12 alloy processed by selective laser melting," *Engineering Failure Analysis*, vol. 79, pp. 34-50, 2017.
- [27] S. Beretta and S. Romano, "A comparison of fatigue strength sensitivity to defects for materials manufactured by AM or traditional processes," *International Journal of Fatigue*, vol. 94, pp. 178-191, 2017.
- [28] Y. Murakami, "Material defects as the basis of fatigue design," *International Journal of Fatigue*, vol. 41, pp. 2-10, 2012.
- [29] S. Romano, A. Brandão, J. Gumpinge, M. Gschweidl and S. Beretta, "Qualification of AM parts: Extreme value statistics applied to tomographic measurements," *Materials & Design*, vol. 131, pp. 32-48, 2017.
- [30] P. Edwards and M. Ramulu, "Fatigue performance evaluation of selective laser melted Ti-6Al-4V," *Materials Science & Engineering A*, vol. 598, pp. 327-337, 2014.

- [31] J. Park, A. Sutradhar, J. J. Shah and G. H. Paulino, "Design of complex bone internal structure using topology optimization with perimeter control," *Comput Biol Med*, vol. 94, pp. 74-84, 2018.
- [32] G. D. Goh, S. Agarwala, G. L. Goh, V. Dikshit, S. L. Sing and W. Y. Yeong, "Additive manufacturing in unmanned aerial vehicles (UAVs): Challenges and potential," *Aerospace Science and Technology*, vol. 63, pp. 140-151, 2017.
- [33] L. M. R. Seabra, *Design Optimisation for Selective Laser Melting (SLM)*, Lisbon: [Master of Science Thesis] Tecnico Lisboa, 2015.
- [34] M. Tomlin and J. Meyer, "Topology Optimization of an Additive Layer Manufactured," Altair Engineering, Bristol, 2011.
- [35] S. T. Yiğitbaşı, *Mechanical Properties Of Ti-6Al-4V Parts Produced By Electron Beam Melting And Topology Optimizatoon In Different Building Directions*, Ankara: [Master of Science Thesis] METU, 2018.
- [36] ASTM E8, *ASTM E8 / E8M-16ae1, Standard Test Methods for Tension Testing of Metallic Materials*, West Conshohocken, PA: ASTM International, 2016.
- [37] ASTM E466-15, *Standard Practice for Conducting Force Controlled Constant Amplitude Axial Fatigue Tests of Metallic Materials*, West Conshohocken, PA: ASTM International, 2015.
- [38] ASTM E 238-17a, *Standard Test Method for Pin-Type Bearing Test of Metallic Materials*, West Conshohocken, PA: ASTM International, 2017.
- [39] EASA, *Certification Memorandum, Additive Manufacturing, CM-S-008 Issue 03*, 2021.

- [40] M. M. Francois, A. Sun, W. E. King, N. J. Henson, D. Tourret, C. A. Bronkhorst, N. N. Carlson, C. K. Newman, T. S. Haut, J. Bakosi, J. W. Gibbs, V. Livescu, S. A. Vander Wiel, A. J. Clarke, M. W. Schraad, T. Blacker, H. Lim, T. Rodgers, S. Owen, F. Abdeljawad, J. Madison, A. T. Anderson, J. L. Fattebert, R. M. Ferencz, N. E. Hodge, S. A. Khairallah and A. Walton, "Modeling of additive manufacturing processes for metals: Challenges and opportunities," *Current Opinion in Solid State and Materials Science*, vol. 21, pp. 198-206, 2017.
- [41] J. Bruno, A. Rochmann and G. Cassar, "Effect of Build Orientation of Electron Beam Melting on Microstructure and Mechanical Properties of Ti-6Al-4V," *Journal of Materials Engineering and Performance*, pp. 692-703, 2017.
- [42] A. Leicht and E. O. Wennberg, "Analyzing the Mechanical Behavior of Additive Manufactured Ti-6Al-4V Using Digital Image Correlation," Chalmers University of Technology, Gothenburg, 2015.
- [43] R. Cunningham, A. Nicolas, J. Madsen, E. Fodran, E. Anagnostou, M. D. Sangid and A. D. Rollett, "Analyzing the effects of powder and post-processing on porosity and properties of electron beam melted Ti-6Al-4V," *Materials Research Letters*, pp. 516-525, 23 Jun 2017.
- [44] M. S. Xavier, S. Yang and C. Comte, "Nondestructive quantitative characterisation of material phases in metal additive manufacturing using multi-energy synchrotron X-rays microtomography.," *Int J Adv Manuf Technol*, vol. 106, pp. 1601-1615, 2020.
- [45] J. D. Boerckel, D. E. Mason, . A. M. McDermott and E. Alsberg, "Microcomputed tomography: approaches and," *Stem Cell Research & Therapy*, vol. 5, p. 144, 2014.

- [46] GOM Correlate®, "Software retrieved from <https://www.gom.com/en/products/gom-correlate>," <https://www.gom.com/en/products/gom-correlate>, 2020.
- [47] R. C. Rice, J. L. Jackson, J. Bakuckas and S. Thompson, "Metallic Materials Properties Development and Standardization (MMPDS)," U.S. Department of Transportation Federal Aviation Administration Office of Aviation Research, Washington, DC, 2003.
- [48] ASTM E 132-97, *Standard Test Method for Poisson's Ratio at Room Temperature*, West Conshohocken, PA: ASTM International, 2017.
- [49] M. Eudier, *The mechanical properties of sintered low-alloy steels*, 1962.
- [50] L. Facchini, E. Magalini and P. Robotti, "Microstructure and mechanical properties of Ti-6Al-4V produced by electron beam melting of pre-alloyed powders," *Rapid Prototyping Journal*, vol. 15, no. 3, pp. 171-178, 2009.
- [51] F. Memu, *Katmanlı İmalat Yöntemiyle Üretilmiş Ti-6Al-4V Alaşımının Mekanik Özelliklerinin İncelenmesi*, Ankara: [Master of Science Thesis] TOBB ETÜ, 2019.
- [52] J. H. Lv, W. Z. Wang and S. W. Liu, "Statistical Analysis of Failure Cases in Aerospace," *International Journal of Aerospace and Mechanical Engineering*, vol. 12, pp. 493-497, 2018.
- [53] ©2019 Siemens Digital Industry Software Inc., "What is a SN-Curve?," Siemens, 29 08 2019. [Online]. Available: <https://community.sw.siemens.com/s/article/what-is-a-sn-curve>. [Accessed 07 10 2021].
- [54] ©2019 Siemens Digital Industry Software Inc., "The Goodman-Haigh Diagram for Infinite Life," Siemens, 29 08 2019. [Online]. Available:

- <https://community.sw.siemens.com/s/article/the-goodman-haigh-diagram-for-infinite-life>. [Accessed 07 10 2021].
- [55] Aerospatiale, *Fatigue Manual-MTS 005 Iss. B*, 1998.
- [56] M. C.-y. Niu, *Airframe stress analysis and Sizing*, HONG KONG: Conmilit Press Ltd., 2001.
- [57] Altair Hyperworks, *Open architecture simulation platform*, Altair, 2019.
- [58] H. Huth, Zum Einfluß der Nietnachgiebigkeit mehrreihiger Nietverbindungen auf die Lastübertragungs und Lebensddauervorhersage, Bericht Nr. FB-172, 1984.
- [59] M. P. Bendsøe and O. Sigmund, *Topology Optimization: Theory, Methods and Applications*, Berlin Heidelberg: Springer-Verlag, 2003.
- [60] A. T. Gaynor and J. K. Guest, "Topology optimization considering overhang constraints:," *Structural and Multidisciplinary Optimization*, vol. 54, p. 1157–1172, 2016.
- [61] R. Hoglund and F. Fuerle, "Design Optimization for Additive Manufacturing in OptiStruct with," Altair Engineering, 2018.
- [62] D. Madier, *Practical Finite Element Analysis for Mechanical Engineers*, Canada: FEA Academy, 2020.
- [63] T. Irvine, "An introduction to the shock response spectrum," 2012.
- [64] J. Liu, L. Yang, X. Zhang, R. Yan and X. Chen, "Intelligent Time-Domain Parameters Matching for Shock Response Spectrum and Its Experimental Validation in Active Vibration Control Systems," *Shock and Vibration*, vol. 2019, 2019.

- [65] T. Irvine, "Shock Response Spectrum," 2013. [Online]. Available: http://www.vibrationdata.com/software_alt/srs.m. [Accessed 30 11 2021].
- [66] A. Spaink, "'Static failure loads of metallic double shear lug," in *Handbuch Struktur Berechnung HSB 26101-01*, 2006, pp. 2-9.
- [67] E. F. Bruhn, "Fittings and Connections, Bolted and Riveted," in *Analysis and Design of Flight Vehicle Structures*, Tri-State Offset Company, 1973.
- [68] Y.-L. Lee and T. Tjhung, "Metal Fatigue Analysis Handbook," in *Chapter 3 - Rainflow Cycle Counting Techniques*, Butterworth-Heinemann, 2012, pp. 89-114.
- [69] W. Ramberg and W. R. Osgood, *Description of stress–strain curves by three parameters*, Washington DC, 1943.
- [70] J. L. Coffin , "A Study of the Effects of Cyclic Thermal Stresses on a Ductile Metal," *Trans ASME*, vol. 76, pp. 931-950, 1954.
- [71] 3DEXPERIENCE SIMULIA, fe-safe 2019 Fatigue Theory Reference, Dassault Systemes, 2019.
- [72] O. H. Basquin, "The Exponential Law of Endurance Tests," *Am Soc Test Mater Proc.*, vol. 10, pp. 625-630, 1910.
- [73] K. N. Smith, P. Watson and T. H. Topper, "A Stress-Strain Function for the Fatigue of metals," *J Mater*, vol. 5, no. 4, pp. 767-778, 1970.
- [74] H. Neuber, "Theory of Stress Concentration for Shear Strained Prismatic Bodies with Arbitrary Non-Linear Stress-Strain Law," *J Appl Mech, Trans ASME*, vol. E28, 1961.
- [75] H. Neuber, *Kerbspannungslehre*, Berlin: Springer, Berlin, Heidelberg, 1958.

APPENDICES

A. Fractured tensile test specimens and test results



Figure A.1. As-built tensile test specimens after fracture.

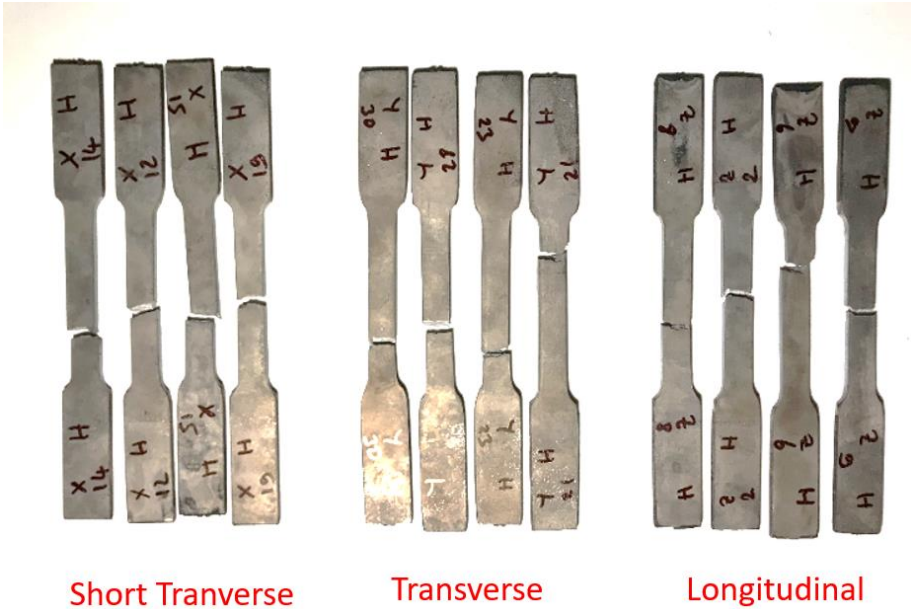


Figure A.2. HIP post-treated tensile test specimens after fracture.

Table A.1 Tensile test results

| | Specimen # | E [GPa] | ν | R _{p0.2} [MPa] | R _{pu} [MPa] | Elongation [%] |
|----------|------------|---------|-------|-------------------------|-----------------------|----------------|
| HIP | L-2-H | 118.9 | 0.28 | 924.59 | 968.91 | 7.00 |
| | L-6-H | 120.1 | 0.30 | 920.90 | 969.61 | 6.08 |
| | L-8-H | 117.6 | 0.29 | 932.21 | 979.34 | 6.08 |
| | L-9-H | 124.7 | 0.30 | 944.81 | 988.39 | 7.12 |
| | T-21-H | 120.1 | 0.30 | 897.77 | 961.47 | 6.30 |
| | T-23-H | 112.6 | 0.30 | 880.85 | 948.93 | 5.44 |
| | T-28-H | 120.2 | 0.33 | 895.14 | 964.67 | 7.21 |
| | T-30-H | 112.8 | 0.32 | 904.67 | 972.61 | 5.40 |
| | ST-12-H | 114.6 | 0.25 | 864.79 | 945.66 | 7.14 |
| | ST-14-H | 115.3 | 0.31 | 891.16 | 965.56 | 6.40 |
| | ST-15-H | 107.5 | 0.38 | 868.38 | 947.37 | 6.30 |
| | ST-19-H | 119.7 | 0.35 | 893.93 | 971.54 | 6.74 |
| As-built | L-1-NH | 120.4 | 0.30 | 977.56 | 1011.56 | 2.10 |
| | L-3-NH | 114.4 | 0.32 | 984.00 | 1028.08 | 5.24 |
| | L-5-NH | 118.3 | 0.28 | 992.06 | 1037.02 | 4.64 |
| | L-10-NH | 118.1 | 0.35 | 992.91 | 1038.56 | 3.89 |
| | T-22-NH | 114.6 | 0.30 | 921.34 | 989.20 | 6.14 |
| | T-24-NH | 117.6 | 0.28 | 952.80 | 1009.46 | 3.92 |
| | T-25-NH | 117.7 | 0.29 | 955.36 | 1030.29 | 7.67 |
| | T-29-NH | 118.1 | 0.42 | 941.67 | 999.95 | 4.57 |
| | ST-11-NH | 111.6 | 0.25 | 908.95 | 984.85 | 11.47 |
| | ST-18-NH | 114.8 | 0.34 | 892.45 | 986.77 | 8.95 |
| | ST-20-NH | 116.4 | 0.35 | 910.18 | 1003.32 | 8.63 |
| | ST-13-NH | 114.1 | 0.12 | 914.17 | 1002.59 | 12.77 |

B. Fractured fatigue test specimens and test results

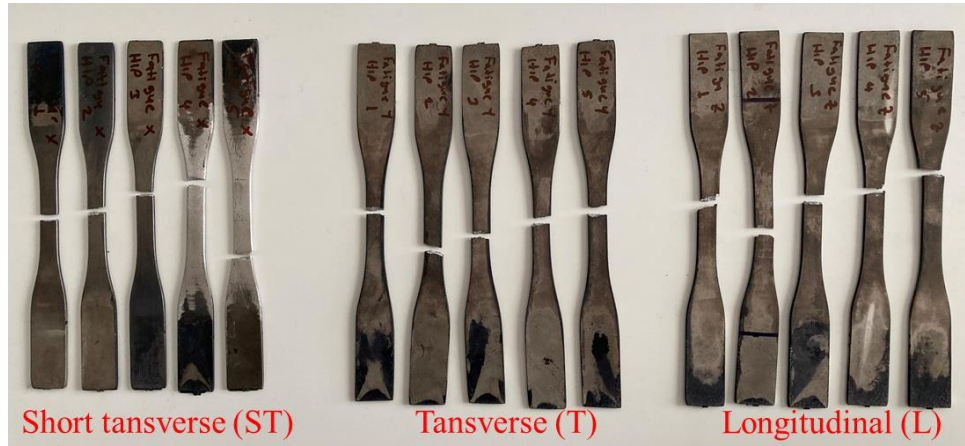


Figure B.1. HIP post-treated fatigue test specimens after fatigue fracture.



Figure B.2. As-built fatigue test specimens after fatigue fracture.

Table B.1 R=0.1 Constant amplitude fatigue test results.

| Build direction | S_{\max} [MPa] | N [Cycles] | |
|------------------|------------------|------------|-------|
| | | As-Built | HIP |
| Longitudinal | 900 | 2891 | 757 |
| | 750 | 3597 | 2476 |
| | 650 | 13386 | 4084 |
| | 550 | 14026 | 5131 |
| | 300 | 314174 | NA |
| Transverse | 900 | 3299 | 967 |
| | 750 | 6621 | 2237 |
| | 650 | 6965 | 3572 |
| | 550 | 12713 | 6580 |
| | 300 | 118895 | NA |
| Short-Transverse | 900 | 3816 | 1211 |
| | 750 | 12141 | 2286 |
| | 650 | 23665 | 7157 |
| | 550 | 36703 | 16808 |
| | 300 | 533469 | NA |

C. Derivation of IQF method and related factors

Fatigue life derivations in this section are gathered from the Airbus fatigue manual [55]. First of all, it is possible when performing the basic imposed deformation test at $R_\epsilon = -1$, at each deformation level, to determine the characteristic stabilized stress of the significant portion of the life of the test specimen; like this, a graph called "cyclic tension" comparable to that of the "monotonic tension" is obtained, which is often modeled by the "Ramberg-Osgood" formula [69], formulated as follows:

$$\epsilon = \frac{\sigma}{E} + K' \cdot \sigma^{n'}$$

Where ϵ is strain, σ is stress, E is the modulus of elasticity, K' is strain hardening coefficient and n' the strain hardening exponent.

The relationship between true local strain amplitude and endurance with regards to the life curve (see Figure C.1), the formula frequently used to represent the results at $R_\epsilon = -1$ is the "Manson-Coffin" curve [70] :

$$\epsilon_a = \frac{\sigma_f'}{E} \cdot (2 \cdot N_f)^b + \epsilon_f' \cdot (2 \cdot N_f)^c$$

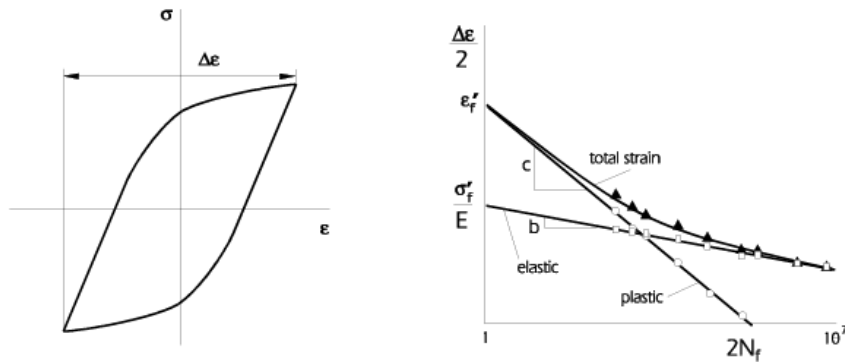


Figure C.1. Cyclic tension [71]

Strain amplitude is $\varepsilon_a = \frac{\Delta\varepsilon}{2}$ and $\Delta\varepsilon$ is the sum of elastic and plastic strain. Here, σ'_f denotes the fatigue strength coefficient, E is the modulus of elasticity, b is the fatigue strength exponent (Basquin's exponent [72]), c is the fatigue ductility exponent (the Coffin-Manson exponent), ε'_f is the fatigue ductility coefficient, which is the plastic strain amplitude at $2N_f = 1$. Moreover, N_f denotes the cycles up to failure.

In order to integrate include mean stress ratio with any ratio R_σ , the general "Smith-Topper-Watson" seems more appropriate. Smith, Watson, and Topper [73] asserted that fatigue life is not only a strain-dependent function but also stress and, therefore, stress ratio-dependent, which can be formulated as below. Moreover, different mean stresses are depicted in Figure C.2.

i. e. $\varepsilon_a \cdot \sigma_{max}$

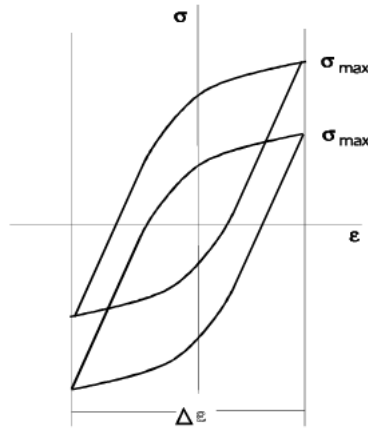


Figure C.2. Hysteresis loops with different mean stress [71]

Furthermore, the following equation is obtained after a series of equation manipulation with this claim.

$$\varepsilon_a \cdot \sigma_{max} = \frac{\sigma_f'^2}{E} \cdot (2 \cdot N_f)^{2b} + \varepsilon_f' \sigma_f' \cdot (2 \cdot N_f)^{(b+c)}$$

For a notched part subjected to uniaxial monotonic loading, the "Neuber" energy criterion may be applied. Neuber [74] proposed that local stress concentration with K_t factor and related strain must be found, depicted in Figure C.3. Nominal stress

and strain are S and e , and the local stress and strain are σ and ε , the Neuber relationship is

$$\Delta\sigma \cdot \Delta\varepsilon = Kt \cdot \Delta S. Kt \cdot \Delta e$$

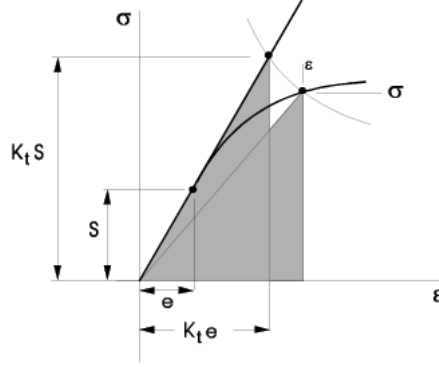


Figure C.3. Neuber's rule [71]

On the left-hand side of this equation is the true elastic strain energy of the material with elastic and plastic properties, and on the right-hand side is the energy of the material considered infinitely elastic. Neuber asserts that these two strain energies, namely the triangle areas shown in the figure, will be equal. For further formulation, S is equated to S_{max} and e is calculated by S_{max}/E . Equation is simplified as below where e is acronym for elastic.

$$\sigma_{max} \cdot \varepsilon_{max} = \sigma e_{max} \cdot \varepsilon e_{max} = \frac{Kt^2 \cdot S_{max}^2}{E}$$

Equations can be arranged for amplitudes also, then:

$$\sigma_a \cdot \varepsilon_a = \sigma e_a \cdot \varepsilon e_a = \frac{Kt^2 \cdot S_a^2}{E}$$

In the long-life domain (greater than 10^3 cycles), the Smith-Topper-Watson formula may approximately be reduced to:

$$\varepsilon_a \cdot \sigma_{max} \approx \frac{\sigma_f'^2}{E} \cdot (2 \cdot N_f)^{2.b}$$

using the second Neuber formula, the following can be formulated as:

$$\frac{Kt^2 \cdot S_a^2}{E} \cdot \frac{\sigma_{max}}{\sigma_a} \approx \frac{\sigma_f'^2}{E} \cdot (2 \cdot N_f)^{2 \cdot b}$$

Knowing that:

$$S_a = \frac{(1 - R)}{2} \cdot S_{max}$$

And that for relatively low plasticity:

$$\frac{\sigma_{max}}{\sigma_a} \approx \frac{S_{max}}{S_a} = \frac{2}{(1 - R)}$$

The following is deduced:

$$N_f \approx \left(\frac{\left(\frac{2^{(b+0.5)} \cdot \sigma_f'}{Kt} \right)}{(1 - R)^{0.5} \cdot S_{max}} \right)^{-1/b}$$

Therefore, the general form:

$$N_f \approx \left(\frac{\left(\frac{C}{Kt} \right)}{f(R) \cdot S_{max}} \right)^p$$

C (and possibly p) characterizes the effect of the material, the surface condition (related to possible heat, mechanical or chemical treatment) as well as the influence of scale (static effect related to the size of the critical area concerned by crack initiation); Kt characterizes the significance of local stress related to the geometrical notch effect; $f(R) \cdot S_{max}$ that from monotonic cyclic loading.

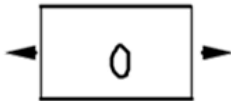
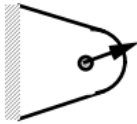

The previous formulation, even though approximate, enables us to understand better the mathematical model proposed in this manual.

In addition to the form of the equation, we can also deduce that life can reasonably be expressed as a function of two independent parameters:

- a parameter intrinsic to the part through the expression C/Kt ;

- a parameter external to the part through the expression $f(R) \cdot S_{max}$ for which a $(1 - R)^q \cdot S_{max}$ form seems more appropriate with q close to 0.5; this is confirmed by MIL-HDBK-5F, which models all life curves (on aluminum, titanium, and nickel alloys and steels) using a function of a similar type.

Table C.1 Effect of the type of structural configuration

| Type of structural configuration | | C |
|----------------------------------|--|-----|
| Notches |  | 510 |
| Yokes |  | 430 |
| Bolted or riveted assemblies |  | 630 |

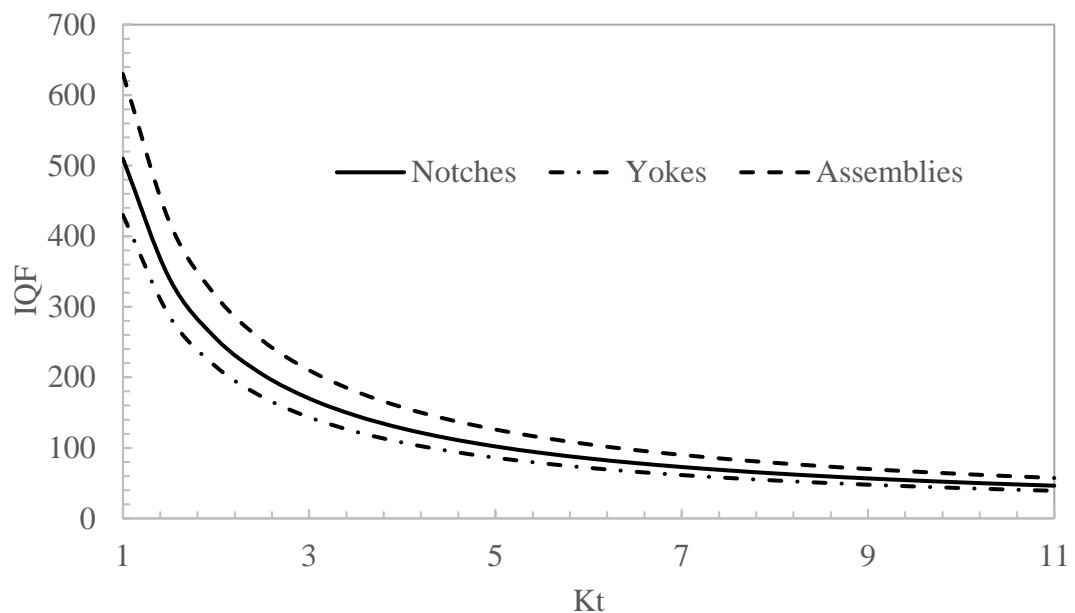


Figure C.4. Effect of C value on IQF.

The scale effect is calculated via.

$$E = \left(\frac{3.175}{r} \right)^{0.08}$$

Where r is shown in the figure. E value is limited to 0.65 for a radius higher than 600 mm

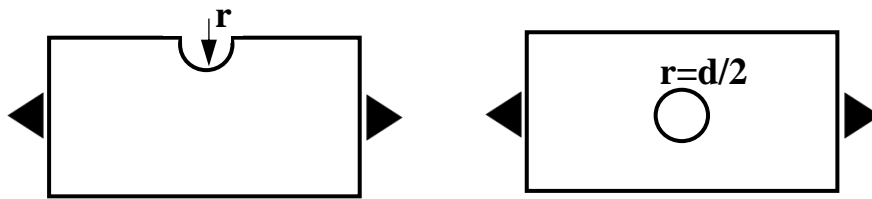


Figure C.5. Radius for scale factor calculation.

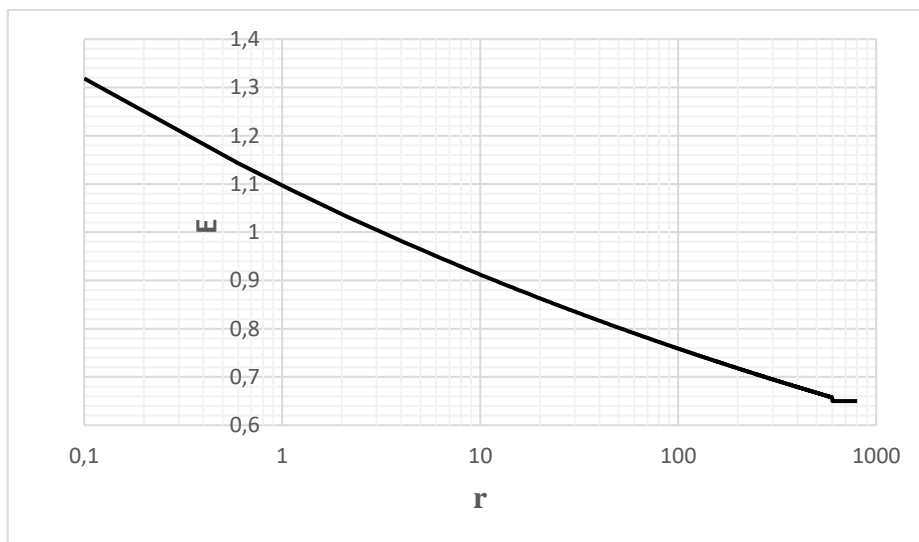


Figure C.6. Variation of scale factor according to notch radius.

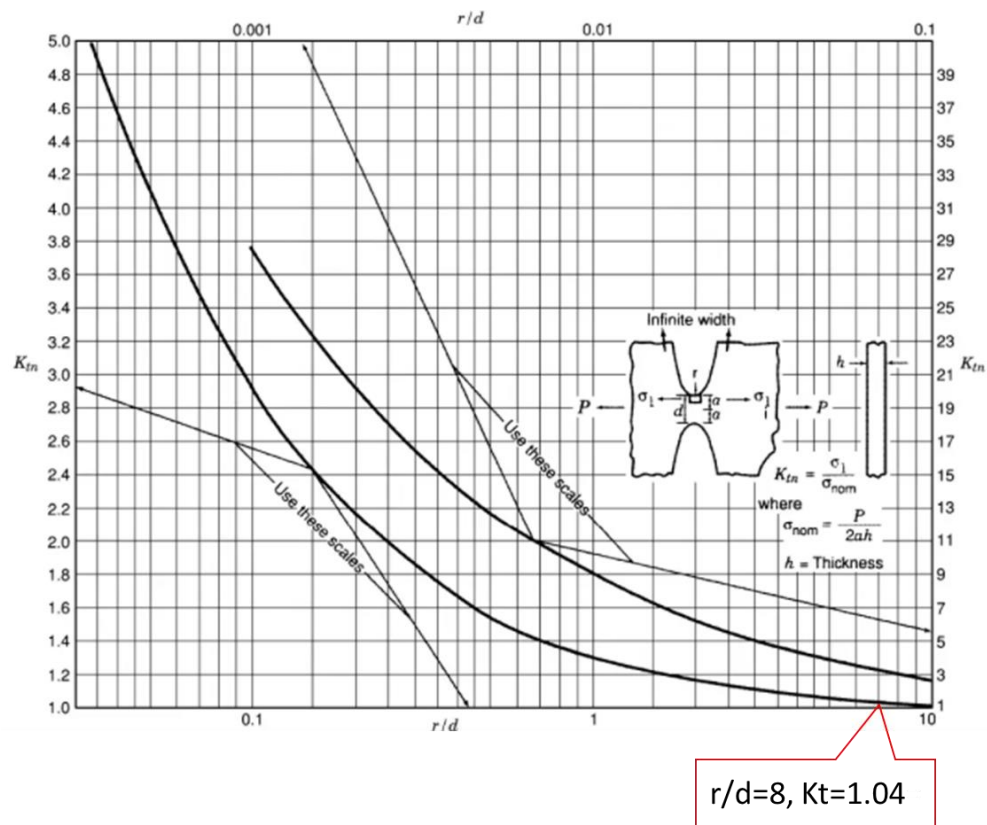


Figure C.7. Stress concentration factors K_t for opposite deep hyperbolic notches in an infinitely wide thin element in tension [75]

D. Fractured pin-bearing test specimens and test results

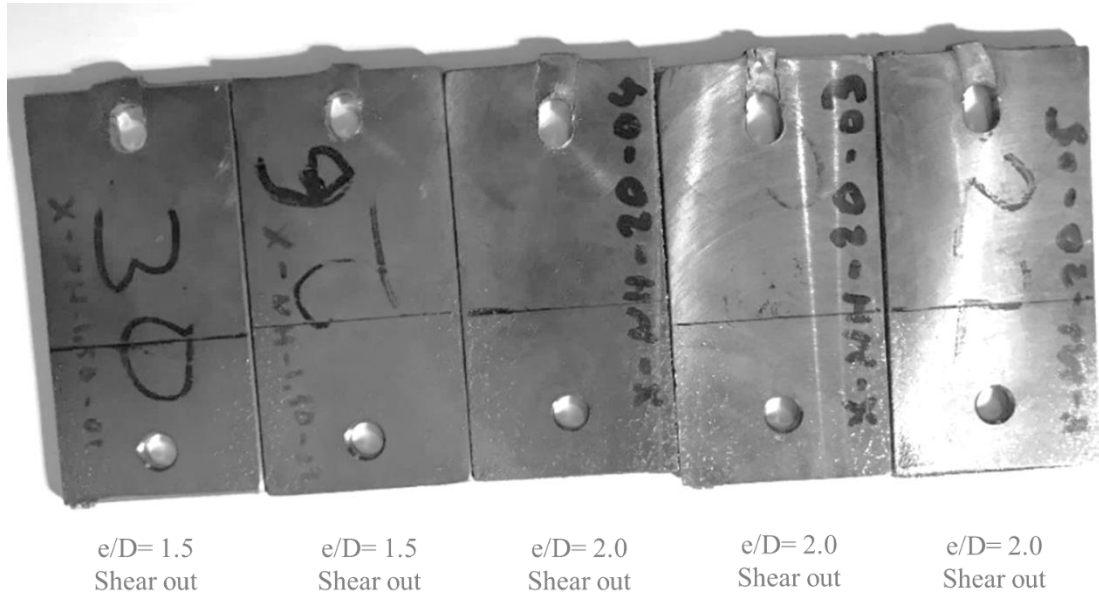


Figure D.1. As built ST build direction pin-bearing test specimens after fracture.

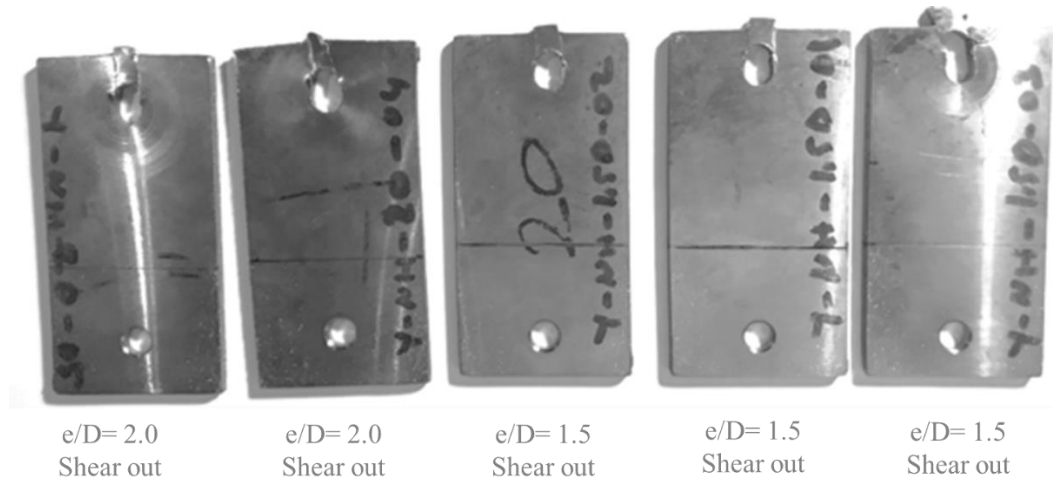


Figure D.2. As built T build direction pin-bearing test specimens after fracture.

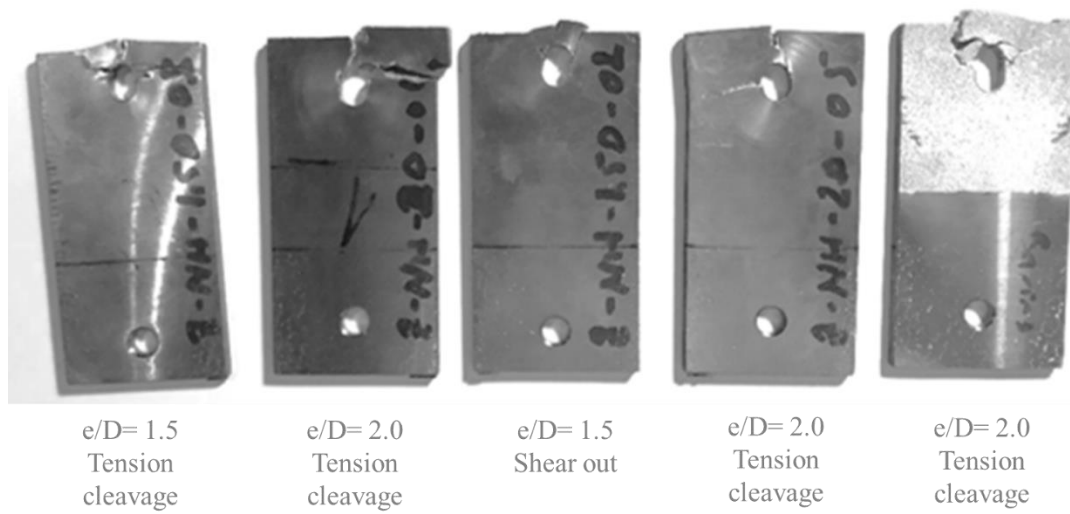


Figure D.3. As built L build direction pin-bearing test specimens after fracture.

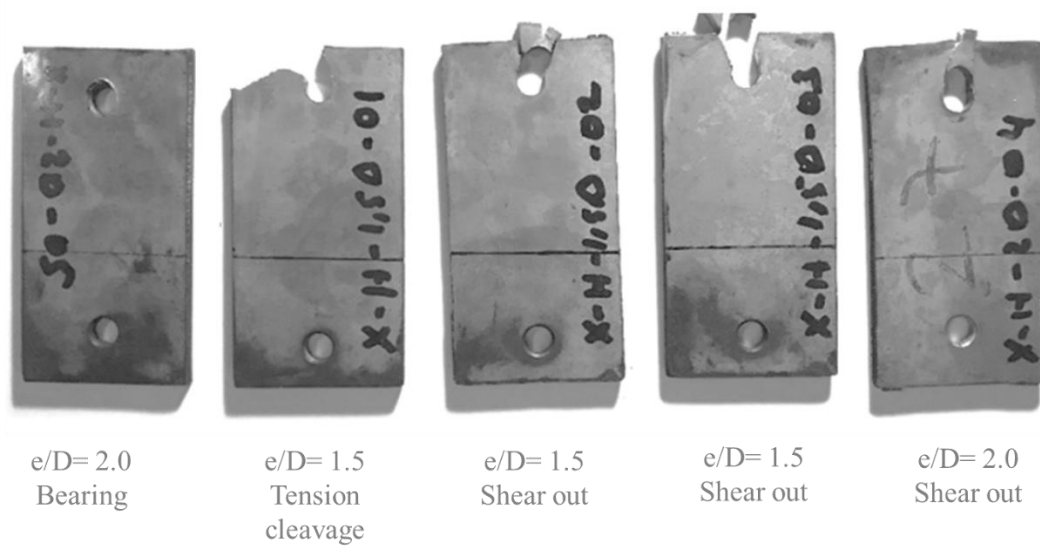


Figure D.4. HIP post-treated ST build direction pin-bearing test specimens after fracture.

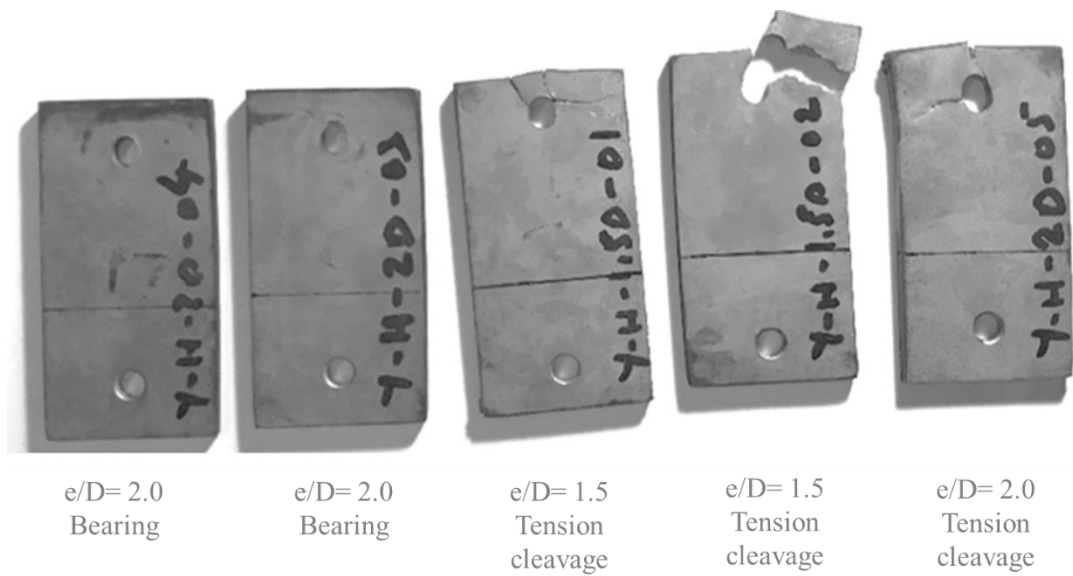


Figure D.5 HIP post-treated T build direction pin-bearing test specimens after fracture.

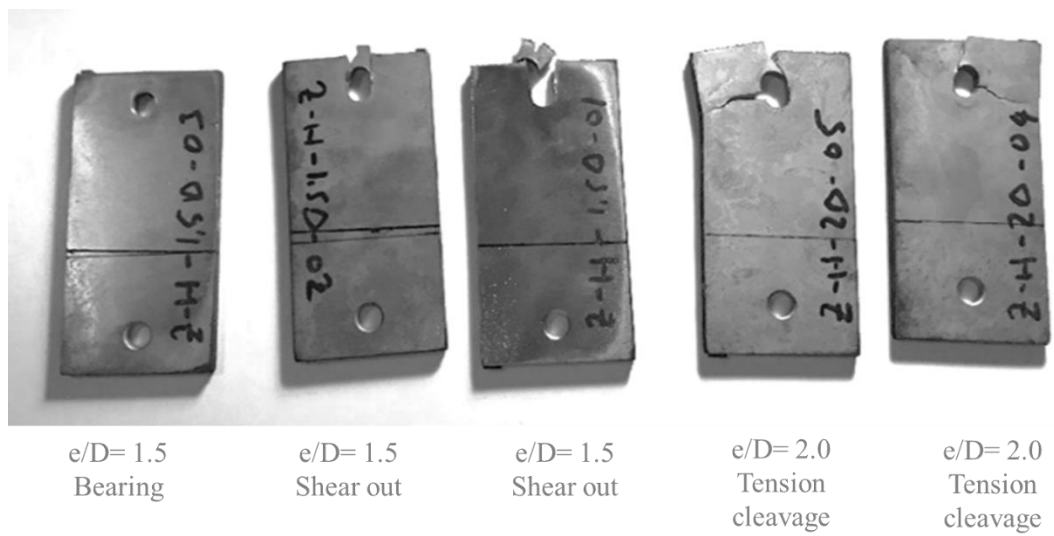


Figure D.6. HIP post-treated L build direction pin-bearing test specimens after fracture.

Table D.1 Pin-bearing test results

| | Specimen # | Fbru [MPa] | Fbry [MPa] | Remark |
|----------|--------------|------------|------------|-----------------------|
| HIP | L-H-1.5D-1 | 1281 | 1229 | |
| | L-H-1.5D-2 | 1334 | 1312 | |
| | L-H-1.5D-3 | 1368 | 1244 | Pin failure |
| | L-H-2D-4 | 1814 | 825 | 3rd trial |
| | L-H-2D-5 | 1947 | 1421 | |
| | T-H-1.5D-1 | 1465 | 1425 | |
| | T-H-1.5D-2 | 1543 | 1418 | |
| | T-H-2D-3 | 1803 | 1407 | Pin failure |
| | T-H-2D-4 | - | - | 3rd trial-Pin failure |
| | T-H-2D-5 | 1875 | 1053 | |
| | ST-H-1.5D-1 | 1499 | 1409 | |
| | ST-H-1.5D-2 | 1378 | 1302 | |
| | ST-H-1.5D-3 | 1385 | 1291 | |
| | ST-H-2D-4 | 1850 | 1527 | |
| | ST-H-2D-5 | 1205 | 1064 | Pin failure |
| As-built | L-NH-1.5D-3 | 1426 | 1276 | |
| | L-NH-2D-1 | 1937 | 1462 | |
| | L-NH-2D-4 | 1877 | 1238 | |
| | L-NH-2D-5 | 1831 | 1139 | |
| | T-NH-1.5D-1 | 1466 | 1233 | |
| | T-NH-1.5D-2 | 1521 | 1298 | |
| | T-NH-1.5D-3 | 1577 | 1269 | |
| | T-NH-2D-4 | 1956 | 1181 | |
| | T-NH-2D-5 | 1894 | 1134 | |
| | ST-NH-1.5D-1 | 1481 | 1293 | |
| | ST-NH-1.5D-2 | 1499 | 1368 | |
| | ST-NH-2D-3 | 1964 | 1579 | |
| | ST-NH-2D-4 | 1985 | 1515 | |
| | ST-NH-2D-5 | 1856 | 1230 | |

E. Finite element model element size dependency check

In order to check whether the element size of the finite element model is sufficient, static analyses are carried out with three different element sizes. As a result of this analysis, it is observed that the results do not deviate much by taking the displacement point as a reference presented in Figure E.1

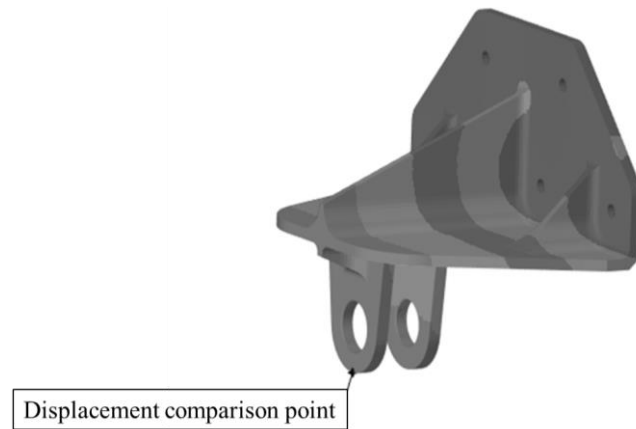


Figure E.1. Lug tip point for the displacement comparison.

Number of elements and lug tip displacements are given in Table E.1. According to Table E.1, the medium mesh is chosen for FEM analysis and topology optimization.

Table E.1 Element quantities and lug tip displacement values.

| | | Coarse mesh | Medium mesh | Fine mesh |
|-------------------|--------|-------------|-------------|-----------|
| Element types | CBEAM | 4 | 4 | 4 |
| | CTETRA | 168867 | 266050 | 410441 |
| | CBUSH | 18 | 18 | 18 |
| Displacement [mm] | | 0.57 | 0.64 | 0.66 |

F. Optimization convergence check and element size dependency

While performing the optimization, analyses are carried out with coarse, medium, and fine mesh densities to observe differences. Figure F.1 shows the element density distribution between 0 to 1 for these number of element options. As can be seen from the figure, when the number of elements increases, the objective value of the volumetric fraction (vfrac) also increases. In this study, since the vfrac target is desired as 0.30, fine mesh with 266072 elements, which gives results close to this value, is preferred for optimization.

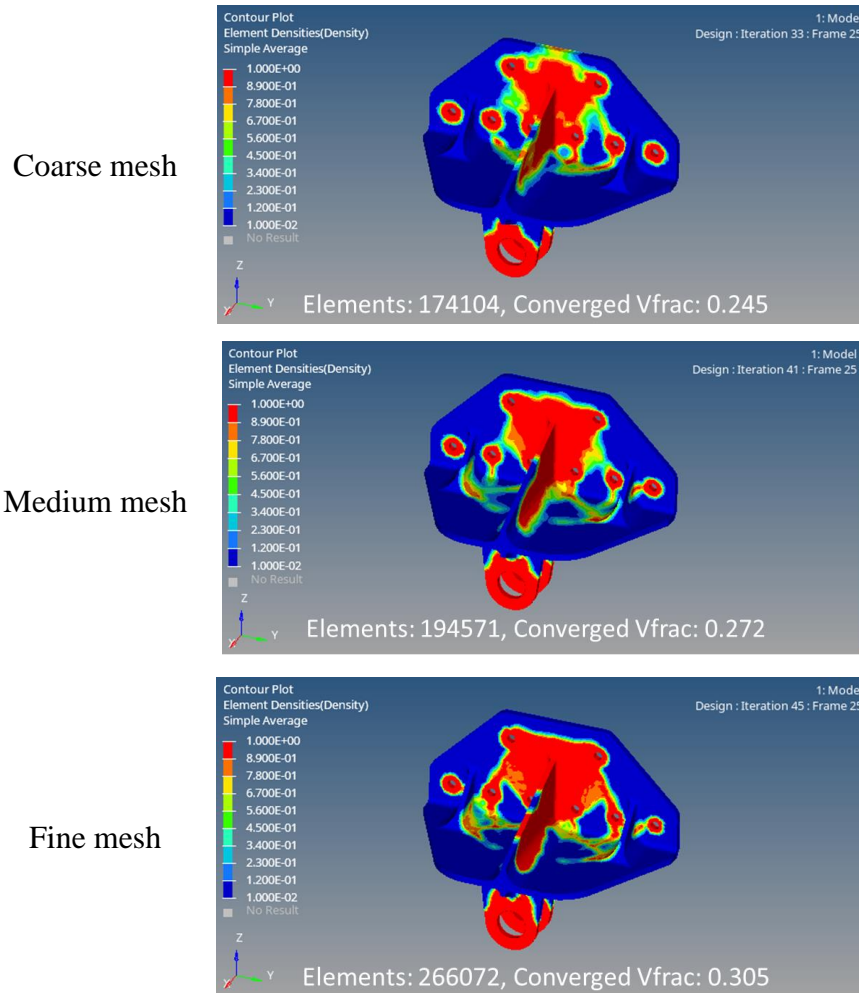


Figure F.1. Element densities contour, element quantities, and vfrac convergence results.

The geometries in Figure F.2 are obtained when the converged vfrac objective values are selected as the limit density value for each element after the optimization.

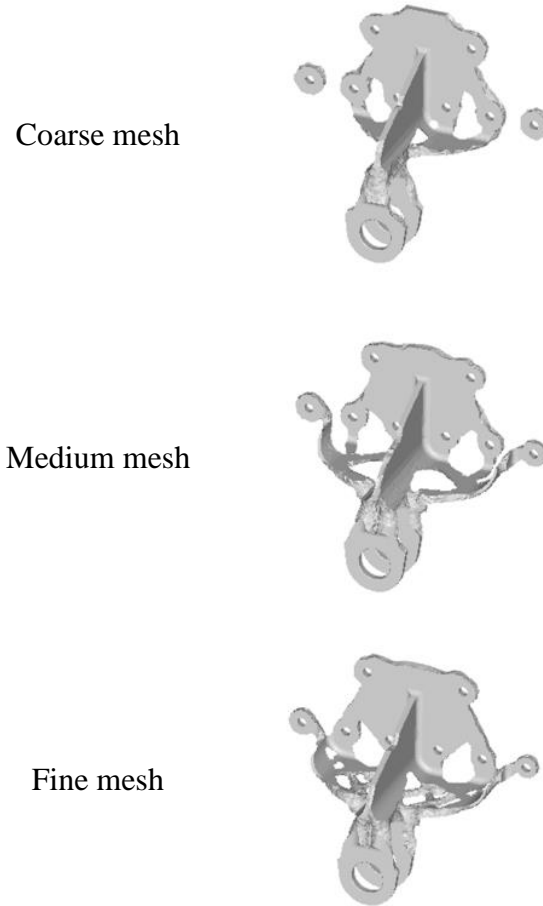


Figure F.2. Geometries regarding converged vfrac values after each optimization.

With the topology optimization performed after the selected number of elements, convergence is achieved after 45 iterations. The variation of the vfrac objective function during iterations is given in Figure F.3.

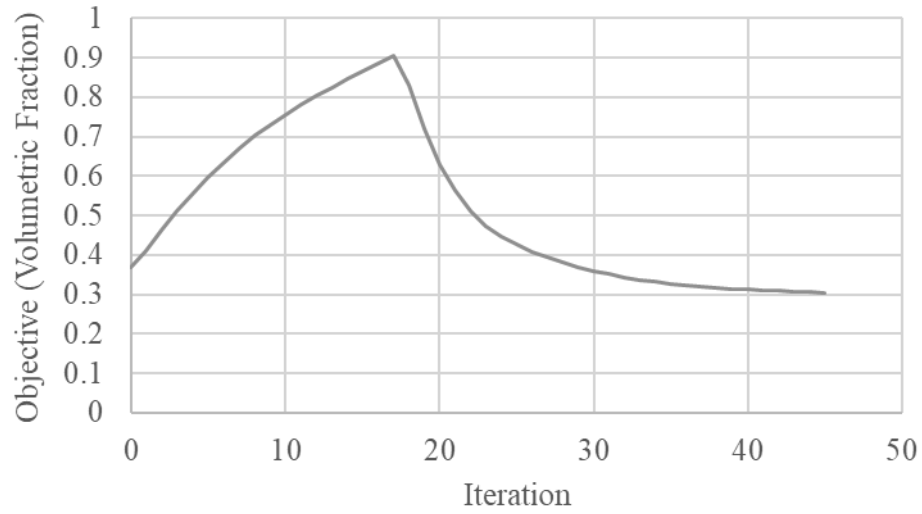


Figure F.3. Change of volumetric fraction objective according to iterations.

In addition to the convergence of objective function, the variation of displacement constraint of the node with largest displacement for three different load cases is given in Figure F.4.

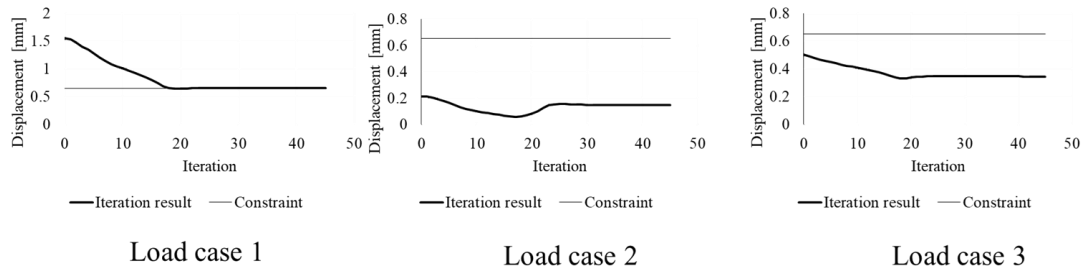


Figure F.4. Change of lug tip displacement according to load cases and iterations.

Finally, for the node that activates the max principal stress constraint, most of the time, the variation of maximum principal stress with iterations is shown in Figure F.5; however, since this node does not exist in all iterations, a graph can be created for 29 iterations.

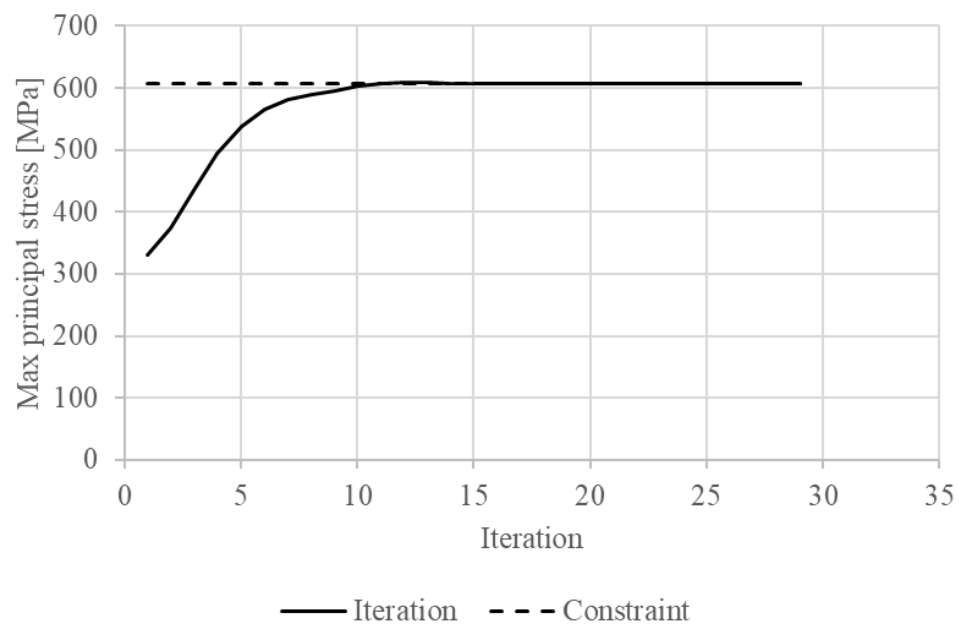


Figure F.5. Change of max principal stress according to iterations.

G. Static failure loads of metallic double shear lug

The definitions of the parameters of the method are given in the Table G.1. This notation will be used for lug static analyses.

Table G.1 Parameters for lug static analysis

| Symbol | unit | Description |
|---------------|------|---|
| d | mm | Diameter of hole in lug |
| e | mm | Edge distance (Measured in the loading direction) |
| h | mm | Eccentricity |
| j | - | Safety factor |
| r | mm | Lug radius |
| t | mm | Thickness |
| w | mm | Smaller edge distance perpendicular to loading direction |
| C | - | Factor for determination of yield strength |
| F | N | Static failure load |
| H | - | Geometry factor depending on the ratio h/r |
| K_{BR} | - | Bearing efficiency factor |
| K_{tb} | - | Ratio of the maximum tensile stress to the bearing stress |
| $K_{tb,1}$ | - | K_{tb} value for the special case $h=r$ |
| R_{bry} | MPa | Bearing yield strength |
| $R_{bry,1.5}$ | MPa | Bearing yield strength for the ratio $e/d = 1.5$ |
| $R_{bry,2}$ | MPa | Bearing yield strength for the ratio $e/d = 2.0$ |
| R_{pu} | MPa | Tensile ultimate strength |
| $R_{p0.2}$ | MPa | Tensile yield strength |
| β | ° | Lug angle |
| φ | ° | Load angle |

Figure G. depicts the lug parameters to be used in equations. The formulas to be used here are valid for the following conditions:

$$0.76 \leq \frac{d}{t} \leq 10.2$$

$$0.73 \leq \frac{h}{r} \leq 2.0$$

$$0.66 \leq \frac{r}{d} \leq 2.25$$

$$0^\circ \leq \beta \leq 45^\circ$$

$$0^\circ \leq \varphi \leq 90^\circ$$

For lugs $\beta \geq 45^\circ$, $\beta = 45^\circ$ calculations are conservative and can be used.

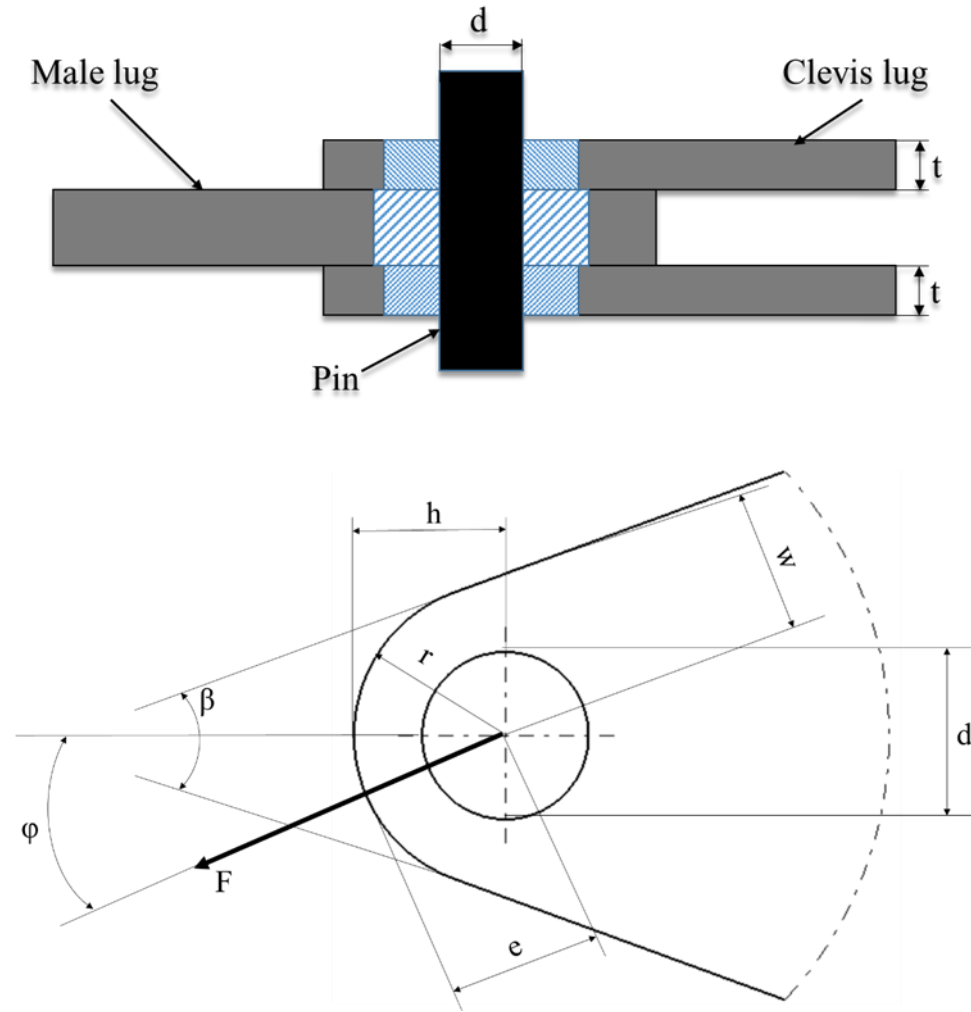


Figure G.1. Lug definition and dimension parameters.

Geometric Parameters $K_{tb,1}/H, /K_{tb}/K_{BR}$

$K_{tb,1}$ for straightlug($\beta=0$):

$$\varphi = 0: \quad K_{tb,1}(\beta = 0/\varphi = 0) = 2.75 \left[\frac{2r}{d} - 1 \right]^{-0.675}$$

$$\varphi = 90: \quad 1.332 < \frac{2r}{d} < 1.723: K_{tb,1}(\beta = 0/\varphi = 90) = 9.33 \left[\frac{2r}{d} - 1 \right]^{-1.667}$$

$$\varphi = 90: \quad 1.723 < \frac{2r}{d} < 3.400: K_{tb,1}(\beta = 0/\varphi = 90) = 7.78 \left[\frac{2r}{d} - 1 \right]^{-1.333}$$

For other φ -values $K_{tb,1}(\beta = 0/\varphi = 0)$ follows by linear interpolation between $\varphi = 0$ and $\varphi = 90$:

$$\begin{aligned} K_{tb,1}(\beta = 0/\varphi) \\ &= K_{tb,1}(\beta = 0/\varphi = 0) \\ &+ \frac{\varphi}{90} \cdot [K_{tb,1}(\beta = 0/\varphi = 90) - K_{tb,1}(\beta = 0/\varphi = 0)] \end{aligned}$$

Geometric parameters for tapered lug ($\beta > 0$):

Case 1: $\beta = 45$

$$0 \leq \varphi \leq 90: K_{tb,1} \left(\beta = \frac{45}{\varphi} \right) = 2.417 [1 + 0.00633\varphi - 0.0000815\varphi^2] \cdot \left[\frac{2r}{d} - 1 \right]^{-0.63}$$

Case 2: $0 < \beta < 45$ and $0 \leq \varphi \leq 90$

- Use linear interpolation to determine $K_{tb,1}$ for a straight lug.
- Calculate $K_{tb,1} \left(\beta = \frac{45}{\varphi} \right)$ for a tapered lug.
- Determine $K_{tb,1}(\beta/\varphi)$ by linear interpolation between $K_{tb,1}(0/\varphi)$ and

$$K_{tb,1}(45/\varphi)$$

$$K_{tb,1}(\beta/\varphi) = K_{tb,1}(0/\varphi) + \beta/45 \cdot [K_{tb,1}(45/\varphi) - K_{tb,1}(0/\varphi)]$$

c) **H** for $\frac{h}{r} \neq 1$

$$\varphi = 0: \quad H(\varphi = 0) = \left[\frac{h}{r} \right]^{-0.916} + 0.284 \cdot \log \left[\frac{h}{r} \right]$$

$$\varphi = 45: \quad H(\varphi = 45) = \left[\frac{h}{r}\right]^{-1.177} + 1.737 \cdot \log \left[\frac{h}{r}\right]$$

$$\varphi = 90: \quad H(\varphi = 90) = \left[\frac{h}{r}\right]^{-0.495} + 0.715 \cdot \log \left[\frac{h}{r}\right]$$

For other φ values H follows by linear interpolations:

$$0 \leq \varphi \leq 45 \quad H(\varphi) = H(\varphi = 0) + \frac{\varphi}{45} \cdot [H(\varphi = 45) - H(\varphi = 0)]$$

$$45 \leq \varphi \leq 90 \quad H(\varphi) = H(\varphi = 45) + \frac{\varphi - 45}{45} \cdot [H(\varphi = 90) - H(\varphi = 45)]$$

Stress concentration factor K_{tb}

$$K_{tb} = H \cdot K_{tb,1}$$

Bearing efficiency factor K_{BR}

$$K_{BR} = 7.502 \cdot [K_{tb} + 1.125]^{-1.637}$$

Three different cases are calculated for the static failure modes. These are; lug ultimate strength, lug net-section yield and lug bearing yield strength.

Case 1: Lug ultimate strength F_{Lu}

$$F_{Lu} = 0.84 \cdot K_{BR} \cdot d \cdot t \cdot R_u$$

Case 2: Lug, net-section yield strength

The smaller value of

Either

$$F_{Ly1} = 2 \cdot j \left(\omega - \frac{d}{2} \right) \cdot t \cdot R_{p0.2}$$

Or

$$F_{Ly2} = j.C.\frac{R_{p0.2}}{R_u}F_{Lu}$$

$$\frac{F_{Lu}}{d.t.R_u} \leq 1.25: \quad C = 1.1$$

$$\frac{F_{Lu}}{d.t.R_u} > 1.25: \quad C = 1.379 - 0.223.\frac{F_{Lu}}{d.t.R_u}$$

Case 3: Lug, bearing yield strength

$$F_{Ly,br} = j.d.t.R_{bry}$$

$$0.5 < \frac{e}{d} \leq 1.5: \quad R_{bry} = R_{bry,1.5} \cdot \left[\frac{e}{d} - 0.5 \right]$$

$$1.5 < \frac{e}{d} \leq 2.0: \quad R_{bry} = R_{bry,1.5} + 2 \cdot \left[\frac{e}{d} - 1.5 \right] (R_{bry,2.0} - R_{bry,1.5})$$

$$\frac{e}{d} \geq 2.0: \quad R_{bry} = R_{bry,2.0}$$

CURRICULUM VITAE

PERSONAL INFORMATION

Surname, Name: Yılmaz, Fatih
Nationality: Turkish (TC)
Date and Place of Birth: 11 February 1980, Malatya
Marital Status: Married
Phone: -
email: fatieh.yilmaz@gmail.com

EDUCATION

| Degree | Institution | Year of Graduation |
|--------|----------------------------|--------------------|
| MS | ITU Mechanical Engineering | 2005 |
| BS | ITU Mechanical Engineering | 2003 |

WORK EXPERIENCE

| Year | Place | Enrollment |
|--------------|-----------------------------------|----------------------------|
| 2010-Present | Turkish Aerospace Industries Inc. | Sr. Structural Design Eng. |
| 2008-2010 | Volvo Otomotiv Turk | Area Service Manager |
| 2006-2008 | Otokar A.Ş. | Project Design Engineer |
| 2003-2005 | Arçelik A.Ş. | R&D Engineer |

FOREIGN LANGUAGES

Advanced English

INTERNATIONAL JOURNALS

1. Yilmaz, F., Şahin, M., and Gürses, E. (2021). "Weight reduction of an unmanned aerial vehicle pylon fitting by topology optimization and additive manufacturing with electron beam melting." Journal of Additive Manufacturing Technologies, 1(2), 553. <https://doi.org/10.18416/JAMTECH.2111553>

INTERNATIONAL CONFERENCES

1. F. Yilmaz, O.O. Haktanır and A.B. Uygur, "Quasi-static structural test of satellites", 2015 7th International Conference on Recent Advances in Space Technologies (RAST), 2015, pp. 421-424

2. A.B. Uygur, O.O. Haktanır, F. Yılmaz, H.G Işık and Z. Aşansü, "Turkey's new Assembly, Integration and Test (AIT) center and its comparison with AIT centers in Europe", 2015 7th International Conference on Recent Advances in Space Technologies (RAST), 2015, pp. 71-74
3. Yılmaz, F., Şahin, M., and Gürses, E. "Weight reduction of an unmanned aerial vehicle pylon fitting by topology optimization and additive manufacturing with electron beam melting." in AMCTURKEY 2021 Conference, 10 Eylül 2021, Istanbul

NATIONAL CONFERENCES

1. Yılmaz, F., Gürses, E., ve Şahin, M. "Topoloji Optimizasyonu ve Eklemeli İmalat ile Hafifletilen Bir İnsansız Hava Aracı Pilon Bağlantı Parçasının Kalifikasyonu", SAVTEK 2022, 10. Savunma Teknolojileri Kongresi, 13-15 September 2022, METU, Ankara